REPUBLIC OF TURKEY
YILDIZ TECHNICAL UNIVERSITY
GRADUATE SCHOOL OF NATURAL AND APPLIED SCIENCES

AN EXPERIMENTAL AND NUMERICAL INVESTIGATION OF SLAMMING LOADS ON SHIP FORMS

FATIH CUNEYD KORKMAZ

PhD. THESIS
DEPARTMENT OF NAVAL ARCHITECTURE AND MARINE ENGINEERING
PROGRAM OF NAVAL ARCHITECTURE AND MARINE ENGINEERING

ADVISER
ASST. PROF. DR. BULENT GUZEL

İSTANBUL, 2016

REPUBLIC OF TURKEY

YILDIZ TECHNICAL UNIVERSITY

GRADUATE SCHOOL OF NATURAL AND APPLIED SCIENCES

AN EXPERIMENTAL AND NUMERICAL INVESTIGATION OF SLAMMING LOADS ON SHIP FORMS

A thesis submitted by Fatih Cuneyd KORKMAZ in partial fulfillment of the requirements for the degree of **DOCTOR OF PHILOSOPHY** is approved by the committee on 24.11.2016 in Department of Naval Architecture and Marine Engineering department, Naval Architecture and Marine Engineering Program.

Thesis Adviser

Assist. Prof. Dr. Bulent GUZEL

Yıldız Technical University

Approved By the Examining Committee

Assist. Prof. Dr. Bulent GUZEL

Yıldız Technical University ____________________

Prof. Dr. Mesut GUNER, Member

Yıldız Technical University ____________________

Prof. Dr. Abdi KUKNER, Member

İstanbul Technical University ____________________

Prof. Dr. Ömer BELİK, Member

Piri Reis University ____________________

Assoc. Prof. Dr. Seyfettin BAYRAKTAR, Member

Yıldız Technical University ____________________

This research has been financially supported by Yildiz Technical University Research Grants (Grant 2013-10-01-KAP03).

ACKNOWLEDGEMENTS

This thesis is the result of the work performed by the author for the degree of doctor of philosophy at the Yildiz Technical University.

I would like to express my sincere and profound to Professor Bulent GUZEL for his guidance, assistance, encouragement, advice and constant support throughout these studies.

Thanks to all the stuffs in the Department of Marine Engineering Operations and Naval Architecture and Marine Engineering for their patient and support during experimental study.

Thanks are due to the technicians for their excellence assembling experimental set up and fabrication models and for the nice friendship.

I would like to thank my colleagues for their support.

A special thanks to my father, mother, brothers and sister for their endless support.

I am deeply in depth to my wife for her endless care and support throughout these studies.

Dedicated to my lovely daughter BERIL SERRA

November, 2016

Fatih Cuneyd KORKMAZ

TABLE OF CONTENTS

Page

LIST OF SYMBOLS

C_s	Slamming coefficient
r	Radius
d	Initial submerge depth
Fr	Froud number
C_p	Pressure coefficient
M	Mass of object
F_b	Buoyancy force
F_d	Drag force
F_c	Capillary force
F	Hydrodynamic force
ζ	Depth of falling object
g	Acceleration of gravity
ρ	Fluid density
A	Cross sectional area
C_{ds}	Drag coefficient
m	Mass of added mass
ρb	Effective density of body
V^{ι}	Volume body of penetrated
γ	Surface tension
P	Length of intersection point
φ	Angle
p	Pressure
$\bar{v}$	Velocity vector
μ	Viscosity of fluid
V_0	Initial velocity
R_e	Reynold number
σ	Surface tension
D	Body length
W_e	Weber number
B_o	Bond number
ΔT_p	Alteration of energy test body
ΔT_w	Alteration water kinetic energy
$\bar{F}$	Body force
$\bar{f}$	Gravity force
S_w	Wetted length
S_f	Wetted free surface
$\bar{V}$	Solid velocity
β	Deadrise angle

r	Half circles of added mass for Von Karman Theory
γ	Function change with deadrise angle
c	Half circles of added mass for Wagner Theory
z	Depth of penetrated body for Wagner Theory
t^*	Time of reaching maximum force
F_l	Impact force per unit length
ρ_s	Cylinder density
$\bar{\xi}$	Non dimensional displacement
$\bar{t}$	Non dimensional time
L	Length of cylinder
u	Velocity component of x direction
v	Velocity component of y direction
f_x	Body force component
f_y	Body force component
$F_{surface}$	Surface force component
C1	UPVC Cylinder
C2	Aluminum Cylinder
S1	Acrylic sphere
E	Elasticity modulus
I	Second moment of inertia
R_m	Mean radius
C_{pw}	Pileup coefficient
h_p	Pileup height
t_p	Pileup width
A_p	Area of displaced water
v	Poisson ratio
h	Cylinder thickness
WF	Wetting factor
y_w	Half-length of wedge at the deformed water section
y	Half-length of wedge at the free surface level
z_{wp}	Height of splash
t	Time
C_e	Water exit coefficient
k-ε	Turbulence model
k-ω	Turbulence model
γ^*	Liquid or air energy
θ	Contact angle
ms	millisecond
HC	Hydrophobic coated
UC	Untreated coated

LIST OF ABBREVIATIONS

BEM Boundary Element Method
CFD Computational Fluid Dynamic
CPU Central Processing Unit
DAQ Data acquisition
FPSO Floating production, storage and offloading unit
FPS Frame per Second
FS Flexural stiffness
LED Light Emitting Diode
MLM Modified Logvinovich mode
MV Motor vessel
PIV Particle Image Velocimetry
PLA Polylactic acid or polylactide
QUICK Quadratic Upstream Interpolation for Convective Kinematics
SIMPLE Semi Implicit Method for Pressure Linked Equations
SPH Smoothed-Particle Hydrodynamics
UPVC Unplasticisized polyvinyl chloride
VOF Volume of Fluid
WIG Wing-in-Ground

LIST OF FIGURES

LIST OF TABLES

ABSTRACT

AN EXPERIMENTAL AND NUMERICAL INVESTIGATION OF SLAMMING LOADS ON SHIP FORMS

Fatih Cuneyd KORKMAZ

Department Of Naval Architecture And Marine Engineering Department

Phd Thesis

Adviser: Asst. Prof. Dr. Bulent GUZEL

This study is performed to investigate the slamming impact experimentally and numerically. Slamming phenomenon has an impulse character and produces high magnitude local pressure pulses that are very short in duration, followed by a lower magnitude residual pressure lasting tens of milliseconds. Various types of geometrical shapes are used when carrying slamming tests in order to obtain impact characteristics. The experiments are conducted with three different groups of specimens; namely, advancing deadrise angle ones; cylinder and sphere, constant deadrise angle ones; wedge and cones, and ship models; bulbous bow and catamaran. Drop tests have been set up for studying the impact forces, dropping test objects from various heights toward water surface. The slamming coefficient is calculated via experimental results and then compared with analytical and numerical results. The current analytical approaches for slamming impact are mainly calculation of the added mass, so the visualization of the experiments are significant. Therefore, free fall tests are recorded via a high speed camera to observe the water deformation, rise of the water and water jet propagates along the surface of the immersing body.

The effect of the deadrise angle is demonstrated via constant deadrise angle shapes by measuring the total slamming impact. The faster the velocity and the lower the deadrise angle it has, the higher the impact force it encounters. These parameters along with the total drop mass and the total volume (buoyancy force) are the main factors shaping the rise of the water and splash characteristics. Along with the experimental investigation, numerical approaches are performed using a commercial code, ANSYS-Fluent, based on finite volume method for a 2-d rigid cylinder. The results are compared with the current experimental results via non-dimensional slamming impact coefficient.

Secondly, the effect of hydrophobicity is investigated experimentally in water entry of all test shapes in this study. Hydrophobicity is the way of increasing the contact angle of a fluid on a solid surface. In this study, hydrophobic surface is created by applying a coating on the test objects. The water deformation phenomena like jet formation, water pileup, and splashing and flow separation on solid surfaces are compared under the hydrophobic effects. It is observed that flow separation occurs earlier with hydrophobic surfaces causing no pressure pulse occurrence on the solid surface at larger penetration depths. The pictures are also captured for hydrophobic coated cases from a high speed camera. It is indicated that hydrophobicity also causes larger pileups with faster jet flows indicating more kinetic energy transference to the fluid. The non-dimensional pileup coefficient is introduced to compare the rate of transferring energy. Along with the high speed images, the impact loads are calculated and compared with when hydrophobicity is present by employing strain gauge measurements. It is found that the peak values during slamming are smaller with hydrophobic surfaces promoting a reduction in the impact forces while distributing the pressure pulses on a larger wetted area.

The effect of flexibility is also studied by using different rigidity of cylinders in case of the advanced deadrise angle shapes. The relatively rigid and flexible materials are tested and less slamming impact is measured for the relatively flexible cylinder.

The water exit of cylinder and sphere is also investigated experimentally. Different fluid dynamics phenomena like free surface evolution, deformation and break up of free surface, the amount of drag water thickness and horizontal width, and water detachment from the solid surfaces during a water exit event have been examined. The deformation of the cylinder and sphere surface due to water exit is measured for different releasing depths.

Finally the wedge and cylinder shape models are tested with macro scale roughness surface to show the possible application of ship surface to gain similar effect with hydrophobic coated surface. The early water separation from the surface is also observed at wedge and cylinder with ridged surfaces.

Key words: Water entry, slamming, impact force, hydrophobicity, flexibility

ÖZET

GEMİ FORMLARI ÜZERİNE GELEN DÖVÜNME YÜKLERİNİN DENEYSEL VE SAYISAL İNCELEMESİ

Fatih Cüneyd KORKMAZ

Gemi İnşaatı ve Gemi Makineleri Mühendisliği Anabilim Dalı
Doktora Tezi

Tez Danışmanı: Yrd. Doç. Dr. Bülent GÜZEL

Bu çalışmada gemilerdeki dövünme yükleri deneysel ve numerik olarak incelenmiştir. Dövünme, dalgalı denizlerde gemi gövdesinin serbest su yüzeyinden ayrılıp tekrar suya girişi esnasında olan, milisaniye mertebelerinde ve geminin yüksek oranda basınca maruz kalındığında olan fenomendir. Dövünme testinde, çarpma etkilerini ölçmek için farklı geometrik şekiller kullanılmıştır. Deneysel çalışmada kullanılan şekillerin yüzeyleri ile serbest su yüzeyi arasındaki değişikliklerine göre, giriş açısının her bir aşamadaki derinlik değerinde farklılık gösteren silindir ve küreyi değişken açılı, buna karşı her derinlik değerinde aynı açı değeri gösteren kama, koni sabit açılı ve gemi modelleri, katamaran ve gemi baş kısım modeli olarak sınıflandırılmıştır. Serbest düşme deneyleri, araştırılan geometrinin belirli yükseklikten suya girişi sağlayarak üzerine gelen çarpma kuvvetlerini ölçmek için kurulmuştur. Boyutsuz bir değer olan dövüme katsayısı; deney, analitik ve numerik yöntemlerle elde edilerek karşılaştırılmıştır. Dövünme kuvvetinin tesbitinde kullanılan analitik yöntemlerde ek su kütlesi kullanılır ve yapılan deneylerde cisimlerin suya giriş aşamalarının görselliği önemlidir. Bu sebepten düşürme testlerinde cisimlerin suya girişi hızlı kamerayla kayıt altına alınarak suyun deformasyonu, suyun yükselmesi ve yüzey üzerinde jet akışının dağılması görselleştirilmiştir.

Kama ve koni gibi sabit açılı suya girişleri olan geometrik şekillerde giriş açısının etkisi farklı açılı modeller kullanılarak gösterilmiştir. Yüksek hızlı girişte ve düşük açılı girişlerde en fazla çarpma kuvvetleriyle karşılaşılırken giriş açısı büyüdüğünde daha az çarpma kuvvetlerine maruz kalındığı görülmüştür. Bu parametreler ile düşürülen cismin ağırlığı ve toplam hacimi (kaldırma kuvveti) yükselen suyun ve sıçrayan suyun şekillenmesinde ki sebeplerdir. Deneysel çalışmanın akabinde numerik çalışma, Ansys

Fluent programı ile 2 boyutlu silindirin suya girişi, sonlu hacim methoduyla gerçekleştirilmiştir. Nümerik sonuçlar ile deney, boyutsuz katsayı olan dövünme katsayısı değeriyle karşılaştırılmıştır.

Deneysel olarak incelenen bütün şekiller, hidrofobik kaplandığı haliyle de düşürme testleri gerçekleştirilmiştir. Hidrofobik kaplama sıvının yüzey ile yaptığı kontak açısı değerini arttırır, yani suyun yüzeyle temas alanını azaltır. Jet akışın şekillenmesi, suyun yapı ile temas noktalarını, suyun dağılması ve ayrılması gibi suyun deformasyonu olayları kaplama yapılan ve yüzeyde işlem yapılmadığı haliyle düşürülen testlerle karşılaştırılmıştır. Kullanılan şekiller hidrofobik kaplı olarak suya girdiğinde cisim üzerindeki etkileşim halinde olan suyun erken ayrılması, daha büyük ötelenen su kütlesi, daha hızlı su akışına dolayısıyla daha büyük oranlarda bir enerji transferi meydana geldiği hidrofobik kaplı testlerde gözlemlenmiştir. Oluşturulan boyutsuz bir katsayı değeri olan pileup değeri tanıtılmış ve hızlı kamera görüntüleriyle ölçülen değerler karşılaştırılmıştır. Sonuçta, cisimler hidrofobik kaplandığında daha az dövünme kuvvetlerine ulaşılırken, tepe değerle ulaşması için daha fazla ıslak alana ulaşması gerektiği bulunmuştur.

Farklı sertlik değerine sahip malzemelerle üretilen silindirler kullanılarak dövünmedeki elastisitenin etkisi araştırılmıştır. Göreceli olarak rijid ve esnek olan silindirler kullanıllanılarak, esnek silindirde daha az dövünme kuvvetleri ölçülmüştür.

Sudan çıkış problemi, silindir ve küre için deneysel olarak çalışılmıştır. Serbest su yüzeyinin değişimi, deformasyonu, ayrılması, serbest su yüzeyinden çıktıktan sonraki suyun yatay ve dikey kalınlıkları ve cismin ötelediği su miktarı sudan çıkış çalışmalarında incelenmiştir. Bu farklılıklar cisimlerin farklı derinliklerden çıkışları için ayrı ayrı araştırılmıştır. Silindir ve kürenin sudan çıkışlarındaki oluşan deformasyonlar, farklı derinliklerden bu cisimlerin serbest bırakılmasıyla ölçülmüştür.

Son olarak büyük ölçekli yüzey pürüzlülüğüne sahip ve muhtemel hidrofobik yüzey özelliklerini kazanabilecek ve gemilerde pratik uygulama sağlayabilecek kama ile silindir şekilli cisimler test edilmiştir. Suyun yüzeyden erken ayrılması pürüzlü kama ve silindirde de aynı şekilde gözlemlenmiştir.

Anahtar Kelimeler: Suya giriş, gemilerde dövünme, çarpma kuvveti, hidrofobiklik, elastiklik

CHAPTER 1

INTRODUCTION

The slamming problem creates important issues during ship sailing operations under rough sea conditions which the ship structure has to overcome; impact loads occur with high pressure among the ship hull and the free surface. The effect of impact level is changed by contact angle, shape of influenced area, type of water effect and the rate of velocity during impact. The highest slamming impact occurs at the collision stage of the highest vertical motion of a wave with the ship hull. This slamming phenomenon describes the impact of very large loads within a very short period of time. The time scale of duration of the pressure and force is in the range of milliseconds. The impact loads are responsible for local and overall damage to ship structures.

There are different types of slamming that ships experience. Two main distinctions are made for slamming types: the first one is bottom slamming and the other one is breaking wave slamming. Pure bottom slamming generally occurs with small ships and high speed boats. This happens after a wave hits, cutting the interaction between ship bottom and water line at the reentering stage to the water. This is not evident for high speed boats because they experience the same situation even in smooth water lines with help of high speed. Bottom slamming can also be observed with large ships and generally with ballast and extreme sea conditions. This slamming case is specialized as bow slamming for large ships. The samples of pure bottom and bow slamming for different sizes of ships are illustrated in figure 1.1.

Figure 1.1 Pure bottom slamming [1]

The other type of bottom slamming is wet deck slamming which is observed with the catamaran and is generated at the underside of the deck of multihulls.

Breaking wave slamming, which is another type of slamming, occurs when breaking waves hit the side of ships or offshore structures (figure 1.2). This is also the source of other branches of slamming. Greenwater slamming is a special case and occurs on deck structures by waves after crossing to the side wall.

Figure 1.2 Slamming on offshore structure [2]

A later slamming impact causes extreme fluid motion (sloshing) of the ship tanks. Figure 1.3 depicts the sample sloshing case.

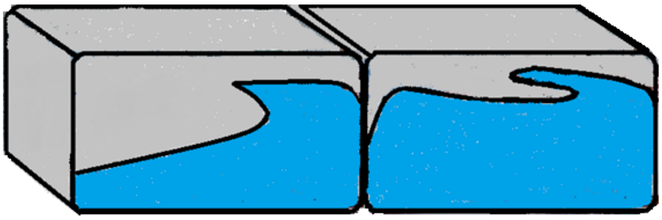

Figure 1.3 Sloshing of the ship locker

Slamming has a lot of negative effects on the ship from the ship hull structure to economic sailing parameters. Time is a very valuable factor for industry and navy forces. Slamming is an obstacle related to the increasing speed of the ship. The ship master prefers reducing the ship speed in heavy weather conditions or changing the route. The consequence of reducing the speed is late delivery of the freight, so the ship owner experiences economic loss. (Chunang [3]) Structural damage can occur instantly or also emerge as fatigue damage so the life of the structure decreases fast, day by day.

The slamming affected structure response can be changed from a local area to overall ship body according to the power of impact. The local structure can be vibrated by the slamming force with other local structural components. This exiting force finally reaches the whole ship body and may be composed of different types of vibration. This short period of vibration is another reason for the shortened life of the structure. If sufficient momentum is applied, the vibration will travel to all of the ship’s structure and can be felt by the crew and passengers. This hull vibration is called the whipping phenomenon. The longitudinal vibration has importance especially 2 node and 3 node have more caution at whipping analysis.

Finally, impulsive loads which have high energy by reason of heavy weather conditions are capable of damaging ship structures (figure 1.4). Many reports are related to slamming accidents and their results. One of them, ,reporting damage from slamming is the *Shiehallion* floating production, storage and offloading unit (FPSO) which experienced bow damage [4]. Another damaging slamming event was MV Estonia in 1994 and is also on the list of the deadliest marine incident. The damage occurred at the bow section by exiting slamming forces. Different cases have also been presented for greenwater slamming damage. Window breaking occurred on the ship bridge of the Linda Buck because of the greenwater slamming effect. As a result of the windows breaking, the ship master lost the control and the ship became stranded.

In all, slamming is hazardous for ships and offshore structural safety. In order to build proper structures, it is important to obtain the true impact values of the slamming effect.

Figure 1.4 Damage on ship structures by slamming [4]

1.1 Literature review

The problem of water impact, which involves the interaction of a structure with a fluid with free surface, has been studied experimentally and theoretically for almost a century. This impact problem, more commonly known as slamming in ocean engineering, either concerns the impact of a floating structure on the sea surface (bottom slamming) or the impact of water waves on ships and other marine structures (breaking wave slamming). Von Karman [5] and Wagner [6] are the pioneers in the field of predicting impact forces and pressure distribution during water entry. These initial researches developed their method by using potential flow theory in order to estimate the loads acting on a landing seaplane. Since then, their method has been taken as a starting point for numerous researchers and improved to give better results in similar cases and related problems that experience slamming loads. Preventing structural damages and increasing maneuverability in ship design, reducing arrival times and increasing fuel efficiency in ship operation, and improving missile entrance into water are few examples to emphasize the importance of the improved understanding of the impact forces and the parameters involved in such slamming events.

The study of fluid-structure interaction during a slamming event has been widely influenced by analytical and numerical models developed for basic geometrical shapes (wedge, cone, sphere, cylinder or flat plate) entering into water since Von Karman's and Wagner's first formulas developed on vertical entry of a wedge. In this method, the pressure and the force acting on a wedge during impact is calculated by applying the momentum theorem, i.e. some of the initial momentum of the body gained until the impact is transferred to a certain mass of water, called the added mass. The problem with this method is that it is valid only on certain deadrise angles and not valid at larger submergences due to the difficulty in calculating the added mass. Many researchers have extended the work of Von Karman and Wagner to different three dimensional geometries. Extensive experimental work has been done to validate these analytical and numerical models. Most of the experimental studies have focused on two-dimensional impact problems with emphasize of the hydrodynamic aspects of such water entry. Experimental measurements of slamming events have been carried out mostly by drop tests where a rigid or non-rigid body is dropped from a certain height creating a desired entrance velocity onto still water. The main aim of such experiments is to investigate the pressure distribution during the impact. An extensive review on the subject has been given by Abrate [7]. Chuang [8] performed experiments by dropping wedges to characterize the effects of deadrise angle and the entrained air between free surface and the body for deadrise angles less than 3 degrees. Chuang [8] later extended Wagner's theory to axisymmetric bodies and also performed experiments with cones to investigate the three-dimensional effects of slamming (Chuang and Milne, [9]). Mei et al. studied the water entry of the two dimensional body analytically. The developed method is fulfilled the boundary conditions differently contrary Wagner theory. Lin and Shieh [10] experimentally investigated the flow pattern during penetration and the pressure characteristics of a cylinder during water impact. Peseux, Gornet and Donguy [11] presented solution of the three dimensional Wagner problem numerically by applying rigid and deformable bodies. Huera-Huarte et al. [12] studied slamming for small deadrise angles and confirmed the trapped air phenomenon significantly cushions impacts with angles less than 5 degrees. Faltinsen [13], Cooper [14], Panciroli et al. [15] carried out their drop tests on non-rigid panels and deformable wedges to study hydroelasticity. I. basaran [16] modeled the slamming impact numerically. During the calculation of slamming impact, the boundary element method is used to solve fluid flow around the two dimensional objects that penetrate and so deforming the free surface. He developed the ITUSEM program to obtain the total impact force and then compared both experiment and numerical results. Zhao and Faltinsen [17] developed a nonlinear BEM for two-dimensional bodies with a jet flow approximation and applied it to rigid wedges with deadrise angles between 4° and 81°. Battistin and Iafrati [18] studied the water impact of two-dimensional and axisymmetric bodies by developing a fully nonlinear BEM taking into account the jet formation at the intersection of the body contour and the free surface. H. Luo et. al. [19] investigated the respond of 3d steel wedge with 22° deadrise angle experimentally. The flexibility is studied by using different size of stiffener and frames. They also presented to compare with numerical results and experimental results. Yettou et al. [20] performed drop tests to study two-dimensional flow situations and investigated the influence of the drop height thus entrance velocity, the deadrise angle and the mass of the wedge. The conical and wedge water impact have been studied by some other researcher. Judge et. al. [21] presented results of drop test for wedge with vertical and oblique entrance to the free surface. The good quality of penetration picture is obtained but the force and pressure measurements aren't investigated. G. De Backer et al. [22] investigated water impact of axisymmetric bodies experimentally. The pressure distribution has been measurement by mounting pressure sensor at cone and hemisphere shapes. The results were compared by asymptotic theory and peak values were measured 50 % to 70% of the theatrical values. Smith et al. [23] carried out an investigation of the flat plate impacting waves experimentally and also the process is visualized by poor quality. Kim and Hong [24] investigated the three dimensional body impacts numerically by utilizing Von Karman and Wagner approaches. They also studied slamming impacts experimentally. Simon G. Lewis et. al. [25] investigated the pressure and acceleration measurement of the wedge section with fix 25° deadrise angle experimentally. They also recorded the penetration process of wedge by high speed camera and the generation of jet is evaluated. A. C. Fairlie-Clarke and T. Tveitnes [26] presented momentum and gravity effect of wedge shape section during water entry process. They remarked that gravity effect doesn't changed hydrodynamic forces significantly. Aarsnes [27] presented pressure distribution and impact forces of the wedge and bow-flare sections for various roll angles with performing drop tests. They indicated that the roll angle doesn't have significant contribution at vertical force. Besides that horizontal forces is much effected by increasing roll angle.

Some experimental studies have been focused on two dimensional objects to use to measure slamming impact. Chuang [28] was presented drop test for wedges by different deadrise angle and flat plate. Chuang [28] composed the relation between pressure distribution and deadrise angle. Panciroli et. al. [29] studied curved rigid wedge by energy transfer approaches. They used experimental studies to compute pileup coefficient in conjunction with wedge geometry and entry velocity. The results indicated that substantial energy was transfer to risen water. The pileup coefficient generally represented as a ratio between risen water level and free surface level. And the Wagner approaches determined the pileup coefficient fixedly $\pi/2$. The other outstanding experimental study has been carried out by Greenhow [30] and determined that the pileup coefficient stay constant during penetration and there is no connection with entry velocity. In addition to this, Wagner approaches doesn't work properly for increasing deadrise angle (X. Mio [31]) and generally like slamming coefficient the values have been overestimated (Bisplinghoff [32]). Another drop test was conducted for varied deadrise angle wedges by Tveitnes [33] and axial force load cells have been used to measure hydrodynamic force. Wu et al. [34] studied the problem of drop the wedge section into the free surface and also simulated same problem by numerically. The good agreement is presented both experimental and numerical results. Okada and Sumi [35] reported the relation of pressure distribution with deadrise angle and also presented pressure formula by comparing their experiments. Also Wu et al. [36] studied two different wedges with 20 and 45 deadrise angle than compared the results by analytical and boundary element methods results. The impact behavior can changes at the water entry any shapes with small deadrise angle. Because the water can't escapes at the interface and the air cushion effects is occurred. The trap air effect between water and structure is studied by Korobkin and Pukhnachov [37]. Oh et al. [38] catch the evaluation of air pocket by visualize the water entry process.

Campbell and Weynberg [39] and Miao [40] carried out forced cylinder impact experiments and derived empirical relations for the slamming forces and provided an empirical slamming coefficient, Cs.

In some studies, an energy approach has been applied to solve the impact problem. The drop of an object to free water surface under gravity is usually considered in analyzing the process of transferring energy to the water in pileups and splashes. Molin et al. [41] analyzed the free fall impact by using the law of the conservation of energy. They showed that, at the beginning of the penetration, half of the energy transferred to the fluid is imparted to the jet flow and pileup, and the remaining half is to the bulk of water in the tank. R. Panciroli and M. Porfiri [42] conducted drop tests and visualized high speed camera images to investigate the effect of impact velocity on pileups and the energy transfer, and concluded that the risen water regularly absorbs the energy at the rate of between 60 and 80%. The formation of pileups is an important stage in energy transfer and its calculation cannot be generalized for every specimen. Faltinsen and Zhao [43] showed that the pileup coefficient varies depending on the impact dynamics and the object geometry. The numerically approach is based on velocity potential and the prediction is good on behalf of different weight, deadrise angle and water entry speed. Cointe [44] made a mathematical model rigid body impact and compared by experimental results. S. Wang and C. G. Soares [45] aiming at investigation of bow flare object with various roll angles by applying explicit finite element method. The effects of water entry velocity and roll angle have been discussed then compare with numerical prediction and experimental studies. Sun and Faltisen [46] also analyzed the bow flare section by constant roll angle. Stephen Michael Laverty [47] studied the impact of spherical projectile to the water surface experimentally. The cavity behind the spherical projectile is studied and the conical shape angle that is composed back side of sphere after the complete entry to the water is examined. The function is obtained that is affiliated to depth and impact speed.

In general, conventional shapes like wedges and spheres are used to investigate slamming phenomenon in the literature. However limited numbers of experimental studies have been carried out with three-dimensional complex geometries. Bow flare and wet deck slamming can be observed in many ship sailing operations. In particular, rough sea conditions and fast sailing are the main reasons for these two types of slamming. The relative motion of jet flow and water impact on structure can be responsible of many damages. S. Brizzolara et al. [48] investigated the slamming loads on a bow section with various numerical methods and compared them with experimental results. M. Davisa and J. Whelanb [49] developed a computational method for wet deck slamming and then compared with the experimental measurements.

Prediction of hydrodynamic loads during water exit of a body is of a great importance in designing the marine vehicles that take off from the free water surface such as sea planes and wing-in-ground effect vehicles (WIG), and that pierce through the free surface like missiles and submarines. It is also critical in designing and operating the wave energy converters. The phenomenology during water exit of an object has not been discussed as deep as in water entry in the available literature. There is a limited amount of experimental data available for comparison. The water exit of an initially fully submerged object, namely cylinder, was first studied by Greenhow and Lin [50] via high speed camera images. They investigated the non-linear free surface effects experimentally during vertical exit of a cylinder. Colicchio et al. [51] carried out experiments with a cylinder entering and exiting the water and obtained the local loads around the cylinder via pressure measurements.

In water exit events, whether for marine vehicles on seas or for models in lab-scale experiments, Reynolds number, Froude number and Weber number are large enough to neglect the viscosity, gravity and surface tension effects in analyzing the phenomenon and in load prediction calculations. Though, gravity and viscosity effects must be considered while an object moving within the water in water exit event. The movement of the sphere is resulted from the fluid forces acting on it. The net force on the sphere changes as a function of time and points upwards in a buoyancy driven exit. The pressure force, weight, drag force and buoyancy force are the forces acting on an object during buoyancy driven water exit. The buoyancy force is the dominating force on the sphere just after it has been released into its motion. As getting close to the free surface, a layer of water on top of the sphere moves upward at the same speed as the sphere, and then gets thinner as the sphere exits the free surface. At this moment, the free surface above the sphere attains first elliptic, then circular shape. When the Froude number is large enough, this circular free surface shape will maintain its shape with a certain radial thickness of water after the fully exit. Based on the general simplifying assumptions like incompressible, inviscid fluid and irrotational flow, analytical solutions are valid only for the initial stage of the flow in both water entry and exit events of solid objects. Tyvand and Miloh [52] developed an analytical free surface profile induced by a moving cylinder in a free surface flow. They concluded that the free surface breaking cannot be predicted using inviscid fluid assumption. It is only possible to simulate the free surface shape before the cylinder exits and the post breaking phase. While moving upward, the sphere creates a low pressure area behind it (Moyo and Greenhow [53]). Greenhow [54] described the two dimensionless parameters characterizing water exit; $\varepsilon = r/d$ where r is the radius of sphere and d is the initial submergence depth. And the Froude number, Fr, described by the sphere velocity and the sphere diameter.

The computation of the water impact at the computational fluid dynamics simulations is widely used at ship slamming applications. This method is the way of decreasing cost of the model test and the less computational time course is required with improved the central progress unit (C_{pu}) at the present time. The various shapes of model have been run at CFD simulations for calculate the slamming impacts. The wedge shape model has been performed by Stian Ripegutu Johannessen [55]. The calculation of the peak force and pressure value has been made for various deadrise angles at the Star-CCM+ programmed and the results compared by boundary element method, asymptotic solution. The various turbulence models are used and after the small differences between laminar and turbulence models, to avoid time consuming the laminar model was selected. The comparisons are examined for C_p maximum dimensionless pressure coefficient and Cs force coefficient. The good agreement is illustrated by theory. Espen Larsen [56] has been performed the water entry test of cylindrical shape at CFD simulations at Star-CCM+. The reason of the using cylinder was the deadrise angle changed every time step of the penetration. The times step, mesh, some numerical differences, comparison of the turbulence and laminar model has been considered to approach optimal model. Alexandru et al. [57] studied 2d slamming impact and discussed the results that is taken by using boundary element methods (BEMs), computational fluid dynamics (Fluent and Flow-3D codes), smooth particle hydrodynamics and explicit FEM (LS dyna). The approaches of peak values are decent but the differences can be observed at the following peak value for wedge section. But the agreement of the peak values doesn't provide for bow section. P. Ghadimi et al. [58] investigated the water entry of the bow shape body numerically and presented the pressure distribution, deformation of the free surface by using volume of fluid method and finite volume method approaches. Faltinsen [59] presented a brief overview of the slamming problem at CFD simulations. The various CFD methods are discussed by giving information of the selected methods advantages and disadvantages. R. Marcer et al. [60] performed the CFD simulation for wedge slamming by using different method. The used VOF and SPH (Smooth Particles Hydrodynamics) methods have been validated by analytical results. H. Ghazizade Ahsaee and A. H. Nikseresht [61] presented numerical study impact of 2d wedge into the water. The flow around the wedge is solved by finite volume method and volume of fluid scheme at the penetration. Engle and Lewis [62] reported the comparative study for water entry process of wedges. The impact pressures estimated numerically and then compared with experimental results for different entry velocity. Shan Wang [63] studied the slamming induce forces by implemented the finite element code and penalty coupling method. The vertical impact forces and pressure distribution are provided and discussed for wedges with different deadrise angle. In addition that, the effect of the roll angle on slamming impact is discussed for bow section. Zhue et al. [64] is studied the circular cylinder utilized with computational fluid dynamic methods. The viscous effect was also take into account, the contribution of this effect is negligible magnitude as prognosticative. The analytical approaches are revealed considering with made comparison by experimental and numerical results. The experimental studies are also conducted by free fall water entry test. Van Nuffel [65] studied cylinder slamming experimentally. The effect of elasticity has been shown by changing stiffness of cylinder at water entry test. It was also mention that the elasticity is the factor that can be reduces the slamming effect and the true application of the sensor is substantial at measurement stages because the little looseness can be causes wrong measured values.

More recently, in much smaller scales, the impact and spreading dynamics of liquids on solid surfaces have been extensively studied for Newtonian and non-Newtonian fluids. The outcome following impact is evinced to three different forms in liquid impact on solids; spreading, rebounding, splashing. Previous studies has showed that drop deformation depend strongly on surface properties. And it is shown that there are fundamental differences in the hydrodynamics of these impacts between hydrophilic and hydrophobic surfaces. The impact dynamics of slamming on hydrophobic surfaces are unexplored.

The wettability ratio is an important parameter in carrying analytical solutions to slamming phenomenon. This ratio can be changed with hydrophobic coating, which increases the contact angle between fluid and solid so that the surface becomes more water repellent. Therefore, the hydrophobic surface reduces the drag in microscale flows for both laminar and turbulent flow regimes. A parameter often used in the literature to quantify the drag reduction is the slip length. The slip length is defined as the ratio of the velocity of the water layer in contact with the surface (slip velocity) to the velocity gradient at the surface. At high Reynolds number flows, hydrophobic surface’s direct effect on the drag force acting on a moving object seems disappointingly small (Duez et al. [66]). But in the phenomenon associated with the entry of a solid body into a liquid, the surface wetting properties determine the way the liquid connects to the solid to form the contact line, demonstrating that the unique properties of super hydrophobic surfaces are indeed capable modifying the macroscale hydrodynamics (Duez et al. [66]). The effects of hydrophobicity in slamming have been recently investigated by Korkmaz and Guzel [67]. They showed that, in the water entry of cylindrical and spherical bodies, the amount of kinetic energy transferred to the water is increased under the hydrophobic effects and thus, the impact loads acting on the object is decreased. Korkmaz et al. [68] also showed the effect of hydrophobicity at catamaran and bow flare model. The early separation and less measured strain are also illustrated.

1.2 Objective of the Thesis

The main aims of this study are to examine the slamming impact of simple geometry by providing experimental and numerical results and to understand the analytical background of slamming. In order to obtain reliable test results, the experiments are supported both by measuring the slamming impact and recording the penetration process via high speed camera and carrying out the same test many times. Then the impact values and the significance of the occurrence of water jet, pile up and the separations of water on the surface are evaluated. Yet another objective of this thesis is to understand the effect of the surface characteristics on the slamming phenomena. To show the effect, the same simple geometry is used with the only difference being the hydrophobic coating. Then investigation is made for the same parameters in the uncoated cases. According to the author, no such experiments have been performed for the slamming test by changing the surface properties.

1.3 Hypothesis

During investigation of the slamming effect there are lots of assumptions: water is incompressible and non-viscous, the gravity effect is neglected, and rigid materials are used. However, flexibility in the material, in particular, has a huge effect during slamming. The current study shows that drop tests of any shape with flexible material measure less impact force and so decrease the slamming impact because the impact energy is absorbed more into itself and into the flexible material so there is less impact measure.

The surface parameter has not been studied before for the slamming phenomena. The hydrophobic surface changes the dynamic contact angle stabilities and so decreases the wettability of the surface. Early separation of the water occurs on the surface, therefore the impact distributions change and also more water detaches during penetration, so the transferring the potential energy of the specimen through the water is more than hydrophilic surface. These differences are also observed in impact measurements; less impact is measured at the hydrophobic surface.

CHAPTER 2

GENERAL INFORMATION

2.1 What happens during slamming?

Slamming impact has an impulse character and produce high magnitude local pressure pulses (around hundreds of kPa) which are very short in duration, followed by a lower magnitude residual pressure lasting tens of milliseconds. This pressure distribution rapidly travels across the immersed body surface making a maximum at the solid-fluid interface at the location where the water jet is formed. This water jet propagates along the surface of the immersing body. From the theory and the experiments, it is known that the maximum impact pressure is proportional to the square of the entrance velocity of the body and is always reached in the vicinity of the waterline. The pressure pulse magnitude and the propagation speed are critically dependent on the impact velocity and deadrise angle of the impacting body. The faster the velocity and the lower the deadrise angle it has, the higher the impact force it encounters. These parameters along with the total drop mass and the total volume (buoyancy force) are the main factors shaping the water uprise and splash characteristics.

Following Von Karman's and Wagner's approach, staying within the framework of potential flow theory, slamming forces can be calculated by conducting momentum analysis with the concept of added mass, i.e. the force acting on a rigid body is equal to its added mass multiplied by its acceleration. In Von Karman's approach, water uprise is completely neglected. Wagner [6] modified Von Karman's formula to take the piled-up water into account. Thus, Wagner's approach gives a larger impact force prediction and is assumed to be more accurate. But the water jet flow, so the splash is still neglected in his approach. Because in momentum analysis, it is shown that the flux of momentum going into the jet is much smaller compared to the flux of momentum going into the remainder of the fluid in the asymptotic solution. In conclusion, Von Karman's formula underestimates the impact force, while Wagner's formula overestimates it (Cointe and Armand [69]) for rigid bodies. On the other hand, the conservation of energy dictates us that the rate of change of the energy within the fluid plus the energy loss due to water uprise and splash at the free surface is equal to the work performed by the moving body. Cointe and Armand [69] investigated the water uprise and the jet flow in detail. According to the asymptotic analysis, half the energy transferred from the body to the fluid is imparted to the main flow and the other half is to be found within the jets developing near the intersections (Cointe et al. [70]). The jet flow (and splash) and the spray at the first contact creates nonlinear effects during the impact (Cointe and Armand [69]). Panciroli et al. [29] investigated the flow physics during water entry of curved wedges via PIV analysis and concluded that between 60 and 80% of the energy transferred to the fluid during the impact is imparted to the risen water, which accounts for the pile-up and the spray jets. Experimental results show that these nonlinearities in the equations of motion as the body penetrates the free surface play an important role in the hydrodynamics of the impact.

From the literature it can be said that an accurate prediction of the impact force can be made under the general simplifying assumptions such as incompressible and inviscid fluid, irrotational flow, no body flexibility, no aeration in flow, no surface tension. Knowing that the maximum impact loads are experienced at the very beginning of impact, these assumptions are not adequate to obtain a right solution to the problem since there are some other effects to be considered. For example, Nuffel [65] investigated the effect of flexibility on cylinder impacts and concluded that the flexibility in the test object decreases the measured pressure and force data.

2.2 Water entry load theory

In this section, the pioneer theory is described for various forces acting on various shapes of bodies during slamming. The equations developed by Von Karman and Wagner Theory are used for comparison of the experimental and numerical results.

2.2.1 General consideration

Various forces can act during the penetration process of an object. These forces are: Mg which comes from the weight, F_B buoyancy force, F_D the drag force (because of the surface tension), F_C the capillary force and lastly the hydrodynamic force F which has major influence on objects. So, the equation of motion of a falling object during slamming can be written as follows:

$$m\ddot{\zeta} = Mg - F - F_B - F_C - F_D \tag{2.1}$$

where ζ is the depth of the falling object under the free surface and

M is the mass of the falling object

When an object penetrates the water surface, a mass of fluids is stuck on the surface and travels with the falling object which is called added mass or virtual mass. The abbreviation of m is used in the equations. The added mass is increased after the penetration starts and is governed by:

$$F = \frac{d}{dt}\left(m\dot{\zeta}\right) = m\ddot{\zeta} + \frac{dm}{d\zeta}\dot{\zeta}^2 \tag{2.2}$$

F transfers into equation 2.1, then the equation can be written:

$$\frac{d}{dt}\left((M+m)\dot{\zeta}\right) = Mg - F_B - F_C - F_D \tag{2.3}$$

or

$$\left((M+m)\ddot{\zeta}\right) = Mg - F_B - F_C - F_D - \frac{dm}{d\zeta}\dot{\zeta}^2 \tag{2.4}$$

The drag force can be expressed by the fluid density ρ, the cross sectional area A at the intersection with the free surface and the steady state drag coefficient C_{ds}:

$$F_D = \frac{1}{2}\rho A C_{ds}\dot{\zeta}^2 \tag{2.5}$$

The drag coefficient C_{di} can be expressed from $(\frac{dm}{d\zeta})\dot{\zeta}^2 = \frac{1}{2}\rho A C_{ds}\dot{\zeta}^2$ and then takes the following form:

$$C_{di} = \frac{2}{\rho A}\frac{dm}{d\zeta} \tag{2.6}$$

Regarding the effective density of body, $\bar{\rho}_B$ and the volume of the body, the weight of the body is described as $Mg = V\bar{\rho}_B g$. The buoyancy force is $F_B = V'\rho g$, where $V'$is the volume of the penetrated body and g is the acceleration of gravity. The capillary force is; $F_C = \gamma P \sin\varphi$ where γ is the surface tension, p is the length of intersection on the water surface and φ is the angle which is formed from tangent to the water line at the body water intersection to the horizontal line of the water. Finally the equation of motion becomes:

$$\frac{d}{dt}\left((M+m)\dot{\zeta}\right) = Mg - F_B - \gamma P \sin\varphi \; - \frac{1}{2}\rho A C_{ds}\dot{\zeta}^2 \tag{2.7}$$

$$\left((M+m)\ddot{\zeta}\right) = Mg - F_B - \gamma P \sin\varphi \; - \frac{1}{2}\rho A (C_{ds} + C_{di})\dot{\zeta}^2 \tag{2.8}$$

2.2.2 The relative importance of external forces for water entry

Various forces have an effect on water entry bodies, which are described in equation 2.1, but are generally neglected for slamming problems.

The drag force is an important parameter only if there is full penetration into the water. Therefore, the drag forces can be negligible at the early stages of penetration. When the drag force formulation is considered for these stages, the cross sectional area is very small so the drag force doesn't have a significant contribution to the equation of motion for water entry.

The following statement is written for describing non dimensional (Reynold's, Weber's and Froude's) numbers to show the ineffectiveness of the viscous, capillary and gravitational forces.

The stress tensor for Newtonian fluid is:

$$\sigma_{ij} = -p\delta_{ij} + \mu\left(\frac{\partial v_i}{\partial x_j} + \frac{\partial v_j}{\partial x_i}\right) \tag{2.9}$$

where p is the pressure

$\bar{v}$ is the velocity vector and

μ is the viscosity of the fluid

μ is 0 for inviscid fluids and then the stress of any surface is -p$\bar{n}$. The Navier-Stokes equation is written for incompressible fluid as:

$$\rho\left[\frac{\partial\bar{v}}{\partial t} + (\bar{v}.\bar{\nabla})\bar{v}\right] = -\bar{\nabla}p + \mu\nabla^2\bar{v} - \rho g\bar{k} \tag{2.10}$$

where$\bar{\nabla} = \bar{\imath}\left(\frac{\partial}{\partial x}\right) + \bar{\jmath}\left(\frac{\partial}{\partial y}\right) + \bar{k}\left(\frac{\partial}{\partial z}\right)$, $\bar{\nabla}p = \bar{\nabla}.\left(p\underline{I}\right) = \bar{\imath}\left(\frac{\partial p}{\partial x}\right) + \bar{\jmath}\left(\frac{\partial p}{\partial y}\right) + \bar{k}\left(\frac{\partial p}{\partial z}\right)$, I is the identity tensor and $\nabla^2 = \bar{\nabla}.\bar{\nabla}$. The right hand side of equation 2.10 shows the pressure, viscosity and gravity effect respectively. To determine the effectiveness of these parameters for the slamming event, the non-dimensional parameter is defined (Abbrate [7]);

$$\bar{v}' = \frac{\bar{v}}{V_0},\ p' = \frac{p}{\rho {V_0}^2},\ t' = V_0 t/D \text{ and } \nabla' = D\nabla \tag{2.11}$$

where $V_0$is the initial velocity and the characteristic dimension is demonstrated as a D notation. The equation 2.10 can be written as a non-dimensional form;

$$\frac{\partial \bar{v}'}{\partial t'} + (\bar{v}'.\bar{\nabla}')\bar{v}' = -\bar{\nabla}'p' + \frac{1}{Re}\nabla'^2\bar{v} - \frac{1}{Fr^2}\bar{k} \tag{2.12}$$

The notation Re is the Reynold number and formulated as, $Re = \rho V_0 D/\mu$; and Fr is the Froude number and defined as, $Fr = V_0/\sqrt{gD}$. The viscous and gravity effects become negligible at high values of the Reynold and Froude numbers. Considering the water entry event values, for instance the entry velocity, gravity and water density, the non-dimensional parameters show large values so the viscosity and gravity have less effect on slamming.

Surface tension has a significant contribution to marine animals whether moving or staying on the water surface. When the body enters the water, the reaction is occurred because the inertia effect is changed by ρV^2 and the area that is affected by the water is proportional to D^2. The occurred force with surface tension has link by product of σ and body length (D). The Weber number indicates the importance of these parameters as;

$$We = \frac{\rho {V_0}^2 D}{\sigma} \tag{2.13}$$

where σ is the surface tension

The Weber number is used for dynamic cases but the Bond number is used for static cases. The weight of the object and surface tension ratio are important for the static situation so the Bond number is:

$$\mathrm{Bo} = \frac{\rho g D^2}{\sigma} \tag{2.14}$$

When the slamming case values are embedded into the Weber and Bond numbers, then very large values are obtained so the surface tension is not of significant importance for slamming.

2.2.3 Von Karman Theory

The Von Karman theory does not taken into account all the other forces in the equation of 2.3. Then the equation of motion becomes:

$$\frac{d}{dt}\left((M+m)\dot{\zeta}\right)=0 \tag{2.15}$$

After the time integration:

$$MV_0=(M+m)\dot{\zeta} \text{ or } \dot{\zeta}=\frac{MV_0}{M+m} \tag{2.16}$$

Besides that, the added mass is zero and the initial velocity is V_0before the penetration process, so t=0.

The equation of 2.16 indicates linear momentum conservation. The water entry problem is sketched for wedge entry at figure 2.1 for the Von Karman approach. The semicircle side shows the added mass of the fluid. During penetration, m increases and, contrary to the added mass, the velocity decreases. The whole process occurs by the energy transfer method. The initial energy of the solid is transferred to the fluid at penetration. The alteration of energy for a water entry test body is:

$$\Delta T_p=\frac{1}{2}M\left({V_0}^2-\dot{\zeta}^2\right)=\frac{1}{2}M{V_0}^2\frac{m(2M+m)}{(M+m)^2} \tag{2.17}$$

The alteration of the water kinetic energy is:

$$\Delta T_w=\frac{1}{2}m\dot{\zeta}^2=\frac{1}{2}M{V_0}^2\frac{Mm}{(M+m)^2} \tag{2.18}$$

The energy transfer ratio for penetration is:

$$\frac{\Delta T_w}{\Delta T_p}=\frac{M}{2M+m} \tag{2.19}$$

The ratio shows that the kinetic energy loss is up to 50%. The main part of the energy is absorbed at the water basin and the remaining part is transferred to the pileup and jet flow. Besides these formulation results, estimation of this ratio which was made by (Pancilori [29]), is close to 70% of the energy transfer to the risen water.

2.2.4 Wagner Theory

Pressure occurs on the wetted widths (S_w) of penetrated bodies and the hydrodynamic forces can be calculated by integrating on their surfaces:

$$\bar{F} = \int_{S_w} p\vec{n}dS \tag{2.20}$$

where $\vec{n}$ is , outside normal for selected small elements, dS. The equation of conservation of momentum and continuity for fluid flow are written as:

$$\rho\left[\frac{\partial\vec{v}}{\partial t} + (\vec{v}.\vec{\nabla})\vec{v}\right] = -\vec{\nabla}p + \mu\nabla^2\vec{v} + \vec{F} \tag{2.21}$$

$$\frac{\partial\rho}{\partial t} + \vec{\nabla}.(\rho\vec{u}) = 0 \tag{2.22}$$

where ρ is the density of fluid

p is the pressure and

$\vec{F}$ are the body forces.

With regard to the body force applied in the vertical direction, the gravity force becomes; $\vec{f} = \rho g\vec{j}$.

To simplify the calculation, the following item is applied:

-irrational flow ($\bar{\nabla}\ x\ \bar{v} = 0$)

The potential function can be written:

$$\bar{v} = \bar{\nabla}\phi = \frac{\partial\phi}{\partial x}\bar{\imath} + \frac{\partial\phi}{\partial y}\bar{\jmath} + \frac{\partial\phi}{\partial z}\bar{k} \tag{2.23}$$

-the fluid is incompressible so the equation (2.22) changes to $\bar{\nabla}.\bar{v} = 0$ and after applying the equation (2.23) for irrotational flow, it becomes:

$$\bar{\nabla}.\bar{v} = \bar{\nabla}.(\phi) = \nabla^2\phi = \frac{\partial^2\phi}{\partial x^2} + \frac{\partial^2\phi}{\partial y^2} + \frac{\partial^2\phi}{\partial z^2} = 0 \tag{2.24}$$

Thus, the known Laplace equation is introduced. The Bernoulli's equation can be revealed by embedding the equation of (2.23) into (2.21) by ignoring the viscosity and gravity as follows:

$$\frac{p}{\rho} = \frac{\partial\phi}{\partial t} - \frac{1}{2}(\bar{\nabla}\phi.\bar{\nabla}\phi) \tag{2.25}$$

It gives the relation between pressure p and velocity potential ϕ. Now, the Bernoulli equation is used to improve the equation (2.20), and so the force calculation,

$$\bar{F} = -\rho\int_{S_w}\left(\frac{\partial\phi}{\partial t} + \frac{1}{2}(\bar{\nabla}\phi.\bar{\nabla}\phi)\right)\bar{n}dS \tag{2.26}$$

The calculation can be made by finding the potential function and boundary conditions. The fluid domain boundary conditions are; the fluid domain S_w, the wetted width and the free surface S_F. The velocity of the solid is equal to the velocity of the fluid in the normal direction.

$$\bar{v}\,.\,\bar{n} = \bar{V}.\bar{n} \tag{2.27}$$

where $\bar{V}$ is the solid velocity

The fluid velocity through the normal to the wetted surface can be represented as $\bar{v}\,.\,\bar{n} = (\frac{\partial \phi}{\partial n})$. The pressure has to be zero on the free surface, thus

$$\frac{\partial \phi}{\partial t} + \frac{1}{2}(\bar{\nabla}\phi . \bar{\nabla}\phi) = 0 \tag{2.28}$$

Finding the potential function and boundary conditions is the main difficulty.

The body is assumed to be a flat plate at the intersection of the body and the free surface, and the length is 2r in the Wagner two dimensional approach. During penetration, the length of flat plate r increases so both parameters are directly proportional. Thus, the Wagner expanding method is named for this method. The velocity vector is written as follows for the two dimensional;

$$\bar{v} = \bar{\nabla}\phi = \frac{\partial \phi}{\partial x}\bar{\imath} + \frac{\partial \phi}{\partial y}\bar{\jmath} \tag{2.29}$$

The potential is taken in the Wagner model as follows:

$$\phi = -V\sqrt{r^2 - z^2} \tag{2.30}$$

where $z = x + iy$. The velocity component of the x direction is $(|x| < r, y = 0)$;

$$\frac{\partial \phi}{\partial x}(x, 0) = V\frac{x}{\sqrt{r^2 - x^2}} \tag{2.31}$$

The y direction of the velocity component is zero because the fluid particles have velocity only in the horizontal direction at this approach. Besides, it can be deduced from equation (2.31), that the velocity is zero for the x=0 and y=0 directions. However, the velocity is infinite at the end of the horizontal direction (x=r, y=0). Now, consider the Bernoulli formulation (2.25) to calculate the pressure along the flat plate:

$$\frac{p}{\rho} = \frac{\partial \phi}{\partial t}\left(V\sqrt{r^2 - x^2}\right) - \frac{1}{2}\left(V\frac{x}{\sqrt{r^2 - x^2}}\right)^2 \tag{2.32}$$

The wetted length and velocity change during the penetration process in the Wagner method:

$$\frac{p}{\rho} = \dot{V}\sqrt{r^2 - x^2} + \frac{V\,r\dot{r}}{\sqrt{r^2-x^2}} - \frac{1}{2}\frac{V^2x^2}{r^2-x^2} \tag{2.33}$$

As $x \to r$, the first term leads to zero and the other terms become infinite on the right side of equation (2.33).

The ratio of the second and third terms is:

$$\frac{V\,r\dot{r}}{\sqrt{r^2-x^2}} / \left(\frac{1}{2}\frac{V^2x^2}{r^2-x^2}\right) = \frac{2r\dot{r}}{Vx^2}\sqrt{r^2 - x^2} \tag{2.34}$$

The equation of (2.33) shows that the third terms have greater value than the second terms at the near edge of the flat plate so the equation of 2.33 leads to the pressure becoming negative at the wetted edge surface of the flat plate.

2.3 Water Entry of Wedge

A simplified test model is used to understand the phenomena of water entry. Because the impact on the body can be solved more easily by simple geometry, the wedge is performed by the Von Karman and Wagner theories. A wedge selection is chosen because it has similarities to the floats on seaplane. The following section gives the impact formula, and the hydrodynamic force is defined for a wedge by the Von Karman approach and the pressure distribution is revealed using the Wagner method.

2.3.1 Von Karman Theory for Wedge Water Entry

The problem is illustrated for wedge water entry using the Von Karman approach. The wedge penetrates with initial impact velocity $V_0$and the contact angle β, the so-called deadrise angle. The mass of the wedge is M and consider the wedge as a unit thickness. During penetration, it is considered that the half-circle occurs with a radius, r, which is moving with the wedge, and the mass (added mass m) of this part is (figure 2.1):

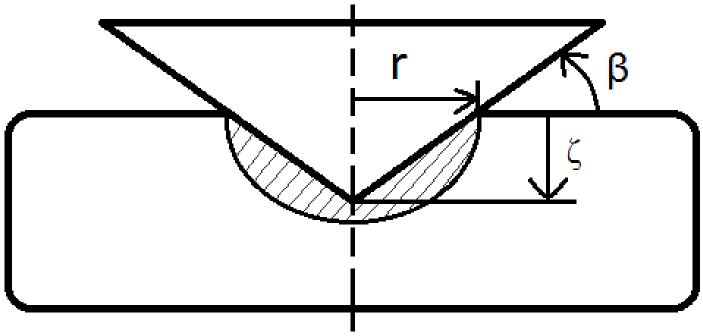

Figure 2.1 Von Karman Approaches for Wedge Water Entry

$$m = \frac{\pi}{2}\rho r^2 = \frac{\pi}{2}\rho \frac{\zeta^2}{tan^2\beta} \tag{2.35}$$

From figure 2.2, it can be observed that water deformation has occurred, so the term ζ should be changed to γ ζ, which then becomes:

$$m = \frac{\pi}{2}\rho r^2 = \frac{\pi}{2}\rho \frac{\gamma^2\zeta^2}{tan^2\beta} \tag{2.36}$$

where γ is a function which changes with the deadrise angle

Water deformation takes place at the intersection point of the free surface and the structure. This deformation is stated by $\eta(x) = \left(\frac{2\beta}{\pi}\right) x \sin^{-1}(\frac{c}{x})$ formulation. Consequently, the depth of the wedge is $\pi\zeta/2$ when considering the risen water (pileup) and the added mass radius is equal to $r' = \pi r/2$. Later on, the γ value becomes $\gamma = \pi/2$ at $\beta = 0$ and $\gamma = 1$at $\beta = \pi/2$. The values can be changed by different approaches but these are generally accepted values (X. Mei et al. [31]). $\gamma = 1$ is taken for the Von Karman approach and $\gamma = \pi/2$ is taken for the Wagner approach.

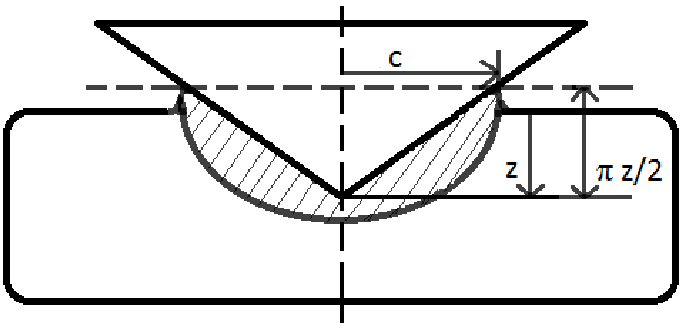

Figure 2.2 Wagner approaches for wedge water entry

Substituting equation (2.36) into equation (2.16), the velocity of the wedge becomes:

$$\dot{\zeta} = \frac{V_0}{1+\frac{\pi}{2}\rho\frac{\gamma^2\zeta^2}{M\,tan^2\beta}} \tag{2.37}$$

From equation (2.15), the acceleration can be written as;

$$\ddot{\zeta} = \frac{d}{dm}\left(\frac{MV_0}{M+m}\right).\frac{dm}{d\zeta}.\frac{d\zeta}{dt} = -\frac{MV_0}{(M+m)^2}.\frac{dm}{d\zeta}.\frac{d\zeta}{dt} = -\frac{\dot{\zeta}^3}{MV_0}\frac{dm}{d\zeta} \tag{2.38}$$

From equation (2.36), m translates into the following equation;

$$\ddot{\zeta} = -\frac{\pi\rho\gamma^2}{MV_0 tan^2\beta}\zeta\dot{\zeta}^3 \tag{2.39}$$

The hydrodynamic force F is obtained by putting equation 2.39into the force, wedge mass and acceleration equation:

$$F = -M\ddot{\zeta} = \frac{\pi\rho\gamma^2}{V_0 tan^2\beta}\zeta\dot{\zeta}^3 \tag{2.40}$$

The ζ is the only variable in equation (2.37). When the derivative force is set to a depth of zero, the maximum force level is obtained at the following depth,

$$\zeta^* = \sqrt{\frac{2M}{5\pi\rho\gamma^2}}tan\beta \tag{2.41}$$

The velocity is found by using equation (2.41) in (2.37):

$$\dot{\zeta}^* = \frac{5}{6}V_0 \tag{2.42}$$

Thus, the maximum force can be obtained by using equation (2.40) and (2.42),

$$F^* = (\frac{5}{6})^3\frac{{V_0}^2}{tan\beta}\sqrt{\frac{2\pi}{5}\rho M\gamma^2} \tag{2.43}$$

The following equation can be obtained by the method of separating variables in equation (2.37):

$$\left[1 + \frac{\pi}{2}\rho\frac{\gamma^2\zeta^3}{Mtan^2\beta}\right]d\zeta = V_0 dt \tag{2.44}$$

By integration, the time and penetration depth interaction is given;

$$t = \left[\zeta + \frac{\pi}{2}\rho\frac{\gamma^2\zeta^3}{M\,tan^2\beta}\right]/V_0 \tag{2.45}$$

The hydrodynamic force values are found by using equation (2.41):

$$t^* = \frac{16}{15}\frac{\zeta^*}{V_0} = \frac{16}{15}\sqrt{\frac{2M}{5\pi\rho\gamma^2}}\frac{tan\beta}{V_0} \tag{2.46}$$

Using equation 2.40, the entry velocity of the wedge is constant and the force F can be found:

$$F = \frac{\pi\rho\gamma^2}{tan^2\beta} {V_0}^3 t \qquad (2.47)$$

The dimensionless force coefficient for the wedge water entry problem is:

$$C_s = \frac{F\ tan\beta^2}{\rho {V_0}^3 t} \qquad (2.48)$$

2.3.2 Wagner approaches for water entry problem of wedge

The Wagner approach takes the water elevation on the surface so the length of the flat plate is $r = \left(\frac{\pi}{2}\right)(\zeta tan\beta)$ at the $\gamma = \pi/2$ in equation (2.36). Substituting into equation (2.33), it becomes:

$$\frac{p}{\rho} = \dot{V}\sqrt{r^2 - x^2} + \frac{\pi}{2}\frac{V^2 r}{tan\beta\sqrt{r^2-x^2}} - \frac{1}{2}\frac{V^2 x^2}{r^2-x^2} \qquad (2.49)$$

where $V = \dot{\zeta}$. The wedge acceleration has low values so the first term on the right hand side can be neglected.

2.4 Water entry of Cone Shape

The cone shape of the water entry is used to examine some marine applications so this simplification is also useful to estimate slamming forces. The implementation of the Von Karman [5] and Wagner [6] approaches for cone water entry is presented in the section below.

2.4.1 Von Karman Theory for Cone water entry

The added mass calculation is made by considering the circular plate which penetrates with a cone and the radius of the circle is the half horizontal length of the cone with the intersection point. The used lengths are demonstrated in figure 2.3.

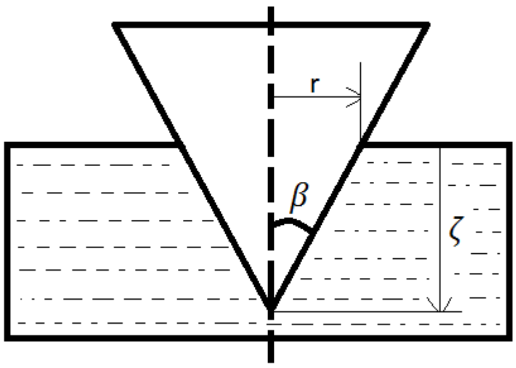

Figure 2.3 Von Karman approaches for cone water entry

The added mass is $\boldsymbol{m = \frac{4}{3} r^3 \rho}$, by using the intersection with penetration depth and half diameter of the cone tip ($\boldsymbol{r = \zeta \tan \beta}$). Thus,

$$m = \frac{4}{3}\rho(\zeta \tan \beta)^3 \tag{2.50}$$

The velocity of the cone can be obtained by using the conservation of momentum,

$$\dot{\zeta} = \frac{MV_0}{M+m} = \frac{MV_0}{M+\frac{4}{3}\rho\zeta^3 tan^3\beta} \tag{2.51}$$

To define the acceleration of the cone, the equation 2.38 is used:

$$\ddot{\zeta} = -\frac{\dot{\zeta}^3}{MV_0}\frac{dm}{d\zeta} = -\frac{(MV_0)^2}{\left(M+\frac{4}{3}\rho\zeta^3 tan^3\beta\right)^3}(4\rho\zeta^2 tan^3\beta) \tag{2.52}$$

So, the hydrodynamic force is:

$$F = -M\ddot{\zeta} = \frac{4\rho\zeta^2 tan^3\beta}{\left(1+\frac{4}{3M}\rho\zeta^3 tan^3\beta\right)^3}{V_0}^2 \tag{2.53}$$

The following equation is calculated to define the maximum values of the force occurring at a given time. The relation with time and penetration depth is given by integration of the equation 2.50:

$$t = \frac{\zeta}{V_0}\left(1 + \frac{1}{3M}\rho\zeta^3 tan^3\beta\right) \tag{2.54}$$

This formulation can be derived with respect to ζ and then the penetration depth can be derived as follows at the maximum acceleration value:

$$\zeta^* = \frac{1}{\tan \beta}\left(\frac{3M}{14\rho}\right)^{1/3} \tag{2.55}$$

The added mass and velocity can be reached by substituting into equations of (2.50) and (2.51):

$$m = \frac{4}{14}M, \dot{\zeta}^* = \frac{7}{9}V_0 \tag{2.56}$$

Substituting into 2.52and 2.53, the maximum force and the time at which it occurs can be found:

$$F^* = 4\left(\frac{7}{9}\right)^3 \rho^{1/3} M^{2/3} {V_0}^2 \tan \beta = 1.8820\, \rho^{1/3}\, M^{2/3}\, {V_0}^2 \tan \beta \tag{2.57}$$

$$t^* = \frac{15}{14}\frac{\zeta^*}{V_0} = 5(3/14)^{4/3}(M/\rho)^{1/3}/(V_0 \tan \beta) = 0.64115\, (M/\rho)^{1/3}/(V_0 \tan \beta) \tag{2.58}$$

The force calculation is defined for the passing of small amounts of time after penetrating the water. The added mass has hemisphere radius r that is accepted as:

$$m = \frac{2\pi}{3}\rho(\zeta\tan\beta)^3 \quad (2.59)$$

Approximation of hydrodynamic forces is with assuming m « M, $\dot{\zeta} \approx V_0$ so$\zeta \approx V_0 t$,

$$F = -M\ddot{\zeta} = \frac{M^3 {V_0}^2}{(M+m)^3}(2\pi\rho\zeta^2 tan^3\beta) \approx \left(2\pi\rho {V_0}^4 t^2 tan^3\beta\right) \quad (2.60)$$

The non-dimensional force coefficient for the cone shape is defined as follows:

$$C_s = \frac{F\, tan\beta^3}{\rho {V_0}^4 t^2} \quad (2.61)$$

2.4.2 Wagner Theory for Cone water entry

The pressure distribution is defined by the Wagner approach with radius of added mass circle c and entry velocity V:

$$\frac{p(x)}{\rho} = \dot{V}\sqrt{c^2 - x^2} + \frac{Vc}{\sqrt{c^2-x^2}}\dot{c} - \frac{1}{2}\frac{V^2x^2}{c^2-x^2} \quad (2.62)$$

Then, substitute the $c = \zeta\tan\alpha$, $\dot{c} = \dot{\zeta}\tan\alpha$ and $\dot{V} = \dot{\zeta}$ into the equation:

$$\frac{p(x)}{\rho} = \ddot{\zeta}\sqrt{\zeta^2\tan^2\alpha - x^2} + \frac{\dot{\zeta}^2\zeta\tan^2\alpha}{\sqrt{\zeta^2\tan^2\alpha - x^2}} - \frac{1}{2}\frac{\dot{\zeta}^2x^2}{\zeta^2\tan^2\alpha - x^2} \quad (2.63)$$

2.5 Water Entry of Sphere Shape

This section provides analytical calculations for sphere water entry. The impact of velocity formulation is indicated in equation 2.16. Therefore the acceleration is written as:

$$\ddot{\zeta} = \frac{d}{dm}\left(\frac{MV_0}{M+m}\right).\frac{dm}{d\zeta}.\frac{d\zeta}{dt} \quad (2.64)$$

And rewritten as

$$\ddot{\zeta} = -\frac{(MV_0)^2}{(M+m)^3}.\frac{dm}{d\zeta} \quad (2.65)$$

The added mass of the hemisphere of radius r is written as follows:

$$m = \frac{2\pi}{3}r^3\rho = \frac{2\pi}{3}\rho(2R\zeta - \zeta^2)^{3/2} \quad (2.66)$$

$$\frac{dm}{d\zeta} = 2\pi\rho[2R\zeta - \zeta^2]^{1/2}(R - \zeta) \quad (2.67)$$

The sphere mass is obtained by $M = (4\pi/3)\,\rho_s R^3$ and the ratio of added mass and sphere mass is defined as:

$$\frac{m}{M} = \frac{1}{2}\frac{\rho}{\rho_s}\frac{[2R\zeta - \zeta^2]^{3/2}}{R^3} \quad (2.68)$$

Then the acceleration and hydrodynamic forces can be written as:

$$\ddot{\zeta} = -\frac{2\pi\rho V_0{}^2}{M}\frac{\left[2R\zeta-\zeta^2\right]^{1/2}(R-\zeta)}{\left[1+\frac{1}{2}\frac{\rho}{\rho_S}\frac{\left[2R\zeta-\zeta^2\right]^{3/2}}{R^3}\right]^3} \quad (2.69)$$

$$F = \frac{M^3 V_0{}^2}{(M+m)^3} 2\pi\rho[2R\zeta - \zeta^2]^{1/2}(R - \zeta) \quad (2.70)$$

The slamming coefficient for the sphere is defined as:

$$C_s = \frac{F_l}{\frac{1}{2}\rho V_0{}^2 A_x} \quad (2.71)$$

where $F_l$is the impact force per unit length and A_x is the projected area of the sphere.

2.6 Water entry of Cylinder Shape

The cylinder shape water entry calculation is also considered because some parts of a ship or offshore structure have cylindrical shapes. Therefore the force calculation and non-dimensional force coefficient are presented below.

2.6.1 Von Karman Theory for Cylinder Water entry

The added mass is defined per unit length:

$$m = \frac{\pi}{2}\rho r^2 = \frac{\pi}{2}\rho(2\zeta R - \zeta^2) \quad (2.72)$$

Substitution into the equation 2.16, the cylinder velocity can be calculated as follows:

$$\dot{\zeta} = V_0/[1 + \frac{\rho}{\rho_s}\left(\tilde{\zeta} - \frac{\tilde{\zeta}^2}{2}\right)] \quad (2.73)$$

where ρ and ρ_s stand for the density of fluid and the cylinder, respectively and $\tilde{\zeta}$ is the non-dimensional displacement ($\tilde{\zeta} = \zeta/R$). To obtain the non-dimensional displacement and time ($\tilde{t} = V_0 t/R$) relation, the equation 2.73 is used:

$$\tilde{t} = \tilde{\zeta} + \frac{\rho}{\rho_s}\left(\frac{\tilde{\zeta}^2}{2} - \frac{\tilde{\zeta}^3}{2}\right) \quad (2.74)$$

The acceleration is defined by using equation 2.65:

$$\ddot{\zeta} = -\frac{(MV_0)^2}{(M+m)^3}\frac{\pi}{2}\rho(2R - 2\zeta) \quad (2.75)$$

where M is the cylinder mass per unit length. Then the hydrodynamic force can be found by:

$$F = -M\ddot{\zeta} = \pi\rho {V_0}^2 R\left(1-\tilde{\zeta}\right)/(1+\frac{\rho}{\rho_s}\left(\tilde{\zeta}-\frac{\tilde{\zeta}^2}{2}\right))^3 \tag{2.76}$$

This formulation shows that the hydrodynamic force written at the very early stage of penetration is:

$$F = \pi\rho {V_0}^2 R \tag{2.77}$$

The intersection point of cylinder and water free surface radius is r for the Von Karman approach but the wetting factor of $\sqrt{2}$ is used by Wagner [6] so the radius of the intersection is $r\sqrt{2}$. The hydrodynamic force with wetting factor is $F \approx 2\pi\rho {V_0}^2 R$.

The slamming coefficient for the cylinder is:

$$C_s = \frac{F_l}{\rho R L {V_0}^2} \tag{2.78}$$

where F_l and L are the forces that are affected per unit length and the length of the cylinder, respectively.

The following statements are made to present the C_s values by different approaches:

$C_s = \pi$ is calculated by the Von Karman approaches and $C_s = 2\pi$ for the Wagner Theory. The C_s obtained is the same as the Von Karman Theory but changes during penetration with the Greenhow and Yanbao [71] approaches by $C_s = \pi(1-\frac{\zeta}{R})$. The Wellicome theory [72], based on the Wagner Theory, found the following form $C_s = 2\pi/1+\frac{3}{2}\frac{\zeta}{R}$. Campbell and Wenberg [73] performed the empirical form by cylinder water entry experiment and they obtained, $C_s = \frac{5.15}{1+8.5\,\zeta/R}+\frac{0.275\zeta}{R}$. Another empirical relation was made by Miao [40] from experimental study of cylinder slamming; $C_s = 6.1e^{-6.2\frac{\zeta}{R}}+0.4$.

2.7 Computational Fluid Dynamic

The computational fluid dynamic is used to perform cylinder water entry simulations and to calculate the impact dynamics on the cylinder. The outcomes of the water entry cylinder are impact force, distribution of velocity and pressure flow field. The various flow models and entry velocity are implemented by using ANSYS Fluent 16.1.

2.7.1 Finite Volume Method

The numerically solved fluid flow has a common term namely, computational fluid dynamics. The Laplace and Navier-Stokes (momentum conservation) equations are solved by the finite volume method in the present simulations.

2.7.2 Governing Equations

The continuity equations describe the same amount of flow entering and exiting the control volume. The two dimensional control volume case is shown in figure 2.4.

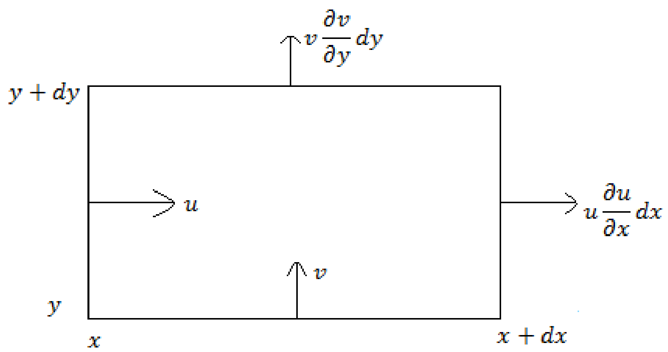

Figure 2.4 Conservation mass at control volume

The u and v letters state the x and y directions of the velocity components. The total mass flux is defined as:

$$-\rho dyu + \rho dy(u + u_x dx) - \rho dxv + \rho dx\left(v + v_y dy\right) = 0 \tag{2.79}$$

The negative values express the mass flux entering the control volume, while the positive values express the mass flux exiting from the control volume,

which can be stated as:

$$\frac{du}{dx} + \frac{dv}{dy} = 0 \tag{2.80}$$

The conservation of momentum is expressed by the Navier-Stokes equation in flow. The small control volume which affects the external forces, as demonstrated in figure 2.5, is considered.

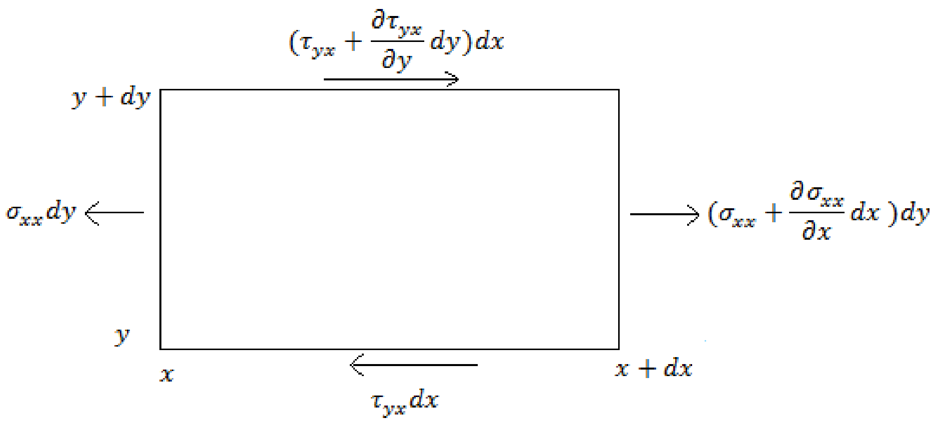

Figure 2.5 Conservation momentum at control volume

The surface forces are written for the x and y directions as follows:

$F_{surface,x} = \left[-\sigma_{xx}dy + \left(\sigma_{xx} + \frac{\partial \sigma_{xx}}{\partial x} dx\right) dy\right] + \left[-\tau_{yx}dx + \left(\tau_{yx} + \frac{\partial \tau_{yx}}{\partial y} dy\right) dx\right]$ then reduced to,

$$F_{surface,x} = \left(\frac{\partial \sigma_{xx}}{\partial x} + \frac{\partial \tau_{yx}}{\partial y}\right) dxdy \tag{2.81}$$

$F_{surface,y} = \left[-\sigma_{yy}dx + \left(\sigma_{yy} + \frac{\partial \sigma_{yy}}{\partial y} dy\right) dx\right] + \left[-\tau_{xy}dy + \left(\tau_{xy} + \frac{\partial \tau_{xy}}{\partial x} dx\right) dy\right]$ then reduced to,

$$F_{surface,y} = \left(\frac{\partial \sigma_{yy}}{\partial y} + \frac{\partial \tau_{xy}}{\partial x}\right) dxdy \tag{2.82}$$

The body force is defined with $f_x$and f_y body force components like gravity per unit mass for the x and y directions:

$$F_{body,x} = \rho f_x dxdy \tag{2.83}$$

$$F_{body,y} = \rho f_y dxdy \tag{2.84}$$

After applying Newton's second law of motion, the following equations are obtained:

x direction: $\rho dxdy \frac{Du}{Dt} = \left(\frac{\partial \sigma_{xx}}{\partial x} + \frac{\partial \tau_{yx}}{\partial y}\right) dxdy + \rho f_x dxdy$ then yields,

$$\rho \frac{Du}{Dt} = \rho f_x + \frac{\partial \sigma_{xx}}{\partial x} + \frac{\partial \tau_{yx}}{\partial y} \tag{2.85}$$

y direction: $\rho dxdy \frac{Dv}{Dt} = \left(\frac{\partial \sigma_{yy}}{\partial y} + \frac{\partial \tau_{xy}}{\partial x}\right) dxdy + \rho f_y dxdy$ then yields,

$$\rho \frac{Dv}{Dt} = \rho f_y + \frac{\partial \sigma_{yy}}{\partial y} + \frac{\partial \tau_{xy}}{\partial x} \tag{2.86}$$

where Du/Dt and Dv/Dt state the ratio of the alteration of velocity at the control volume.

The substantial derivate of u and v can be stated in the case of field derivatives utilizing the Euler formula:

x direction: $\rho\left(\frac{du}{dt}+u\frac{du}{dx}+v\frac{du}{dy}\right)=\rho f_x+\frac{\partial\sigma_{xx}}{\partial x}+\frac{\partial\tau_{yx}}{\partial y}$ and the equation is reduced for inviscid flow; $\rho\left(\frac{du}{dt}+u\frac{du}{dx}+v\frac{du}{dy}\right)=\rho f_x+\frac{\partial p}{\partial x}$

y direction: $\rho\left(\frac{dv}{dt}+u\frac{dv}{dx}+v\frac{dv}{dy}\right)=\rho f_y+\frac{\partial\sigma_{yy}}{\partial y}+\frac{\partial\tau_{xy}}{\partial x}$ and for the equation is reduced inviscid flow: $\rho\left(\frac{dv}{dt}+u\frac{dv}{dx}+v\frac{dv}{dy}\right)=\rho f_y+\frac{\partial p}{\partial y}$

The Navier-Stokes equation for non-viscous flow is known as the Euler equation.

The only force for water entry is gravity so body force per unit length is $f_x=0$ and $f_y=g$.

2.7.3 The solver method of differential equations

The finite volume method is chosen for discretization techniques to solve numerically the field functions and boundary conditions. Because the Euler and continuity equations are non-linear partial differential equations and the analytical solutions are insufficient.

2.7.3.1 Integration and discretization of finite volume method

The differential equations of a divided number of control volume are integrated for each volume which then give the fine difference equations. The bound variable is stated at the cell faces in the discrete form. The quadratic differencing scheme (QUICK) has been chosen to state the cell face values and yields a set of linear equations.

2.7.3.2 The set of linear equations solutions

This set of linear equations gives the components of the horizontal and vertical velocity and pressure which are then utilized for mass and momentum formulations. The equations can be performed sequentially and these equations represent the new data of the pressure which is required but it cannot be reached from the mass and momentum balance. SIMPLE (semi-implicit method for pressure-linked equations) are chosen to alter the continuity equation to pressure correction calculations.

2.7.4 The Free surface model

The volume of fluid method is used to define the intersection of water and air. It is possible to obtain flow by pileup, jet flow and water separation. The variables are presented for every fluid in the domain of the VOF method. Specification of the variable is the number of particular fluids in the cell with respect to the fraction of the total cell volume. Each fraction of the volume is followed through the domain and the total of the parts of the volume fractions for all fluids is added to unity within every cell. The fluids split unit set of momentum equations, and the properties of the fluid depend on the volume fraction of the fluids in it. The values of the properties are obtained as a volume fraction. The free surface has the value of 0.5 volume fraction for every adjoint fluid. (Trym Tveitnes [74])

CHAPTER 3

EXPERIMENTAL SETUP

For the experimental investigation, a drop test setup has been designed and constructed to measure the hydrodynamic effects on various bodies entering water. An image of the experimental setup for drop tests is given in Figure 3.1. It composes two parts, one of the railing sections and other is water basin section. It is constructed with 45 mm wide aluminum profiles and 10 mm thick acrylic sheets. The frame is firmly fixed to the floor and to a concrete beam at four different locations. This frame contains four vertical legs of 5 m in length on the sides, and a 1.7m long, 1.0m wide and 1.2m deep water basin at the bottom. The four railing system was established to prevent rotation and its height is 4 m. The rail has been embedded in side of the aluminum and attached the trolley by bearing. The model test is mounted to the trolley and can be easily disassembled and assembled. The test bodies fall due to gravity into the water. This experimental setup is designed for specimens to be dropped from the heights of 0.05 m to 4 m. The five different free fall drop heights have been evaluated at the measuring water entry effect and there are 30 cm, 50 cm, 60 cm, 75 cm and 1 m for cylinder and sphere shape water entry test. In addition that some other drops height experiments are applied for wedge and ship model test. All experiment has been repeated at least five times. The sliding mechanism was hold by special releasing mechanism which is composes rope with integrating concentric circles and the circles are releases when the interaction remove thus free fall of the specimen to water surface have been accomplished. The water basin is made of acrylic sheets allowing observations from any direction and was filled with water only up to 0.8m. It has been cut with appropriate size and the edges have been integrated by special adhesive. The water didn’t fill all depth to prevent water leakage from water basin. The setup was equipped with four guiding rails on the legs to prevent the carriage fixture from rotating or moving horizontally, assuring the verticality of impacts. The release application has been made by helping of interwoven of three hoops at the upper side of interaction of trolley and carrier rope. The connection of interwoven of three hoops are provided by small bar.

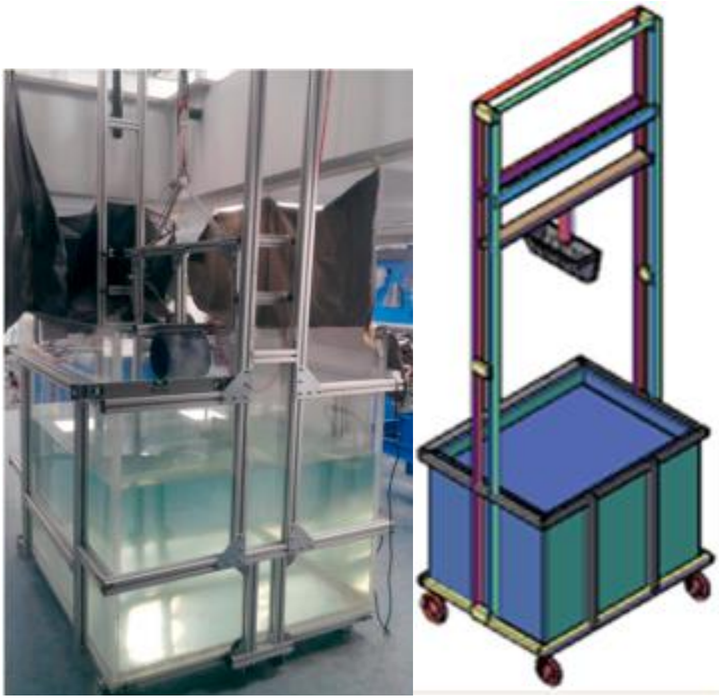

Figure 3.1 The experimental drop weight setup

With removing the bar unit from undermost hoop, the all hoops are become free. So the trolley with carrier rope is disconnected and free fall can be performed. After the earning the acceleration of the trolley, it becomes free at the stage of the entrance of the free surface. So the trolley doesn’t have interaction with railways on aluminum profile.

3.1 Test Models

The advanced deadrise angle shapes tests were carried out using one spherical and two cylindrical models. The geometric and the mass values of the test objects can be seen in Table 3.1. The drop height in the setup can vary from 0.05m to 4m above the calm water level, corresponding to impact velocities of up to 9 m/s. The first cylinder model is made of UPVC, second one is of aluminum and the sphere model is made of acrylic.

Table 3.1 The geometric and the mass values of the test objects

	Cylinder (C1)	Cylinder (C2)	Sphere (S1)
Mass (with carriage)	16 kg	11 kg	12 kg
Diameter	22 cm	12 cm	30 cm
Wall thickness	1 cm	0.2 cm	0.4 cm
Material	UPVC	Aluminum	Acrylic

The main advantage of using a cylinder and a sphere (figure 3.2) is that they have a varying deadrise angle along the circumference. As such, climbing of water on surface at low velocities and separation of water at high velocities, on the same object, can be visualized and pressure measurements are possible at different deadrise angles. Studying slamming with varying deadrise angle has gained importance especially in designing offshore platforms and ship bulbs.

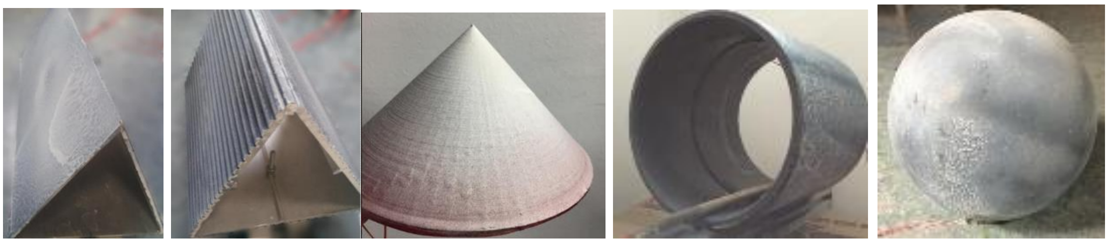

Figure 3.2 Test bodies for constant and advencing angle samples

Figure 3.2 shows also the geometry that used for second types of experiments sequence. The six different deadrise angles have been chosen for wedge and conical shapes to investigate the impact dynamics with constant deadrise angle. These shapes can represent the bottom of ship structure and pontoon. The comparison is made for wedge shapes in itself by varied deadrise angle, and then they are compared with cone shapes. The importance of deadrise angle is demonstrated by investigating four different angles and these are 7.5°, 30°, 45° and 60° degree. The second comparison has been performed for conical shapes. The cone objects have 30° and 45° degree of deadrise angle. The five drop height is performed for wedge and conical shapes and they are 30°, 40°, 50°, 60° and 75 cm. The only 60° degree of deadrise angle wedges are made of aluminum and all the others material is Polylactic Acid (PLA).

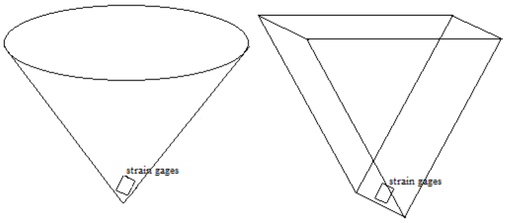

Figure 3.3 The places for applied strain gages

Another important parameter is water entry velocities. These experiments are carried out by releasing specimens with different heights to simulate the effect of different impact velocities. The strain gages are implemented the inner side of specimens to measure impact effects and these gages are employed exactly at the same positions which are arranged from tip for all specimens. The place of mounted strain gages are demonstrated at figure 3.3.

A vacuum mechanism is added to the setup for holding and releasing the test ship model specimens. The specimens were manufactured by a 3D printer and made of PLA with a wall thickness of 2 mm. The distance from the tip of the specimen to free surface is adjusted via a sliding mechanism positioned on the aluminum frame. Thus, the entrance velocity can be controlled by changing the drop height of the specimens. Each test was carried when the system was free of any wave and vibration to assure repeatability. The dimensions of bulbous bow section are 15cm by 14 cm with a mass of 432 gr. The catamaran section is 16cm by 16 cm in dimensions with a mass of 225 gr (Figure 3.4). The test bodies were released from the heights of 0.3 m to 0.75 m.

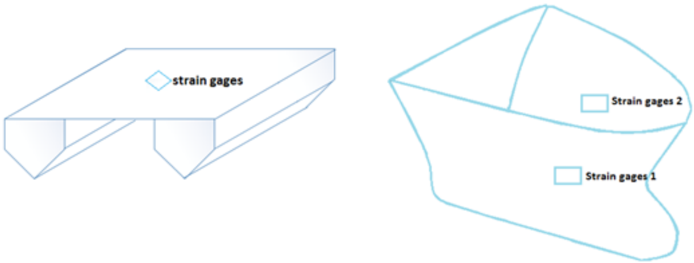

Figure 3.4 Ship models and the place that applied strain gages

The water exit tests were carried out using a sphere, a flat plate and cylinder. The sphere is of acrylic with a diameter of 20 cm and a mass of 800 gr for partially immersion tests and another one with a diameter of 6 cm and a mass of 20 gr for fully immersion tests. The flat plate is made of wood with the dimensions of 40x25x2 cm and a mass of 1250 gr. The material of the cylinder is acrylic and the dimensions are 10cm for diameter and 20 cm for length. The cylinder shapes is also used for fully immersion test.

The water exit experiments were conducted in a prismatic basin allowing measuring the hydrodynamic effects of partially and fully submerged rigid bodies exiting water. A schematic view of the experimental setup is given in Figure 3.5. It is originally designed for carrying out drop tests and has a water basin of 1.7m in length, 1.0m in width, and 1.2m in depth. The water basin is made of acrylic sheets (10mm thick) allowing observation from any direction. For the exit tests of fully submerged bodies (sphere), the release of the test objects in water are regulated by help of a small pulley attached to the bottom of the tank. Test objects are tied with a thin fishing line from their bottom and the other end of the fishing line goes through the pulley at the bottom, then to the outside of the tank. With the release of the fishing line in one end, the sphere moves upward under buoyancy effects. For the exit tests of partially submerged bodies, another pulley is attached on an aluminum frame placed on the top of the tank, and the objects pulled out of the water by dropping some weights attached to the other end of the fishing line holding the test bodies. Thus, the initial exit velocity can be controlled by changing the drop height of the weights. For each test case, it started when everything is at rest, to make sure no secondary flows or effects are present in the flow domain.

The release height in the setup can vary from 0.01 m to 0.9 m below the undisturbed free surface.

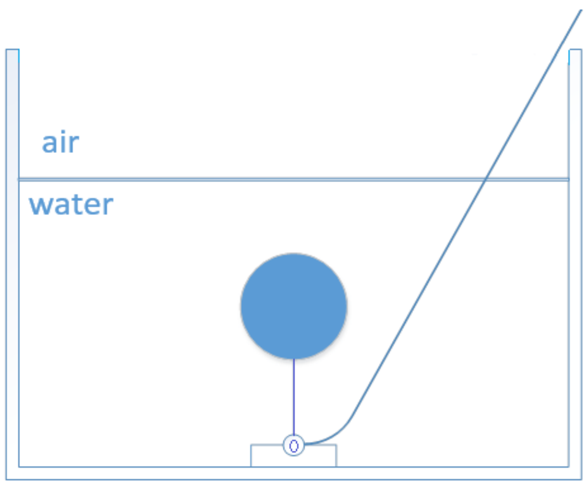

Figure 3.5 Schematic view of the test tank

3.2 Strain gauges

Strain gauges are used to measure slamming impact deformations. The fundamental aspect of the measurement of the strain gauge is that during deformation, the metallic foil pattern is also deformed and this deformation comprises electrical resistance. The electrical resistance differences are measured by the Wheatstone bridge and are connected with the gauge factor. The strain gauges used illustrated in figure 3.6.

The test objects used in the experiments are cylindrical, spherical, wedge, conical and ship models, so that measuring the strain is analogous to measuring the impact force directly. From high speed camera images, it can be observed that the impacts cause elastic deformations in all test bodies. Deformation of the test bodies during the experiments is measured by three water-proof strain gauges placed in the azimuthal direction for the cylinder and spherical shapes. The strain is attached to at the tip of the shapes in the direction of the chines for other test objects. These strain gauges (Type WFLA-6-11-3L by Tokyo Sokki Kenkyujo Co. Ltd.) are installed on the inner surfaces of the test bodies. One strain gauge is installed at the bottom of each body and the other two are placed at the angular shift of 10° and 30° with respect to the bottom strain gauge for the cylinder. They are all oriented towards the same direction. The strain recordings are directly proportional to the local stresses, thus correlating with the impact forces. In this study, a sampling rate of 10 kHz was used for the strain recordings. These recordings were compared with the ones obtained at 25 kHz at the beginning, to ensure the 10 kHz sampling rate is good enough to sufficiently cover the peak region of sudden impacts.

Deformation of the surface was measured by the strain gauges and normalized by the well-known force. Thus, strain and force interaction have been determined. Therefore the strain values that are obtained from water entry tests can be converted to force values by the formulation of the strain-force interaction. The strain gauge properties are given in table 3.2.

Table 3.2 Specifications of strain gauges

Type	Gauge length (mm)	Gauge width (mm)	Backing length (mm)	Backing width (mm)	Backing thickness (mm)	Resist-ance (Ω)	Strain limit	Gauge Factor
WFLA-6-11-3L	6	2.2	25	11	1.5	120	3% $(30000 \times 10^{-6}$strain	2.12

Figure 3.6 Sample of strain gauges

3.3 High speed camera

A high speed camera (Phantom Miro eX4) was used to record penetration of the impacting bodies and the formation of water uprises and splashes (figure 3.7). In all test cases, the image resolution, brightness and clarity were considered; resolution was 640 x 480, the recording speed of the camera is optimized and the high speed images were taken at 1400 fps in order to understand the physics and dynamics of the impact phenomenon (table 3.3). The velocity measurement of the test bodies including the impact velocity and the splash propagation were determined via these images. The technique for extracting the velocity with the high speed camera is based on the data obtained from the position measurement of the test object in the images and the change in time frame of the high speed camera images i.e. the displacement versus time. To double check the position of the bodies (eliminating the effect of flexibility), the carriage fixture that holds the bodies is also tracked in each time step.

Figure 3.7 The High speed camera Phantom Miro ex4

Visualization of the behavior of the model test can be carried out by employing lighting which is significant to the water entry process. A Light Emitting Diode (LED) was used at the direction opposite to the high speed camera. Thus, the processes of the model test showed clearly and comparisons were made by a cine viewer application program.

Table 3.3 Specifications of High Speed Camera

Specifications	Miro ex4
Maximum Resolution (pixel)	800*600
Frame per seconds at full resolution (fps)	1260
Frame per seconds at low resolution (fps)	11100

3.4 The Data Acquisition System

The data acquisition system is used to obtain the strain values from the strain gauges. The system composes two parts: the C-DAQ chassis (National instrument DAQ-9174) and the modulus which is integrated to the chassis and connected directly to the wires by the strain gauges (figure 3.8). The chassis has four sockets for the modulus and the modulus is generally prepared for specific measurements. The NI 9235 modulus strain gauges and specifications are demonstrated in table 3.4. The measurement application is implemented by the LABVIEW software program. The trigger, measurement and transferring of the data are performed by this program. The NI 9235 performs the quarter Wheatstone bridge for each connected strain gauge. The shunt calibration is implemented for the strain gauges at each measurement.

Figure 3.8 Data Logger and its chassis

Table 3.4 Specification of data logger

NI 9235	Differential Channels	Analog Input Resolution	Maximum Voltage Range Accuracy	
	8	24 bits	-29.4 mV / V - 29.4 mV / V	0.02957 mV / V

CHAPTER 4

THE EFFECT OF FLEXIBILITY

This chapter presents the ratio of the material flexibility on water entry test for some shapes. The hydrodynamic loads on surface can't be calculated or measures by assuming the full rigid material. The structural deformation can change the impact dynamics and it can be become the reason of degreases the impact forces. Because this type of material can absorb the impact effects and less forces can measured. Additionally, the more deformation is also observed on the flexible material at water entry and so the fluid motion can change. Therefore the wetted area can change and the numerical approaches can be concluded truly. The results of this structural deformation; the amount of air between structure surface and deform water can be differ with assumed rigid structure. This air composes extra damping effect that is called air cushion effect. Also the change of the fluid path is the reason of negative pressure. Therefore the structure deformation is the important parameter for water entry cases.

Two types of cylinder are used for advanced deadrise angle shapes in the drop tests for studying flexibility, a flexible one (C1) made of UPVC and a relatively rigid one (C2) made of aluminum. During the water entry of a flexible cylinder, the cylinder initially tends to deform as an ellipse right after the impact (Panciroli et. al. [75]). Deflection is proportional to impact load. According to thin ring theory, the circumferential flexural rigidity (pipe stiffness) is comprised of material stiffness (E) and geometric stiffness (I/Rm3). Deflection decreases as pipe stiffness increases. Flexural stiffness (pipe stiffness, ring bending stiffness) is given by the equation

$$FS = \frac{EI}{{R_m}^3} \tag{4.1}$$

where E=elasticity modulus, I=second moment of inertia and R_m=mean radius. Although the elasticity modulus of the pipe materials is not provided by the manufacturers, the E values of UPVC and aluminum cylinders from the other international pipe manufacturers were used in calculating the flexural stiffness. Taking E_{AL}=70 GPa and E_{UPVC}=3.7 GPa from the other manufacturers, the flexural stiffness of the aluminum cylinder is almost four times larger than the one of the UPVC one. The ratio of the flexural stiffness between the test cylinders was also checked before the experiments. Static compression tests were carried with the test cylinders to characterize their resistance to ring (hoop) deflection. Seven different loads were applied with a line contact on the cylinders and measured the vertical deflections and the circumferential strain values in the approximate range of 50 - 1000 microstrain. It was seen that the percentage deflections and the strain values were two times higher for the UPVC cylinders under the same loads. Percentage deflection is calculated as a percentage of the initial diameter and is a function of EI/Rm2. Thus, UPVC cylinder is more flexible than the aluminum one.

It is known that deformable objects experience less slamming forces. Blommaert et al. [76] performed slamming tests on both a rigid and deformable cylinder to investigate the influence of the deformation on the peak pressures. The cylinders were dropped from a height of 1000 mm. The peak pressure measured was about 730 kPa for the rigid cylinder while it was much lower, 335 kPa (almost a factor of two smaller), for the deformable one. Van Nuffel [65] carried out careful drop test experiments with rigid and flexible cylinders and showed the effect of deformability. They also showed the importance of the sampling rate, location and position of the pressure sensors and how they would influence the outcomes of the experimental results. Panciroli et al. [75] carried free fall drop tests with a flexible thin cylinder and analyzed the structural deformation and the distributed strain field via modal decomposition method. They concluded that flexibility of the structure creates different impact dynamics comparing to the impact of rigid structures.

CHAPTER 5

THE EFFECT OF HYDROPHOBICITY

If a water droplet resting on a solid surface forms a characteristic contact angle of larger than 90°, the surface is named as hydrophobic, otherwise hydrophilic. Super hydrophobic surface is referred to have contact angles exceeding 150° and the roll-off angles (hysteresis) less than 5°. In the wetting state of Cassie-Baxter's, water particles sit on a mixture of solid and air and cannot penetrate into between the corrugations on the solid surface, thus causing air pockets to be trapped under it, resulting in less contact area between the solid surface and the water. If there is only air under the droplet, it is predicted to be a contact angle of 180°. Coating can also induce similar corrugation on solid surfaces, causing water drops to move or even bounce during interactions with solids.

From the literature, it is known that hydrophobic surfaces can cause slippage as water flows on them. Therefore, a hydrophobic surface reduces the drag in microscale flows for both laminar and turbulent flow regimes (Daniello et al. [77]). A parameter often used in the literature to quantify the drag reduction is the slip length. The slip length is defined as the ratio of the velocity of the water layer in contact with the surface (slip velocity) to the velocity gradient at the surface, in other words, the distance inside the solid wall for which the velocity profile of flowing water vanishes. At high Reynolds number flows, hydrophobic surface's direct effect on the drag force acting on a moving object seems disappointingly small (Duez et al. [66]). But in the phenomenon associated with the entry of a solid body into a liquid, the surface wetting properties determine the way the liquid connects to the solid to form the contact line, demonstrating that the unique properties of super hydrophobic surfaces are indeed capable of modifying the macroscale hydrodynamics (Duez et al. [66]). Duez et al. [66] carried out experiments by impacting spheres and showed that hydrophobicity promotes air entrainment.

A hydrophobic spray coating, WetProof Super Hydro by WetProof Inc., is used to prepare hydrophobic surfaces on the test bodies. The coating is in the order of micrometer, so did not affect the radii and not change the density of the bodies, only increased the contact angle on the surfaces. Although the coating is durable enough to carry 7-9 sets of experiments, the test objects were recoated every third set of experiments to make sure the repeatability of the results. In doing so, the old coating was removed before the new coating was applied.

The coated consist of two parts, first part is base coat that is prepare the surface and increases the holding rate of the second coat. After the spraying first coat, the sample leaves at rest for half an hour. The second layer is coated by top coat and one day is needed to get dry and take best result. The coated application is performed by helping compressor that is also useful for equal distribution of coat material.

With change of surface parameter, the reaction of free fall object became a diversified. These surface characteristics can modify by hydrophobic coated. After the completing free fall test with regular surface, the same experiment has been made by implementing hydrophobic coated with micron thickness to the surface. The hydrophobicity effect has been shown by strain measurement and interaction fluid and structure at penetration process. The pileup and splash are described for water entry problems and composed a dimensionless value to be clarity. The separations of water, generation of pileup and splash characteristics have been demonstrated by recording the penetration process of specimens by high speed camera. The slamming coefficient and wetting factor have been calculated both untreated and hydrophobic surface experiments.

CHAPTER 6

WATER ENTRY OF CYLINDERS AND SPHERES UNDER HYDROPHOBIC EFFECTS; CASE FOR ADVANCING DEADRISE ANGLES

The results of an experimental investigation of water entry of spherical and cylindrical shaped objects with hydrophobic surfaces are presented in this chapter. The test specimens have a varying deadrise angle. Drop tests have been set up for studying slamming by dropping test objects from various heights toward water surface. Different fluid dynamics phenomena like jet formation, cavity formation, water splashing and flow separation on solid surfaces are investigated and compared with under hydrophobic effects. From digital images captured using a high speed camera, pileup coefficients and splash velocities are measured. It is observed that flow separation occurs earlier with hydrophobic surfaces causing no pressure pulse occurrence on the solid surface at larger penetration depths. Hydrophobicity also causes larger pileups with faster jet flows indicating more kinetic energy transference to the fluid. Along with high speed imaging, the impact loads are calculated and compared with when hydrophobicity is present via strain gauge measurements. It is found that the peak strain values during slamming are smaller with hydrophobic surfaces promoting a reduction in the impact forces while distributing the pressure pulses on a larger wetted area.

The results presented here are for the initial drop heights varying from 150 mm to 1000 mm. For these drop heights the theoretical water entry velocities vary between 1.72 m/s and 4.43 m/s, however, real velocities are measured via high speed camera images as 94-98% of the theoretical values due to the energy losses on the guide rail system and the air drag. This difference is larger at higher velocities with increasing drop height.

When an object enters vertically into calm water in a free fall, its vertical velocity remains unchanged for a short period of time at the beginning of the impact. At this very initial stage, the impact creates spray with free surface following the first contact. Then the penetration velocity decreases as the body moves further down, due to transferring some of its kinetic energy into water and due to increasing displacement, and so buoyancy. As the body decelerates, more kinetic energy is being transferred to the water and the water starts moving outward, called uprising and splashing, and a jet flow occurs rooted at the water line. This is the moment that the body experiences a reaction force called slamming force or impact force. The slamming force and the characteristics of splash are dependent on the entrance velocity and the shape of the body. It is shown that the temporal and spatial pressure variation on the wetted length is related to splash characteristics. The location of flow separation affects the pressure variation on the surface (Sun [78]).

As the object further penetrates into water, displaced water keeps raising up and forms water pile-up at the root of jet. Later, as the object fully submerged, a cavity starts forming behind the object. Initially, the cavity is filled by air, and the water around the cavity is further pushed outward to the sides while transferring more water into the pile-ups and jets. After a certain penetration depth, depending on the entrance velocity, the cavity closes and is filled with water and air. This common phenomenon of the slamming impact can be seen in Figure 6.1 and Figure 6.2 for the test objects of a cylinder and a sphere. Figure 6.1 shows the snapshots of seven different instants in time (early and late stages of impact) of the sphere (S1) and the cylinder (C1) penetrating the free water surface, dropped from 150 mm, and Figure 6.2 shows the same for 500 mm drop height. The terms that are mentioned before like splash, pileup, jet flow and air cavity are visual in Figure 6.1 and Figure 6.2. One thing to notice in this figure is that the hydrodynamic phenomenon of the impact on the left side of the objects is different than the one on their right side. It is the hydrophobicity that causes the difference in the characteristics of splashes and the air cavity behind between the two halves even though they experience the same hydrodynamic effects. It contributes early separation, no water climbing on the surface and larger air cavity behind onto this phenomenon (Guzel and Korkmaz [78]).

From these images the creation and the propagation of a jet along the body surface can be clearly seen and quantified. Normally at higher entrance velocities, the jet is detached from the surface as the local deadrise angle increases in the case of sphere and cylinder slamming. The magnitude of the velocity of the jet generated by the impact is very large. As the angle increases, the speed of the jet decreases (Chung et al. [80]). The increasing deadrise angle may result in a detachment of the jet from the body surface (Battistin and Iafrati [18]). Battistin and Iafrati [18] showed that when reducing the deadrise angle the kinetic energy tends to be equally shared between the bulk of the fluid and the jet and a larger fraction of the kinetic energy flows into the jet in the axisymmetric case compared to the two-dimensional one. Moreover, how the jet flow is detached from the object is dependent on the surface properties as well. It can be observed in Figure 6.1 and Figure 6.2 that the amount of pile-ups on both sides is different. Figure 6.3 shows the time at which the center of the cylinders reached the undisturbed free surface for all drop heights.

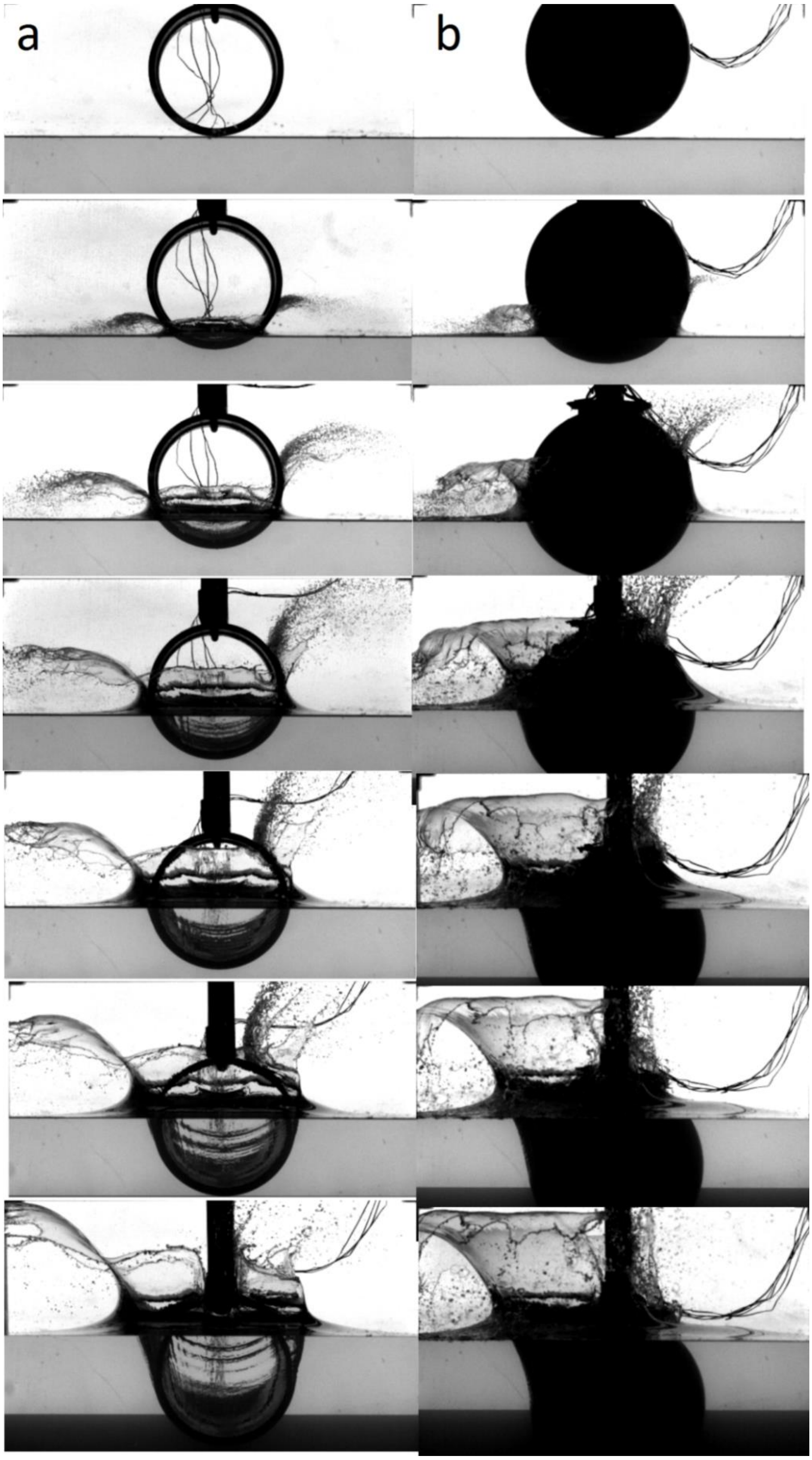

Figure 6.1 Snapshots taken at different time steps of the water entry of (a) cylinder (C1) dropped from 0.15 m (0, 14, 28, 42, 57, 71, 96 ms) and (b) sphere dropped from 0.15m (0, 29, 58, 87, 117, 131, 146 ms). The left half is treated with hydrophobic coating in both cases.

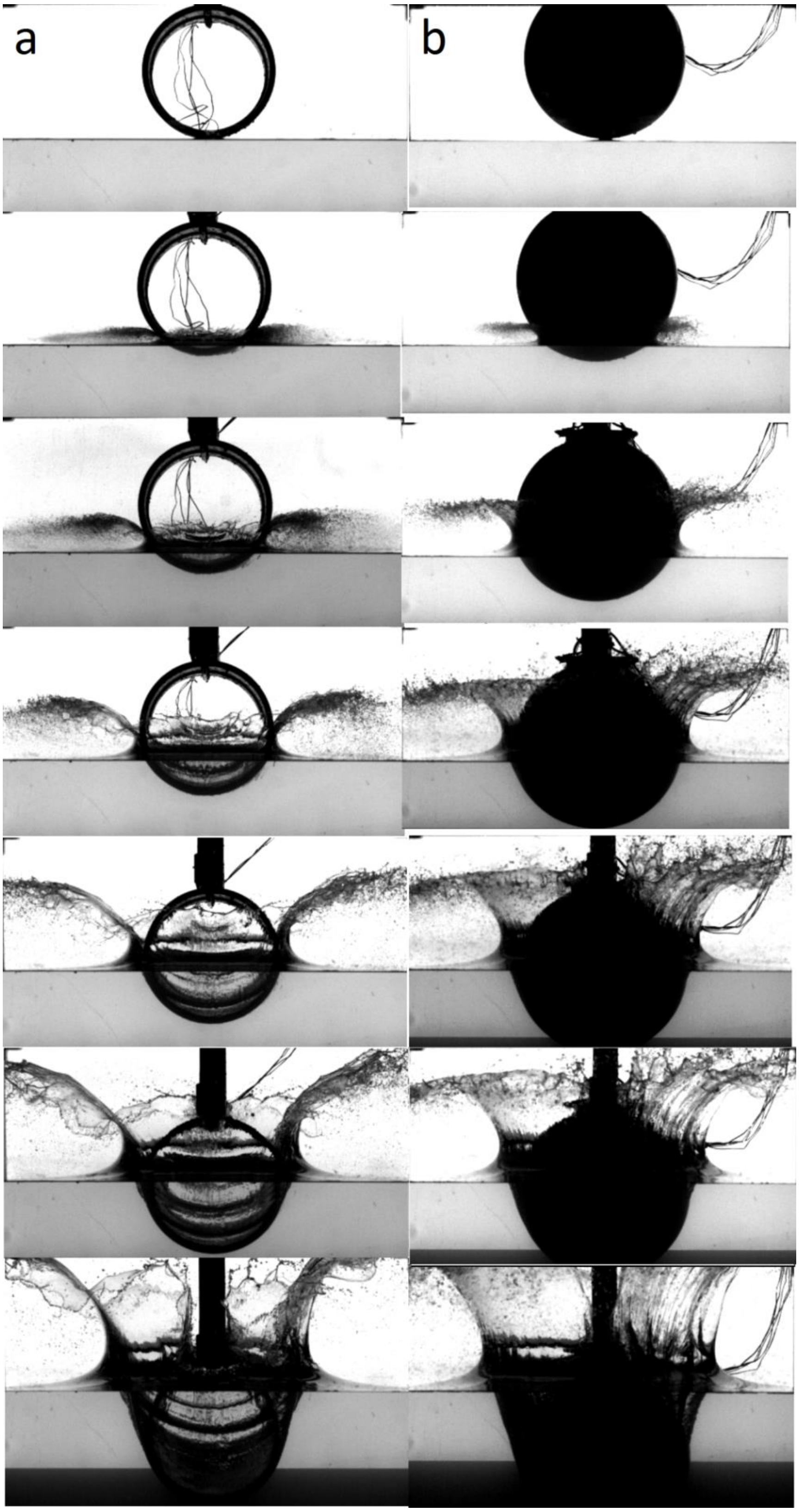

Figure 6.2 Snapshots taken at different time steps of the water entry of (a) cylinder (C1) dropped from 0.5 m (0, 6, 13, 21, 31, 42, 66 ms) and (b) sphere dropped from 0.5m (0, 11, 29, 43, 53, 61, 95 ms). The left half is treated with hydrophobic coating in both cases.

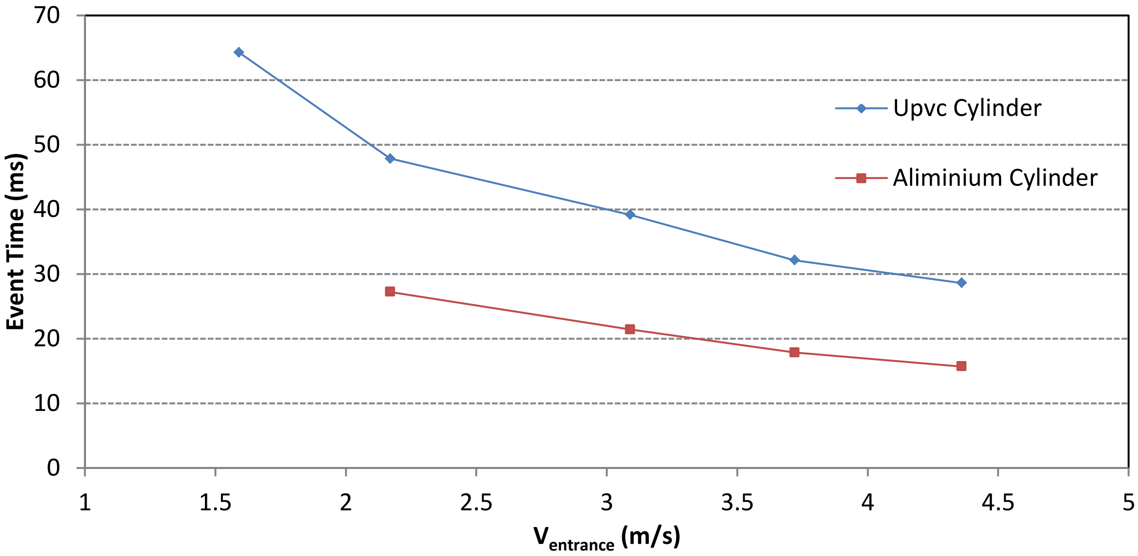

Figure 6.3 Time at which the center of the cylinders reached the undisturbed free surface

In model development for the impact force prediction, some assumptions and significant simplifications are usually considered to achieve the appropriate design criterion. For water, it is modeled as an incompressible, irrotational, inviscid, and for the body, it is taken as rigid with a uniform wall thickness. Some other factors such as elastic deformations, oblique or asymmetric entry, and complex geometries even further complicates the understanding the impact mechanism.

For simplicity in understanding the effect of the change in surface properties in slamming, cylinder and sphere are chosen for being the main geometry. The first reason for choosing these two geometries as a test model is to avoid air cushioning effects on the slamming loads, which is very crucial in experimenting with hydrophobic surfaces. For these geometries, the air can escape quicker along the sides of the test objects. And the second reason is that the sphere and the cylinder are subject to much higher slamming coefficients in the bottom area than the wedges and the cones due to small values of the local deadrise angle (G. De Backer et al. [22]). So it would make it easier to compare the impact forces under the different feature of the surface characteristics.

The equation of motion of a water-entering object can be written as

$$\Sigma F = M\ddot{\zeta} \tag{6.1}$$

$$Mg - F - F_b - F_c - F_d = M\ddot{\zeta} \tag{6.2}$$

where ζ is the penetration depth relative to the still free water surface (Abrate [7]).

Considering the force balance on an object entering the water, inertia force (Mg), buoyancy force (F_b), drag force (F_d), capillary force (F_c), and the impact force (F) which is the force that is applied by the fluid on the object are the forces to be considered. In real slamming events, whether for ships on seas or for models in lab-scale drop experiments, Reynolds number, Froude number and Weber number are large enough to neglect the viscosity, gravity and surface tension effects in model development and in force prediction calculations. The drag force and the buoyancy force are only important at larger submergences. Thus, in literature, the attention is paid to the sudden acceleration of a certain mass of water, the added mass, after the impact, while the jet flow and the pileup is often neglected. From the Figure 6.1, another uncertainty adds up to the problem; does hydrophobicity change the characteristics of the added mass, such as its mass, its shape, its evolution or its acceleration? Does changing the water rise up characteristics has any effect on the slamming forces?

Working within the frame of the conservation of energy, it is realized that the jets and the water rise-up should be taken into account in the energy balance. In the case of the drop test experiments, depending on the height, the object has certain potential energy with respect to the free water surface, just before it is released from its stationary position. This potential energy is equal to the total kinetic energy prior the first contact at the free surface (neglecting the air drag). When the object hits the free surface, some of its kinetic energy is transferred to the fluid during the impact. Cointe and Armand [69] and Payne [81] carried out energy analysis by using asymptotic theory and concluded that, for a constant vertical impact velocity, half the work performed by the object would seem to be transferred to the fluid as kinetic energy within the spray. And the other half is transferred to the surrounding bulk fluid and absorbed and stored in it for a short period of time.

To compare and to quantify the kinetic energy transfer to the water in slamming under the different surface characteristics, first of all a new pileup coefficient is defined, in such, comparing the ratio of the amount of water in pileup to the displaced water as the object submerges. This chunk of water, pileup, not only holds some of the displaced water but also carries some of its kinetic energy within it because it moves outward of the body as chunk. The rest of the displaced water is moved away within the jet and the splash, with the rest of the kinetic energy that is transferred to the water rise up. This energy is considered to be 50-80% of the energy transferred to the water (Cointe and

Armand [69], Panciroli et al. [29]). The other half is stored in the bulk of the fluid. In this study, the pileup coefficient, C_{pw}, is defined as follows;

$$C_{pw} = \frac{h_p * t_p}{A_p} \tag{6.3}$$

Where h_p is the pileup height, t_p is the pileup width and A_p is the area of the displaced water. The parameters h_p and t_p are defined in a way that they correspond the outer boundaries of pileups. With this definition, the mass of water in pileups because pileups keep moving outward even after separated from the object. h_p is the distance to the jet root from the undisturbed free surface. t_p is the distance to the midpoint of the upper edge of the pileup from the lower right corner of the pileup which coincides with the undisturbed free surface.

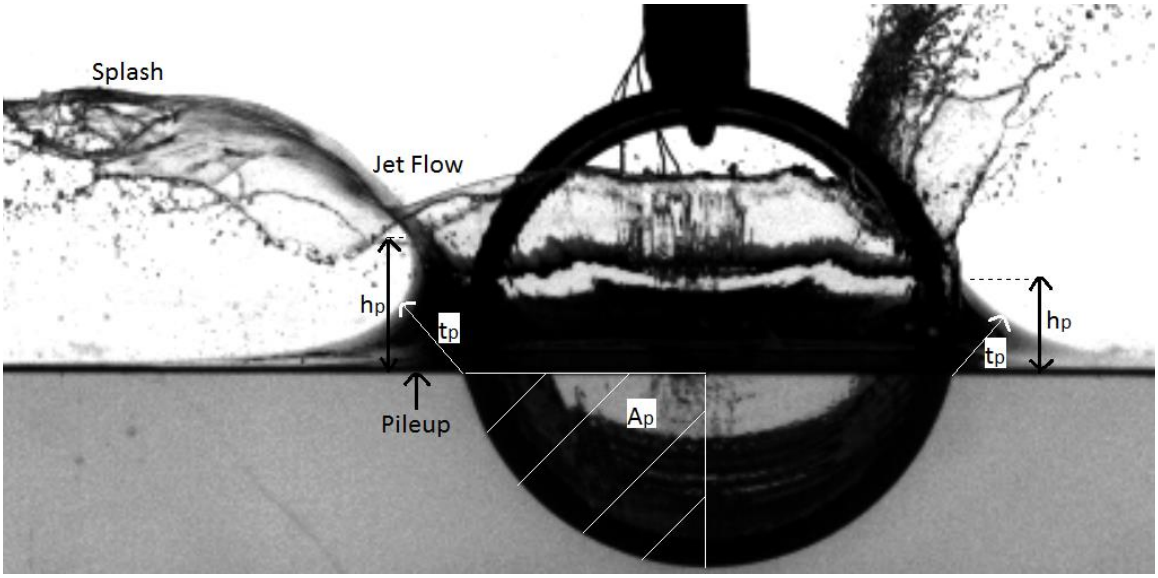

Figure 6.4 shows the pileup height, h_p, the pileup width, t_p and the area of the displaced water, A_p on an actual image taken during a slamming event of the cylinder C1

Figure 6.4 A high speed video image taken during a slamming impact of the cylindrical test object showing where splash, jet and pile up occur.

Figure 6.5 shows the pileup coefficient values as a function of the dimensionless submergence depth (Ut/R) for slamming of the cylindrical test object (C1) dropped from different heights. For the calculated coefficients of C_{pw} during the impact, an obvious trend can be observed in Figure 6.5. For the untreated surface (UC), the pileup coefficient, C_{pw}, does not change as the object further penetrates. From the C_{pw} definition, it can be said that the amount of water in pileup is linearly proportional to the displaced water. On the other hand, for the hydrophobic coated surface (HC), C_{pw}

increases with the dimensionless submergence depth, meaning it moves further away from the object with increasing amount of water in it. Thus, it carries more kinetic energy away from the bulk of the water. Since measuring the distances of h_p and t_p is subjective on the black and white images because the location of the jet root is determined w.r.t. its black intensity on the images, other possibility of the h_p and t_p distance values that could be different depending on the light emissivity are taken into account in calculating the coefficients of C_{pw}. Figure 6.6 shows the variation of the C_{pw} values in error bars, calculated based on the different measurements of h_p and t_p distance values from the high speed images. As a reminder, doing these evaluations by taking the flow around the objects as 2D is a valid assumption. Because it is known that there is not large three-dimensional flow effects in similar slamming events except at the very edge of the objects (Jalalisendi [82], Panciroli and Porfirib [83], Nila [84]).

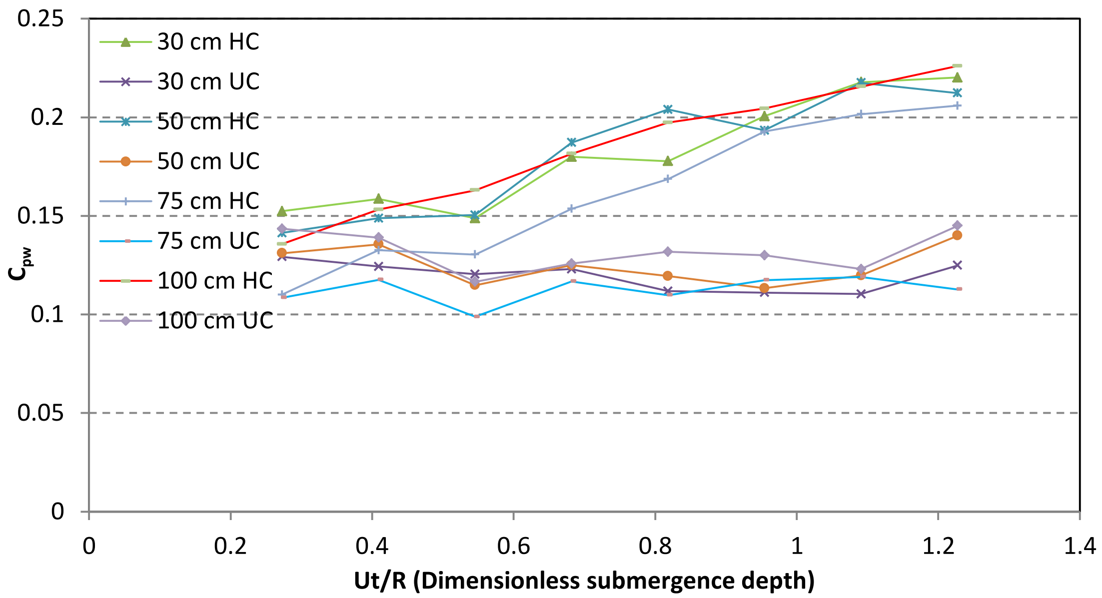

Figure 6.5 Pileup coefficients during the cylinder (C1) impacts as a function of dimensionless submergence depth for the cases of 30, 50, 75 and 100 cm drop heights. UC; uncoated surface, HC, hydrophobic coated surface

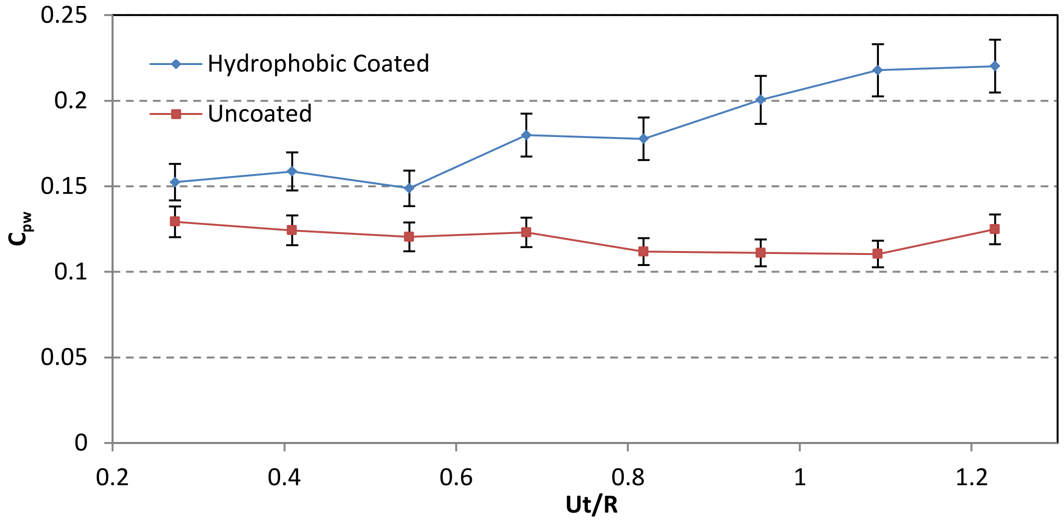

Figure 6.6 Pileup coefficients during the cylinder (C1) impact as a function of dimensionless submergence depth dropped from 30 cm.

Figure 6.7 shows the pileup coefficient values as a function of dimensionless submergence depth for slamming of the spherical test object (S1) dropped from different heights. For the case of sphere, the pileup coefficient, C_{pw}, does not change as the object further penetrates for the both types of surface. In all experiments, C_{pw} is a little larger on the hydrophobic coated side. And Figure 6.8 shows the variation of the C_{pw} values in error bars, calculated based on the different measurement of h_p and t_p distance values.

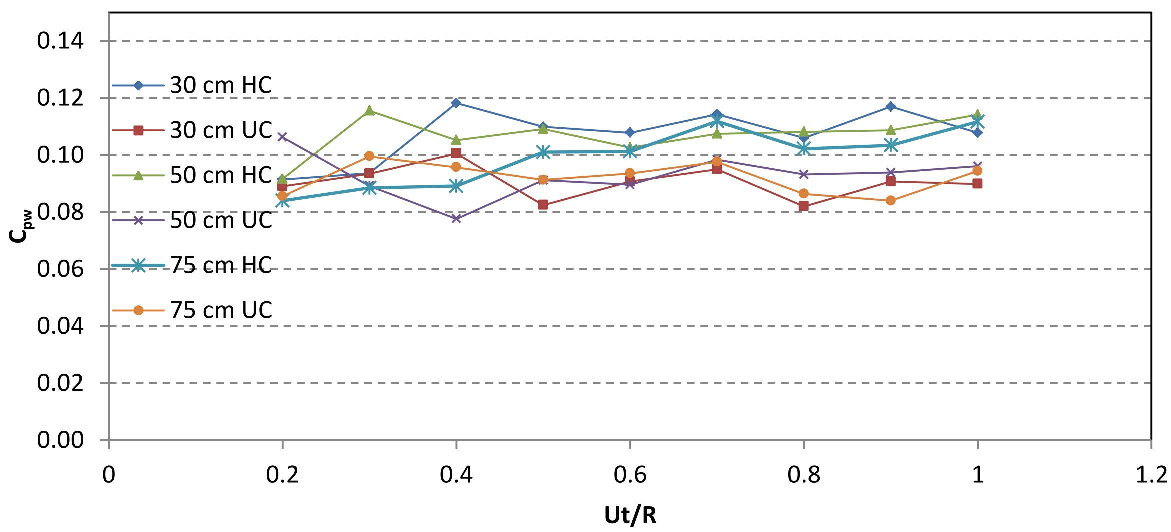

Figure 6.7 Pileup coefficients during the sphere (S1) impacts as a function of dimensionless submergence depth for the cases of 30, 50, 75 and 100 cm drop heights. UC; uncoated surface, HC, hydrophobic coated surface

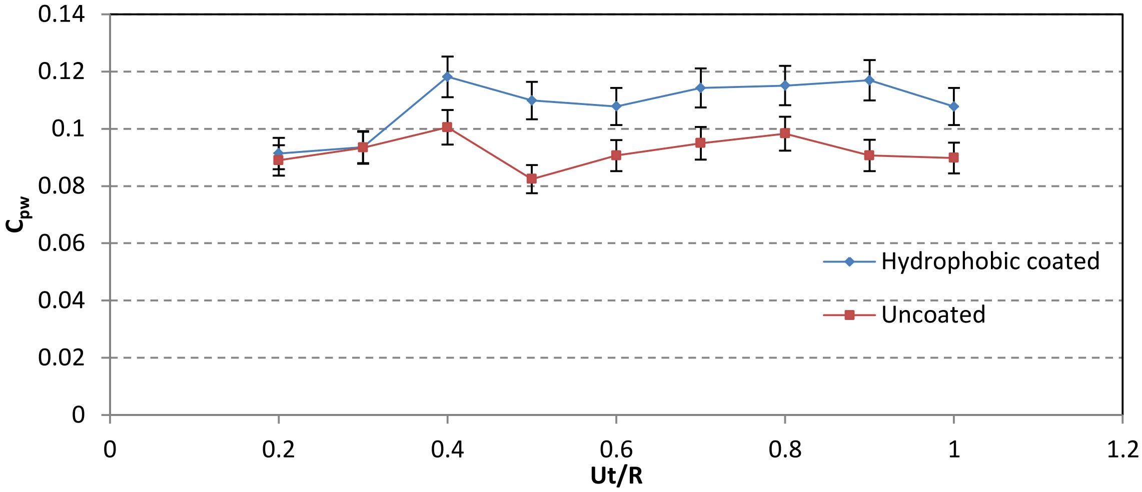

Figure 6.8 Pileup coefficients during the sphere (S1) impact as a function of dimensionless submergence depth dropped from 30 cm.

It can be observed from the high speed images that the entrance velocity can be taken as constant in the impact stage of the drop tests. It is also possible to measure the splash velocities from these high speed camera images. The method of extracting the velocities out of the images is straightforward. For all high speed camera recordings in each experiment, this measurement is done by tracking the leading edge of the splashes. It would be more accurate to measure the average splash velocities rather than the instant velocities. This is due to the difficulty tracking the leading edge of the splashes instantly. Figure 6.9 shows the splash velocities averaged between the time frame at the beginning of the impact (first touch) and the time frames corresponding to the penetration depths of 2.5 cm and 5 cm for test objects of the cylinder (C1) and the sphere (S1). First, the position of the leading edge of the splash is marked at the beginning of the impact, then the distance it has travelled is measured by marking its position when the object submerged 2.5 cm and 5 cm separately. Then, the velocities are calculated based on the differences of the time frames that the two images are taken. It is obvious from these figures that the splashes travel much faster on the hydrophobic coated side for the both objects due to more kinetic energy transferred during the impact.

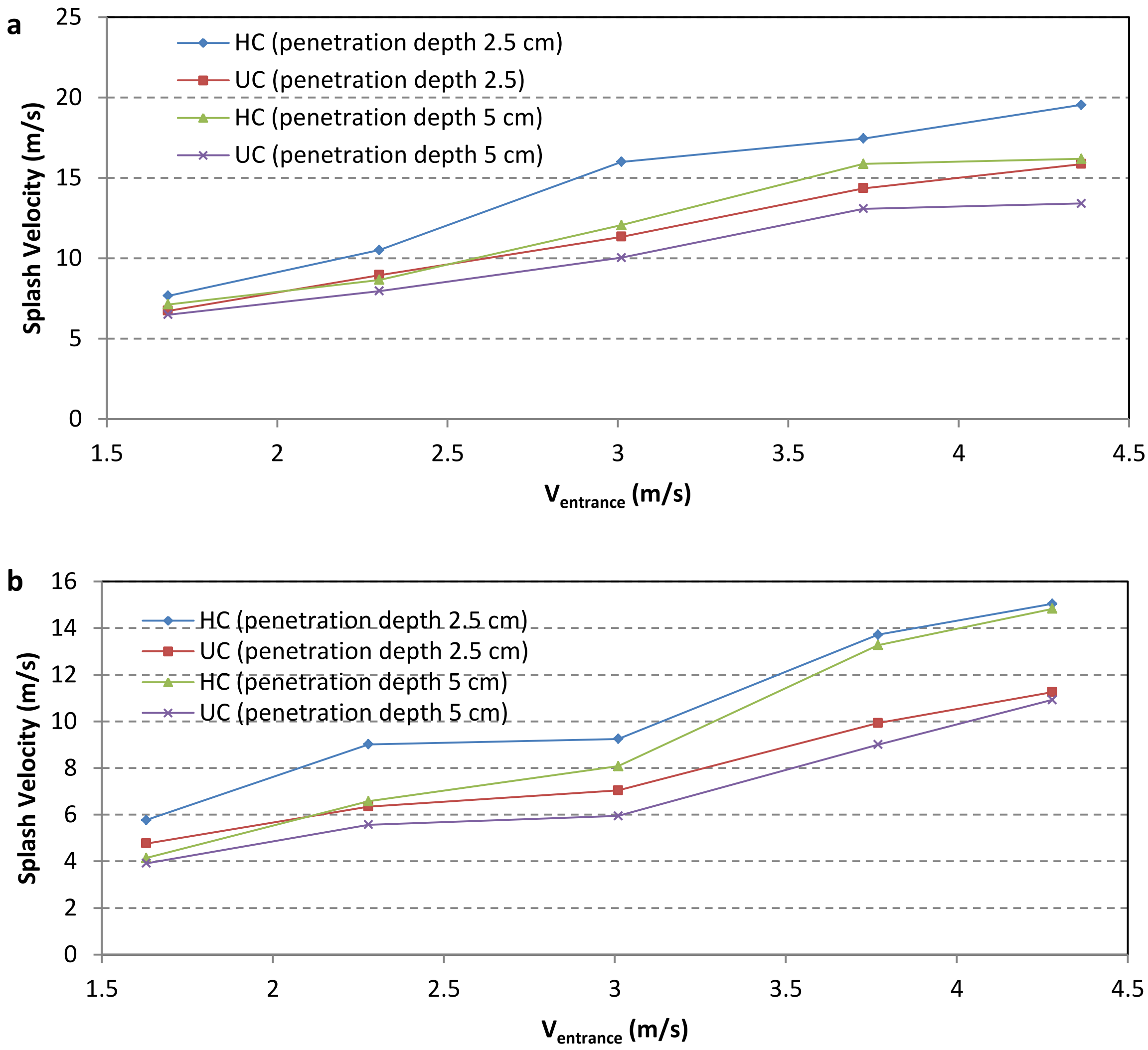

Figure 6.9 Average splash velocities as a function of entrance velocity obtained from the images for (a) Cylinder (C1) (b) Sphere (S1), calculated at the penetration depth of 2.5cm and 5 cm for the drop heights of 15, 30, 50, 75 and 100 cm.

After visualizing and measuring more kinetic energy transference to the water, and knowing that the object keeps moving with less kinetic energy under the effect of hydrophobicity, it can be assumed that the object should slow down quicker comparing to the case with the untreated surface. And, the momentum is also conserved during the impact, then it can be concluded that the object should experience less impact force.

To make this comparison in terms of impact forces, strain gauge measurements are employed with the same test objects for the same drop heights. The velocity vector field of the water flow in the longitudinal direction for the cylinder drop tests is measured by using a PIV technique by Nila[84]. Nila [84] stated that the flow in the longitudinal direction during slamming is negligible throughout the cylinder surface except at the very edges. Jalalisendi [82] experimentally investigated the water entry of a wedge and obtained the 3D velocity field in the whole fluid domain through PIV measurements. They found that the hydrodynamic loading is maximized at the mid-span of the wedge and considerably decreases toward the edges. They also stated that the force per unit length is nearly constant for up to 4.8 cm from the edges. It can also be seen from their results that the three-dimensional effects are quite small at the onset of the impact. Thus, three strain gauges are placed at 5 cm from the edges, on the inner surface of the test objects in the azimuthal direction. Measuring the circumferential strain can give some analogy about the impact force they experience during water entry. Basically, the strain gauges measure the elastic deformations. This deformation is maximum in the direction of the impact force. That's why the first strain gauge is installed at the bottom of the test objects. To eliminate possible artifacts coming from one strain measurement, another two strain gauges are placed at the angular shift of 10° and 30° with respect to the bottom strain gauge oriented in the same direction. The strain recordings are directly proportional to the local stresses, thus correlated with the impact forces. A sampling rate of 10 kHz was chosen as an optimum rate for the strain recordings during the impacts.

Figure 6.10 shows samples of strain time histories for each test object for the drop experiments done with the entrance velocity of 4.36 m/s. The strain recordings are not of periods of sudden peak values but make wide expanse in time because of the nature of the slamming impact that realizes over a wetted area, not a single line contact. So it builds up more gradually in time. It can be seen that after the first strain pulse in the strain time history in Figure 6.10a and 6.10c, there are some oscillations present in the strain recordings due to the oscillatory deformations of the cylindrical test objects, which eventually dampens out in time.

The m−th radial natural frequency of a thin cylinder under plane strain approximation can be written as

$$f_m = \frac{1}{2\pi R^2}\frac{m(m^2-1)}{\sqrt{1+m^2}}\sqrt{\frac{Eh^2}{12\rho(1-v^2)}} \tag{6.4}$$

where h is the cylinder thickness, R the radius, E the Young modulus, υ the Poisson ratio, and ρ the material density (Sun and Faltinsen [85], Panciroli et. al. [75]). The natural frequency of the UPVC cylinder calculated from the Eqn. 5 is found two times smaller than the one of the aluminum cylinder. If the added mass of the carriage is distributed uniformly along the cylinders, and an equivalent density of the shell is used in the equation (Ionina and Korobkin [86], Sun and Faltinsen [85]), the same natural frequencies are obtained for both cylinders. That's why the same period of oscillations in Figure 6.10a and 6.10c is observed.

With increasing flexibility of the cylinders more energy is absorbed by the deformation, resulting in higher strain values. Here, the strain values can be used as a measure for the impact force, and also for the amount of energy absorbed by the deformation. It can be seen from the Figure 6.10 and Fig. 6.3 that the UPVC cylinder experiences three oscillations before its center reaches at the undisturbed free surface, while two oscillations are observed for the aluminum one. The frequency that the cylindrical models deform is present in the strain recordings and is also visible in the high speed camera images. From the images it can be seen that the both cylinders deform into an ellipse. But the deformation is less visible in the case of sphere both in the strain readings and in the images. Since the impact forces acting on the test objects and the strain values measured in the circumferential direction are related and proportional, it is possible to determine the impact forces from the peak strain values if the material properties of the test objects are known. The elasticity modulus of the objects along with the section modulus is necessary for such calculation. It could not be done because the manufacturers of the objects did not provide such information. But still, the peak strain values can be used in comparison for the case where the hydrophobicity is present at the surface of the test objects. The peak strain value depends on the entrance velocity, the wall thickness and diameter of the object (the projected area) and the elasticity of the material. Thus, the comparison can only be made within the same geometrical and material characteristics. In all experiments for the three test objects, the peak strain value with the hydrophobic surface is always smaller than the one with the untreated surface under the same test conditions. This can be clearly seen in the Figure 6.10. The repeatability of the strain measurements is observed under the same test conditions and shown in Figure 6.11. The two different strain 1 values of the repeated experiments done with the same coating in two different days (2 days apart) show high repeatability of the experiments and the durability of the coating.

The experimental studies measuring the impact forces during cylinder slamming is discussed in detailed by Miao [40]. Miao [40] listed the experimental campaigns measuring the impact forces during cylinder slamming and showed that the slamming coefficient, Cs, varied between 2.4 and 6.9 for drop tests in different experimental studies. G. De Backer et al. [22] carried out pressure measurements on sphere and conic shaped objects during a slamming event. It is showed that, during the initial impact at each measurement point along the surface, the pressure peaks steeply to a maximum value. As the body further penetrates into water, the peak pressure value at the measurement points not only drops but also it reaches its maxima much slower as the body slows down. A more peaked pressure distribution is observed as the deadrise angle decreases (G. De Backer et al. [22]). With this information, it can be said that the bottom strain gauge might give some information about the maximum impact force. Nuffel [65] conducted quasi-static compression experiments and carried out compression simulations, and Nila et al. [87] conveyed PIV measurements on the flexible cylindrical objects. They concluded that the flexible cylindrical objects deform elliptically and the slamming load that is distributed over the wetted area can be treated as acting like a line force at the tips of the cylinders. This conclusion proves that, during the water entry of a deformable cylinder, the impact forces and the deformations measured by the strain gauges are result of the same dynamic nature and can be related, thus making the conversions from one to another possible.

The entrance velocity represents the initial total kinetic energy of the test objects at the moment of the first water contact. Thus, it is the dominant parameter that effects the impact force and the peak strain values. So the peak impact force during a slamming event is considered to be the function of the entrance velocity. The change in the average peak strain values recorded with the three strain gauges in the drop tests for the three test objects with respect to the entrance velocity is shown in Figure 6.12. The peak strain values for all strain gauges in the hydrophobic cases are always smaller than the ones with the untreated surfaces. This figure clearly shows that the difference of the peak values for the hydrophobic and untreated cases is increasing as the entrance velocity increases. This tendency is present in all experiments that were carried out. For each entrance velocity, at least seven slamming tests were performed to see the reproducibility of the difference in magnitude of the peak strain values the hydrophobicity causes. The standard deviation of the experiments can be seen in Figure 6.12 in terms of the error bars. For the case of the spherical test object, comparably rigid, the peak strain value follows a second order relationship and increases quadratically with the entrance velocity. However, for the cylinders, where more deformability is present, the relation between the peak strain values and the entry velocities follow a more linear relationship. This means that the impact loads acting on the sphere rise faster with increasing entrance velocity.

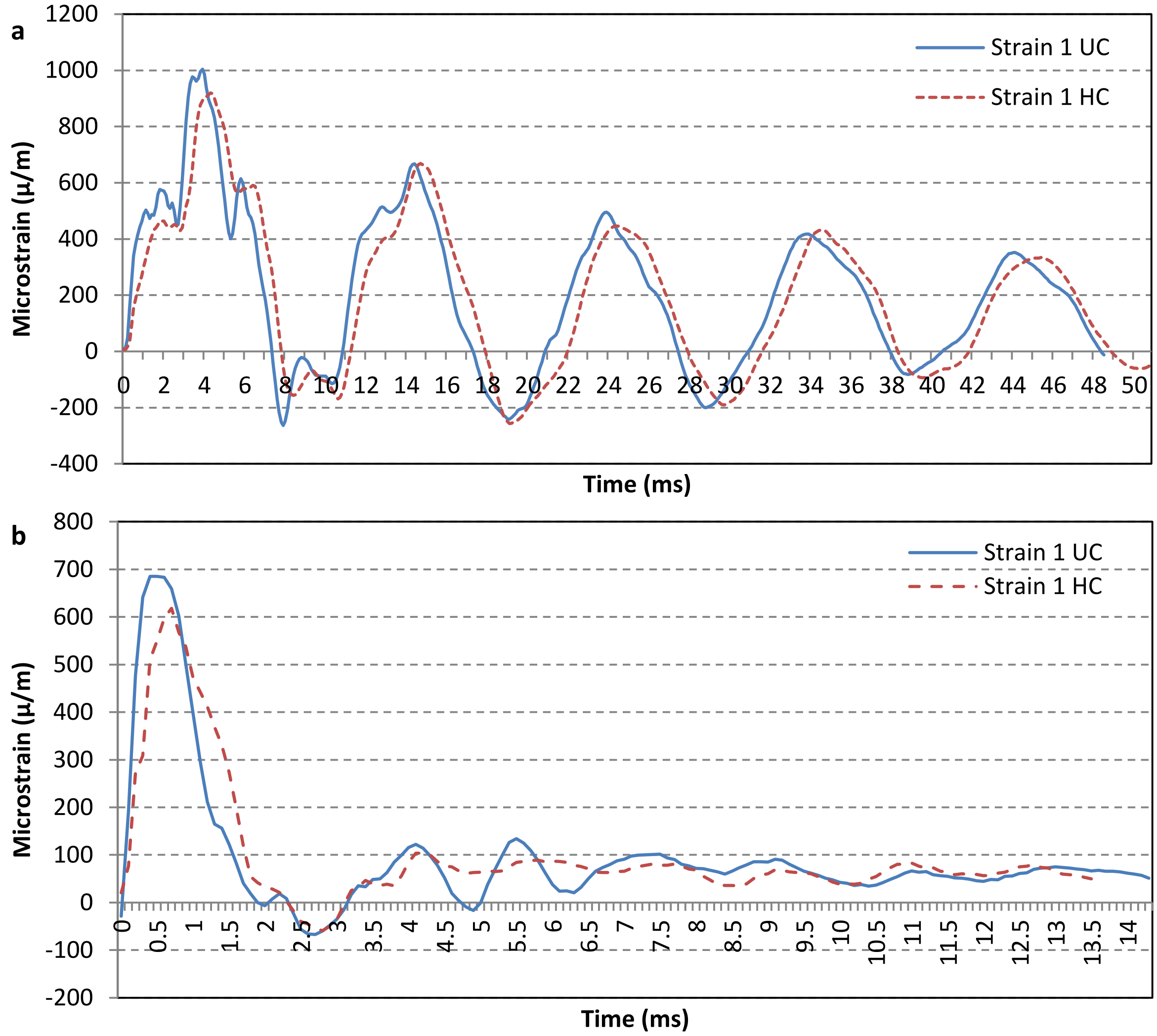

Figure 6.10 Time plots for the bottom strain gauge (0° deadrise angle) installed on (a) UPVC cylinder (C1) (b) Sphere (S1) c) Aluminum cylinder (C2) for a drop height of 100 cm and an entry velocity of 4.36 m/s.

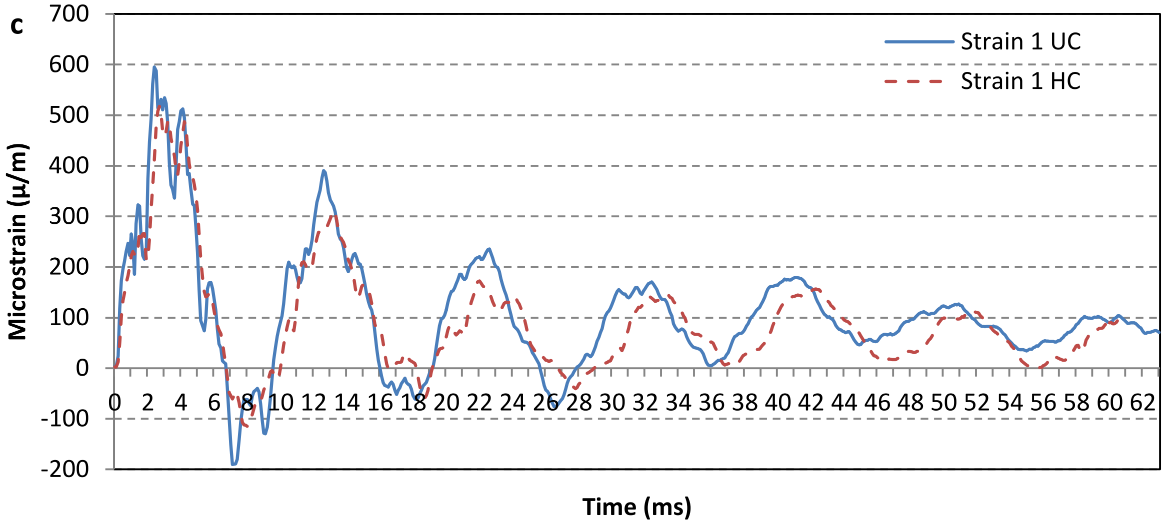

Figure 6.10 Time plots for the bottom strain gauge (0° deadrise angle) installed on (a) UPVC cylinder (C1) (b) Sphere (S1) c) Aluminum cylinder (C2) for a drop height of 100 cm and an entry velocity of 4.36 m/s (cont.).

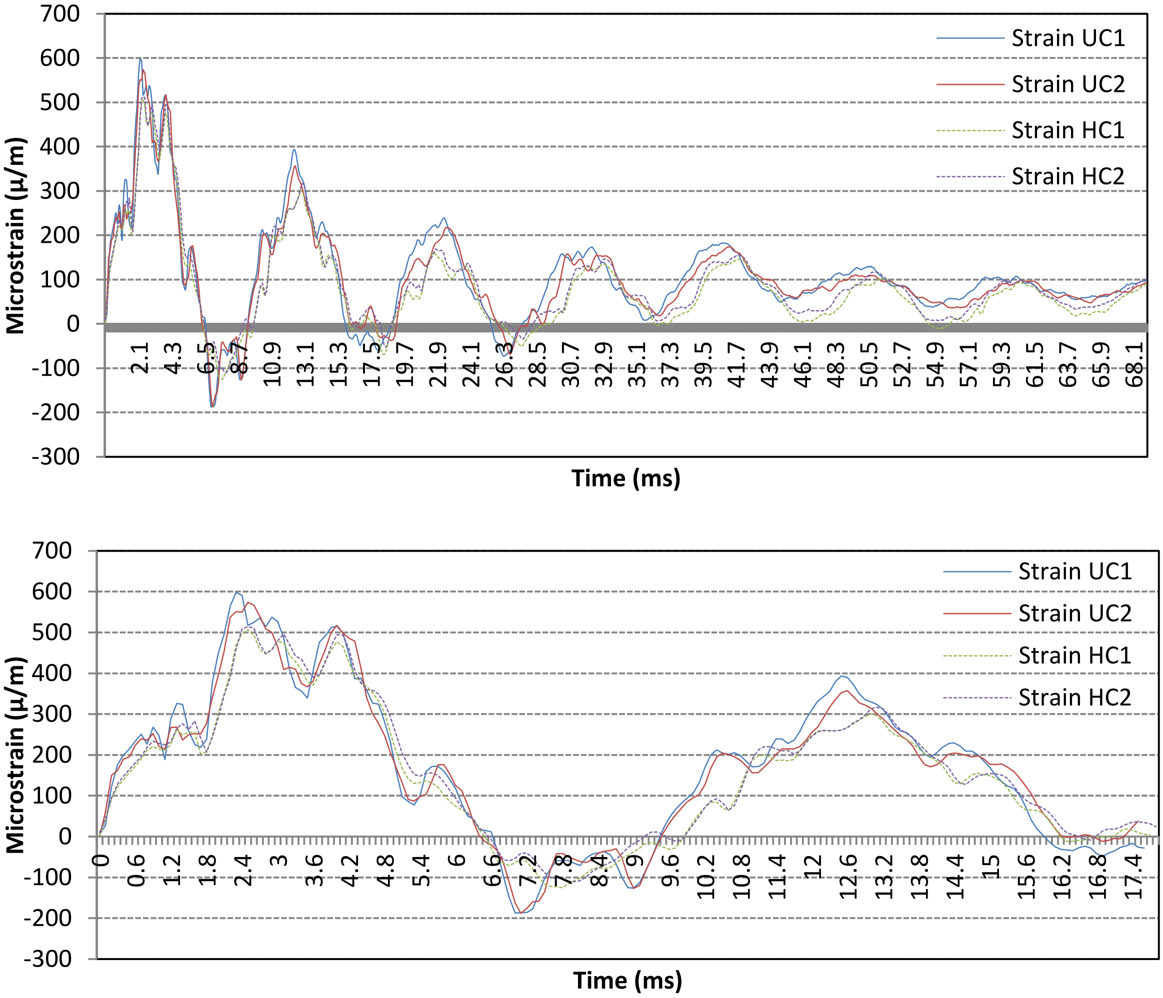

Figure 6.11 Repeatability of the impact tests of the Aluminum cylinder with both surfaces. Strain 1 values of the impact tests from 100 cm.

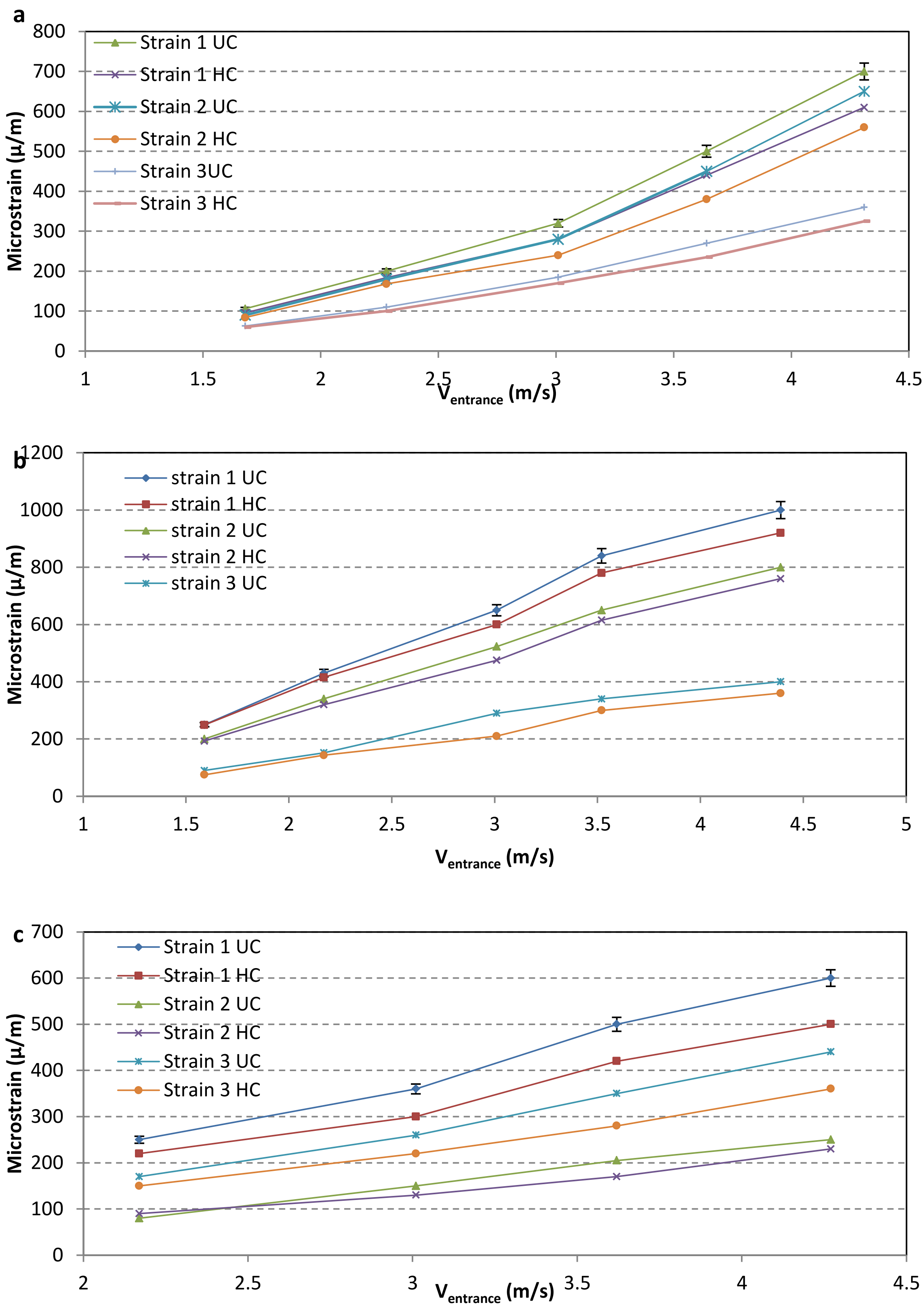

Figure 6.12 Peak strain values for strain1 (θ = 0°), strain2 (θ = 10°) and strain 3 (θ = 30°) as a function of the entrance velocity for (a) Sphere (S1) (b) UPVC cylinder (C1) and (c) Aluminum cylinder (C2)

In Figure 6.12 each data point illustrates the averaged peak strain values for seven consecutive slamming tests under the same test conditions. The scatter of these test results for each point is not large and represented with the error bars shown on the data points of the first strain values. The differences between the hydrophobic case and the untreated case are much bigger than the scatter level of these strain results. Before each recordings, it is important to wait for the wakes die out in the water tank and vibration is not present on the frame of the setup for the reproducibility and the correctness of the strain measurement results.

Since the impact forces could not be determined due to the lack of the necessary information of the elasticity modulus of the materials, the slamming coefficient (the non-dimensional impact force) of the impacts cannot be directly determined. But taking the peak strain value normalized by the square of the entrance velocity as resemblance to the slamming coefficient, it is possible to get the behavior of the slamming coefficient under the hydrophobic surface effects. The normalized peak strain values are plotted as a function of the entrance velocity in Figure 6.13. The characteristics of the curves in Figure 6.13 would be the same of the slamming coefficient curves. In all experiments for the three test objects, the normalized strain values with the hydrophobic surface are always smaller than the one with the untreated surface for the same entrance velocity. It can also be observed that for the case of the rigid sphere, the normalized strain values do not change as much with the entrance velocity. Comparing with the experimental results from the literature, it can be concluded that the slamming coefficient in slamming for rigid bodies is independent from the entrance velocity and it is the same for the slamming events with the hydrophobic surfaces as well. Whereas, the slamming coefficient for the deformable cylinders decreases with increasing entrance velocity. The same result can be observed in Figure 6.13 that the relation between the strain values and the entrance velocity for the deformable cylindrical test objects is almost linear.

In order to convert the strain measurements to impact forces to be used in calculation the slamming coefficient, Cs, static compression tests were done on each test objects. These tests were performed via seven different weights varying from 1 kg to 50 kg. 10 mm wide and 20 mm thick an aluminum bar was placed on the test objects. The length of the bar was chosen to be the same length as the test objects. The test objects then were placed on the concrete floor. To compress the test objects, the designated weights were placed on the aluminum bar one by one. The applied forces (weights) and the corresponding strains at the locations of the strain gauges were measured in order to obtain a linear relation between strain and force. Then these linear relations obtained for each strain gauge were used to convert the strain values recorded during the slamming tests to impact forces acting vertically on the test objects. While doing so, the same strain gauges were kept on the test objects, during the slamming tests and the compression tests. Eventually, the slamming coefficients were calculated from the impact force values and plotted as a function of entrance velocity in Figure 6.14. The force versus strain relation that is used to convert the measured strains to slamming forces is not trustworthy. But it is good enough for making the comparison of the slamming coefficients between the cases of hydrophobic and untreated surfaces. The slamming coefficients calculated with this method for the test objects are smaller than the ones for rigid bodies in the literature. To show the effect of rigidness a thicker aluminum cylinder with an average wall thickness of 0.6 cm was tested (ridged aluminum). It gave higher Cs values as seen in Figure 6.14.

The slamming coefficient (dimensionless impact force) is given by:

$$C_s = \frac{F_l}{\rho R L {V_{entry}}^2} \tag{6.5}$$

for a cylinder and

$$C_s = \frac{F}{\frac{1}{2}\rho {V_{entry}}^2 A_x} \tag{6.6}$$

for a sphere.

In Figure 6.14 Von Karman’s and Wagner’s approaches are shown as the limits of the impact forces predicted on rigid bodies, Cs=π and 2π, respectively. For the initial stage of the impact, the hydrodynamic force (per unit length) can be approximated by (Abrate [7])

$$\mathrm{F} \approx \pi\rho {V_0}^2 (R - V_0 t) \tag{6.7}$$

Eqn. 6.7 is obtained from Von Karman’s approach, giving the same max. impact force as Von Karman’s as seen in Figure 6.14.

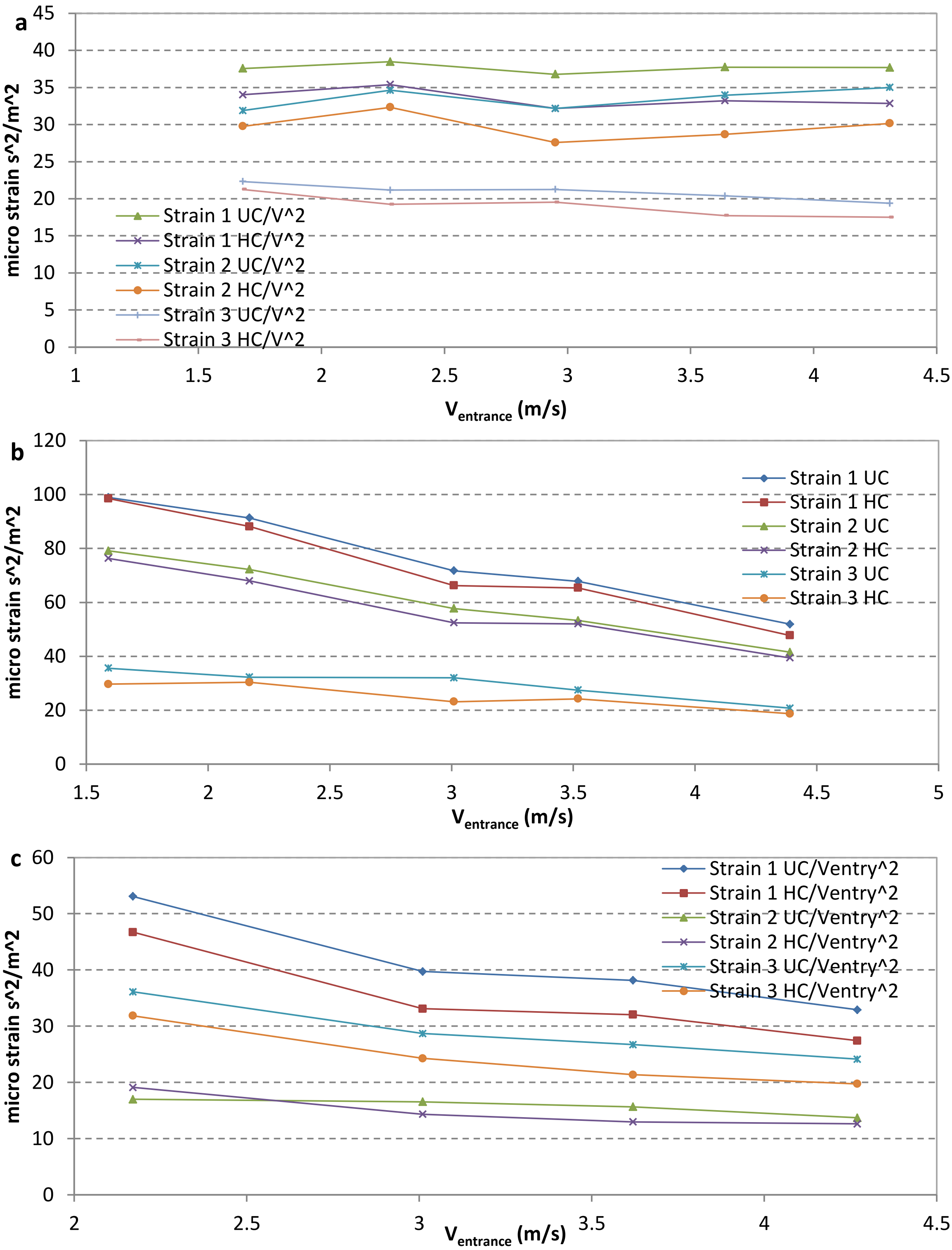

Figure 6.13 Normalized peak strain values as function of entrance velocity for (a) Sphere (S1) (b) UPVC cylinder (C1) (c) Aluminum cylinder (C2)

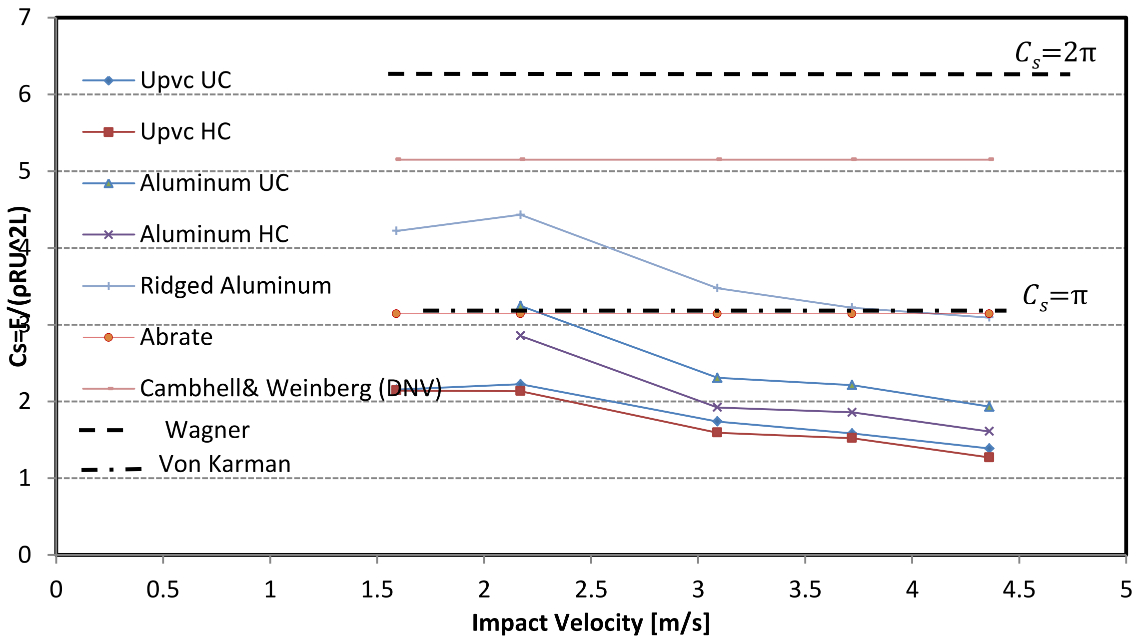

Figure 6.14 Maximum slamming coefficients for cylindrical test objects as a function of entrance velocity

The wetted area and the force (Figure 6.10) grow gradually as the object penetrates water. It can be observed from the Figure 6.10 that the strain value (force) reaches its maximum at a certain moment. It reaches its maximum in 3.7 ms for the UPVC cylinder, and in 2.3 ms for the aluminum cylinder in untreated case. Under the hydrophobic effects, they become 4.3 ms and 2.5 ms respectively. It is possible to calculate the distance that the cylinders travel during this time, knowing that the velocity of the object does not change at the initial stage of the impact. And from this distance, the submergence angle can be calculated with an uncertainty of ±1°. During the experiments of the UPVC and the aluminum cylinders dropped from 100 cm with the untreated surface, the maximum strain value was measured at the values corresponding to a submergence angle of 31° and 33°, respectively, of the cylindrical circumference from the vertical. Figure 6.15 illustrates an average wetted area that corresponds to the maximum strain value for the cylindrical test objects. And this angle, where the maximum impact force occurs gets smaller for smaller entrance velocities (i.e. 23° for 30 cm drop height). It is worth to mention that rising time of the strain value to its maximum is measured to be independent of the entrance velocity in this study. Moreover, the submergence angle, and the corresponding penetration depth, is larger under the hydrophobic effects for the same test conditions. It is measured to be 33.5° and 35° for the UPVC and aluminum cylinders respectively. Having larger penetration depth, and thus larger wetted area (Figure 6.15), and smaller strain values (Figure 6.12) under hydrophobic effects, two main conclusions can be made;

The impact pressure is distributed on a wider surface area at the beginning of the impact and

The impact pressure on the body is smaller in slamming with hydrophobic surfaces.

When considering the splash velocities is higher in the hydrophobic case, larger amount of water is pushed away from the object, causing a larger wetted area. This is because more kinetic energy is transferred to the water.

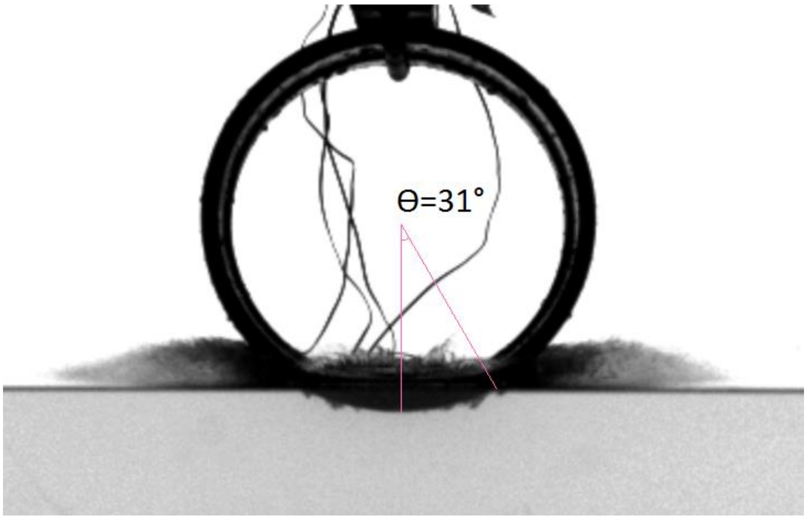

Figure 6.15 High speed camera images at the time frame corresponding the maximum impact force during a slamming event with the UPVC cylinder (C1) for a drop height of 100 cm

6.1 Discussion

In early 20th century two approximate solutions were developed by Von Karman [5] and Wagner [6], based on the momentum theory for the problem of the water entry of the solid objects. Their solution is used to predict the slamming (a.k.a impact or hydrodynamic) force and the pressure distribution on the wetted surface of an object entering water. When the whole motion is taken into consideration, as an object impinges on the free surface, first the object sprays water into the air and then a jet flow is generated along the surface of the object. When the object moves further downward, a large amount of water is pushed outward and piles up at the root of the jet. The water pile up is taken into account in Wagner’s approach, but there is a singularity in his solution where the jet is formed. Here there are some questions arise; is it possible to lower the magnitude of the impact loads or to change the propagation characteristics of the impact pressure or to widen the distribution of the impact pressure by altering the properties of the surface? The flexibility of the body is already studied by many researchers, and its effect in reducing the impact pressure is proven experimentally and numerically.

Within the experimental conditions of this study, when comparing the results obtained from the hydrophobic coated test objects with the ones from the untreated test objects, it was observed that in the first case the strain values measured at the bottom of the test objects were decreased at the impact stage of the slamming event, and the amount of water riseup and the velocity of jet flows were increased. Although there is not any difference in slamming test conditions, changing only the surface characteristics caused such a different phenomenon. The main outcome from the comparison of these two cases is that more kinetic energy is transferred to the water during the impact. As a result, the magnitude of the impact force gets smaller under the hydrophobic surface effects. Then it is necessary to check if the velocity of the body, after the impact, slows down due to the loss of more kinetic energy. It is known from the literature that the change in velocity of the objects during the impact is very small in the time span of the pressure pulses. But it is still needed to investigate whether the hydrophobicity has any effect on the velocity of the object due to the loss of its kinetic energy. It can be observed from the object tracking in the high speed camera images that the velocity of the object does not seem to lose its velocity. Two reasons are encountered for the explanation. First, the weight of the objects with the carriage is such large (12-14 kgs) that the effect of the hydrophobicity cannot be detected on the velocity of the objects because the total kinetic energy due to the total mass is quite large and the objects are still accelerating after the impact in the water. The difference in the amount of kinetic energy between the cases is very small comparing to the total kinetic energy. Secondly, for smaller drop heights the impact force is quite small that the object keeps accelerating after the impact. The change in the kinetic energy is comparably large enough in the scale of the energy hold by the water pushed away in jets (splash velocities), but not detectable in the scale that the test object poses. Remembering the force balance on an object entering the water, as a remedy to this problem, the balance between the inertia force, buoyancy force, drag force, capillary force, and the impact force should be adjusted such a way that the inertia force is not dominant anymore and the impact force is still large enough for comparison. Thus, its possible decay can be detected in terms of the loss kinetic energy. For this reason, it is decided that the spherical test object would be dropped without the carriage, with lesser total weight of 630 grams, for minimizing the inertia force (and the kinetic energy). It can be seen from the amount of the splashed water in the Figure 6.16 that the transferred kinetic energy is much larger in the hydrophobic case. The test object does not submerge totally due to positive buoyancy and it stops at a certain depth depending on the drop height. 15, 50 and 65 cm drop heights were tested. It can be concluded that the object with hydrophobic surface slows down faster and penetrates lesser into the water than the one with untreated surface. On average, the penetration depth with the hydrophobic surface is 3% smaller than with the untreated one.[1]

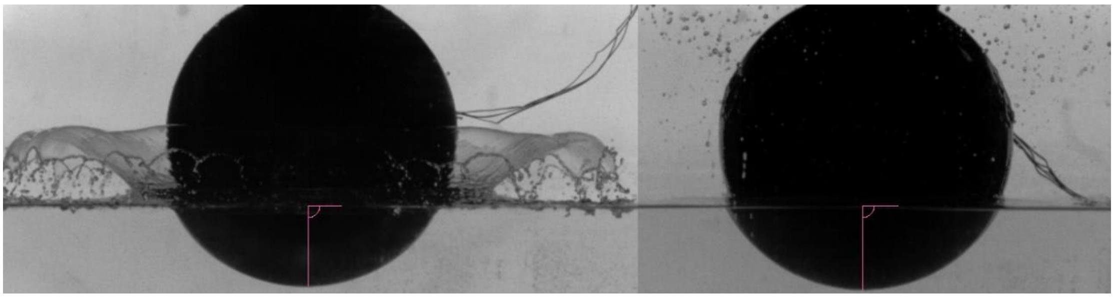

Figure 6.16 Snapshots taken corresponding to the stop point of the water entry of sphere (S1) without carriage dropped from 0.15 m a) Hydrophobic case b) Untreated case

[1] This chapter was published in Ocean Engineering Volume 129, 1 January 2017, Pages 240–252.

CHAPTER 7

THE EFFECT OF DIFFERENT HYDRODYNAMIC PARAMETERS IN WATER ENTRY OF THE OBJECTS WITH CONSTANT DEADRISE ANGLE

In this chapter, the results of experimental investigation of the slamming of the wedge and cone shape sections during water entry are presented. The effect of contact angle was examined by using various deadrise angle sections and compared with one another. The strain gauges were implemented in each section and positioned with same distance from the tip, for all objects. The high speed camera was employed to capture the process of penetration of the objects and utilized for calculation of the pile up coefficient, jet flow velocity and wetting factor. The change of surface parameters was studied and each test was also performed by increasing the water and surface contact angle via the hydrophobic coat. These comparative results showed that with the hydrophobic coat more energy was transferred to the water at the same instant and in turn, the hydrodynamic effect was reduced.

7.1 Analytical Formulation

The momentum theory applied to compare the experimental results with ignoring the viscosity, surface tension, gravity and drag effect and so Newton's second law, the force of hydrodynamics is:

$$M\ddot{\zeta} = -F \tag{7.1}$$

where F is the hydrodynamic force and thus impact force, M is the mass of the object, g is the gravity and ζ is the penetration depth.

The calculation of the impact force for wedge and cone shapes as follow;

The impact force on the wedge shape body is:

$$F = -M\ddot{\zeta} = -M\left(-\frac{\dot{\xi}^3}{MV_0}\frac{dm}{d\xi}\right) = \frac{\pi\rho\gamma^2}{tan^2\beta}{V_0}^3 t \tag{7.2}$$

where $V_0$is the entry velocity and t is the time of the object water entry process

Calculation of the relative water splash up γ changes with some approaches for Von Karman γ=1 and Wagner γ=π/2 and some other predictions depend on the deadrise angle (Mei [31], Payne [88]).

The force on a cone shape with deadrise angle β is determined from;

$$F = 2\pi\rho {V_0}^4 t^2 tan^3\beta \tag{7.3}$$

7.2 Experimental Results and discussion

The wedge and cone drop experiments are presented in this section. The angles of 30° and 45° for the wedge and 7.5°, 30° and 45° for the cone have been selected to measure the slamming impact. Visual study was made for 60° smooth and ridged wedges and comparison was performed for the hydrophobic case for all experiments. The images of the 60° wedge entry is demonstrated in figure 7.1 with different surface roughness, and the image process was studied to introduce the effect of the hydrophobicity. The pileup and wetting factors were configured to show differences which are important at the energy transfer approaches.

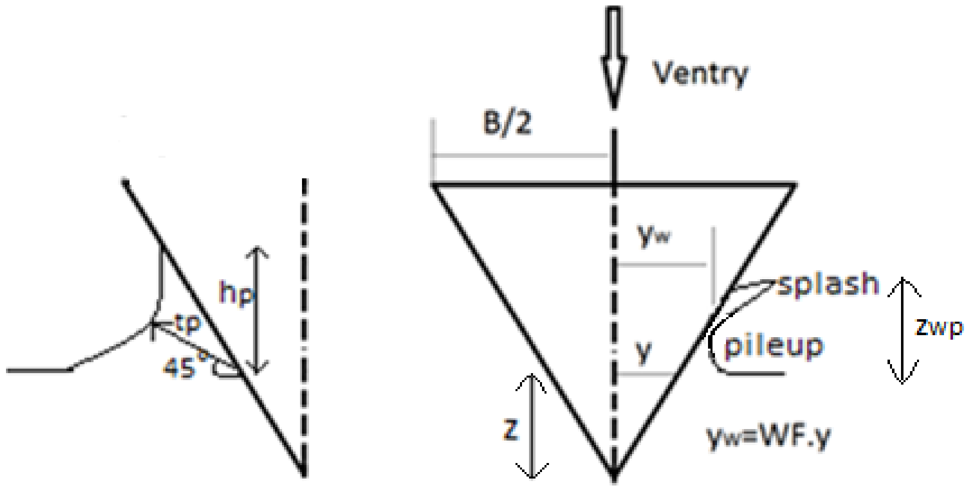

Figure 7.1 Sketches of wedge water entry with demonstration of pileup and splash

The pileup C_{pw} and wetting factor WF are identified below by taking data from the images at four different entry velocities of the wedges. Furthermore, the wedges which have different roughness factor are also shown.

Calculation of the pileup coefficient was evaluated by multiplying the thickness and height of the pileup water then dividing by multiplication of the wetted-length and entry depth. The constant 45° angle was used for measuring the thickness. The results show how much water is repelled at the same entry velocity and for different surface properties.

$$C_{pw} = \frac{h * t_p}{y * z} \tag{7.4}$$

where C_{pw} is the pileup coefficient, h is the height of pileup and t_p is the thickness. The y and z express the wetted length and entry depth of the wedge, respectively.

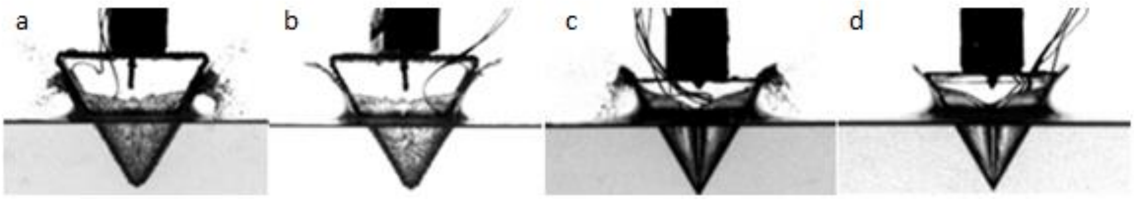

Figure 7.2 The snapshot of wedge water entry a) ridged wedge b) ridged wedge with hydrophobic coat c) smooth wedge and d) smooth wedge with hydrophobic coat

Figure 7.2 shows photos for the ridged wedge and smooth wedge at the instant of the water entry process. The a and c photos are samples of the hydrophobic surface and the remaining photos are wedge drop tests which have an untreated surface. It is clearly observed that the attachment of water is less for the untreated surface and also the splashes reach higher in the hydrophobic cases.

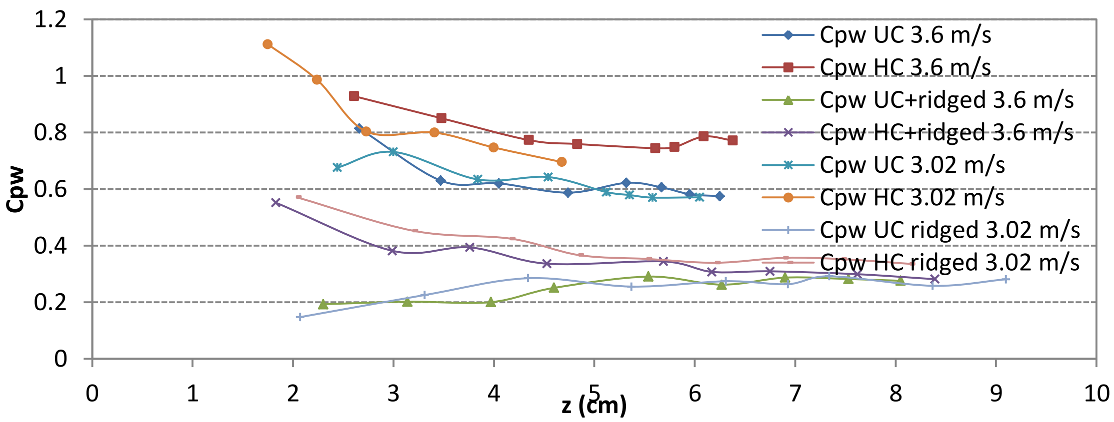

Figure 7.3 Pileup coefficient for ridged wedge and smooth wedge with hydrophobic surface

Figure 7.3 shows the pileup coefficient (C_{pw}) versus entry depth of wedge which has constant 3.6 m/s and 3.02 m/s entry velocities for ridged wedge and smooth wedge hydrophobic cases. The pileup coefficient is about 0.8 for smooth wedge hydrophobic cases, 0.6 for smooth wedge untreated cases, 0.4 for ridged wedge hydrophobic cases and 0.3 for ridged wedge untreated cases. The results show that the pileup coefficient is much bigger for the hydrophobic coated series at the same water entry velocity. The wedges ratio of ridged surface values are also different as discussed before, the roughness factor changes the effect of the wettability of surface. The coefficients are independent of the entry velocity and depend on the surface parameters.

The rising water level against the free surface level is significant in predicting the energy transfer to the water. The so-called wetting factor WF can be determined in the wedge impact problem as a ratio of the half wetted width y_w wedge to the half width wedge at the free surface level y.

$$WF = \frac{y_w}{y} \tag{7.5}$$

In all literature, the Wagner approach gives the wetting factor as a constant $\pi/2$ value for all deadrise angles. Cointe [89] and Zhao and Faltinsen [90] also accepted these wetting factor values. W. S. Vorus [91] revealed a new approach for the wetting factor:

$$WF = \frac{\pi}{2} * \frac{\sqrt{\pi}}{b * \Gamma(\lambda) * \Gamma\left(\frac{3}{2} - \lambda\right) * cos\tilde{\beta}}, with\ \lambda = \frac{1}{2} - \frac{\tilde{\beta}}{\pi}, and\ \tilde{\beta} = tan^{-1}(sin\beta) \tag{7.6}$$

where β is the deadrise angle and b is the jet head offset

W. S. Vorus [91] indicated that $\pi/2$ can be the upper limit for wedge case, and for the 60° deadrise angle, the value is 1.18.

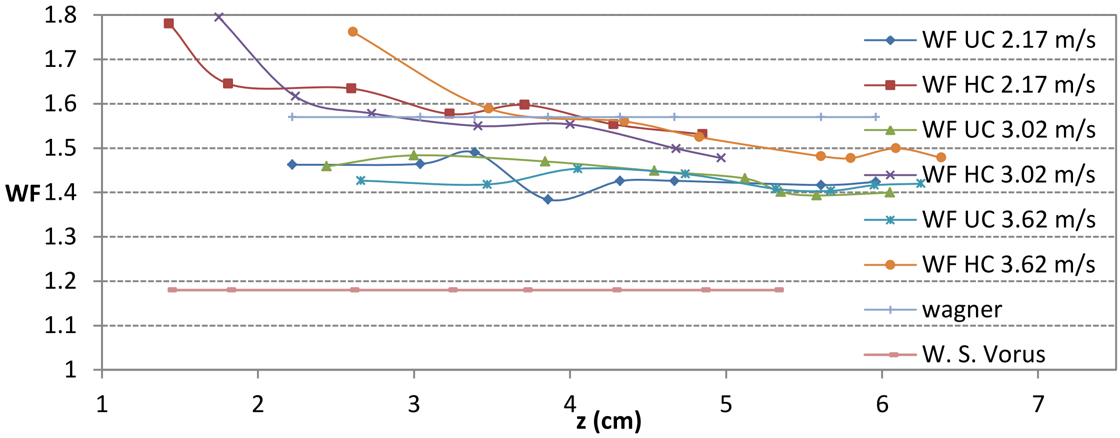

Figure 7.4 The wetting factor of smooth wedge for constant 60° deadrise angle with hydrophobic surface

In figure 7.4, the wetting factor is illustrated versus the depth of wedge for a 60° smooth wedge and three drop heights(30 cm, 50 cm and 75 cm). The hydrophobic cases are observed to have a higher value than the untreated cases for each with the same entry velocity. In the initial stages of the water entry process, the wetting factor approaches 1.8 then goes down to 1.5 in the hydrophobic coated drop test. However, the coefficient is constant and approximately equal to 1.4 in every entry velocity and depth for the untreated cases. In these cases, the wetting factor does not change with entry velocity. The Wagner [6] solution, especially, is close to the hydrophobic cases for small entry but W. S. Vorus [91] result remains at low values.

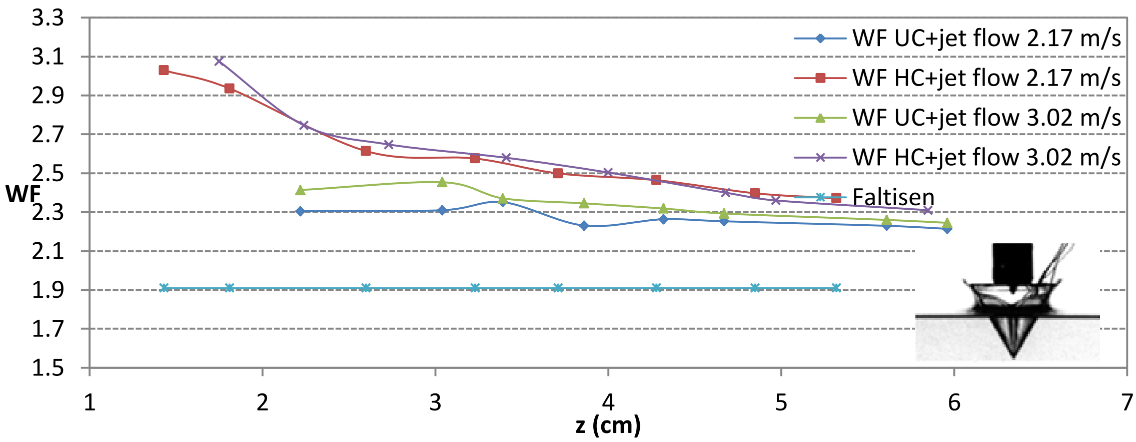

Figure 7.5 The wetting factor of wedge for constant 60° deadrise angle by taking into account jet flow with hydrophobic surface

The value of the wetting factor is relatively constant for the untreated smooth wedge and two drop heights; however, the result shows that a downward tendency occurs for the hydrophobic cases. Hydrophobic coating makes the wetting factor reach a higher value than for untreated ones. Though the tendency does not change significantly, contribution of the jet flow can be concluded by the increasing wetting factor value. Zhao, R and Faltinsen [90] compute the wetting factor by $\frac{4}{\pi}$ $(1 + cos\beta)$. The Zhao, R and Faltinsen [90] formulations show the results are 18% lower than the experiments, on average. Although the wedges and cones, which have smaller deadrise angles, can be visualized, determination of the wetting factor is difficult because of the complexity of the intersection point (figure 7.5).

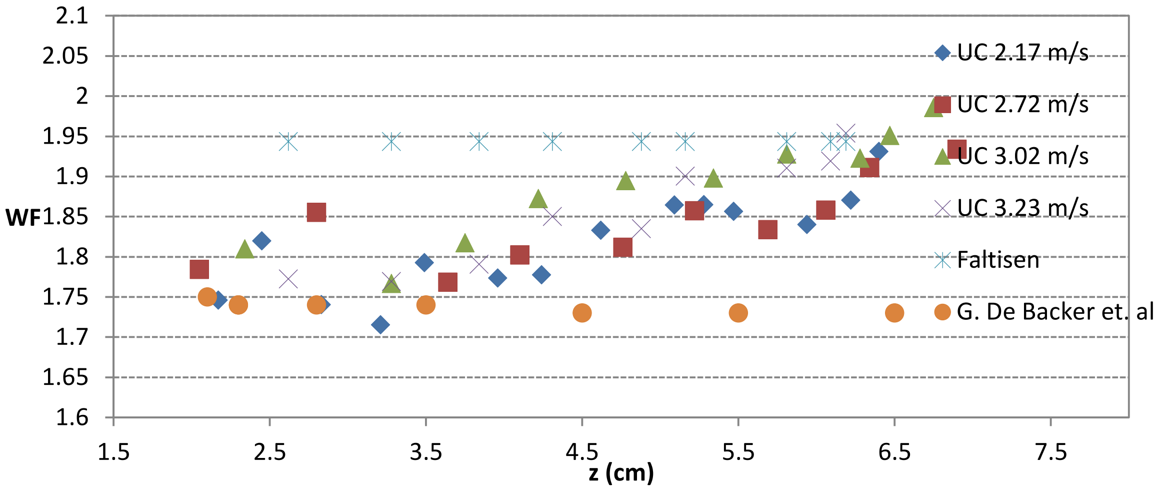

Figure 7.6 The wetting factor of cone water entry with 45° deadrise angle

The wetting factor (WF) as a function of cone entry depth is also calculated for the cone shape with 45° deadrise angle and is illustrated in figure 7.6. The WF is determined by taking into account the wetting radius at undistributed level (y) and distributed level (y_w) then splash height (z_{wp}) and penetration depth (z):

$$WF = \frac{y_w}{y} + \frac{z_{wp}}{z} \tag{7.7}$$

where z_{wp} is the height of the jet flow.

G De. Backer et al. [22] added the jet flow height because the intersection point occurs above the pileup height. When applying various drop heights, the results show that free fall from different heights does not change the wetting factor: small scatter is observed between 1.75 and 1.97. The analytical approaches of Zhao, R and Faltinsen [90] and the experimental study of G. De. Backer et al. [22] for the wetting factor are positioned at the edge of the upper and lower levels, respectively of our results.

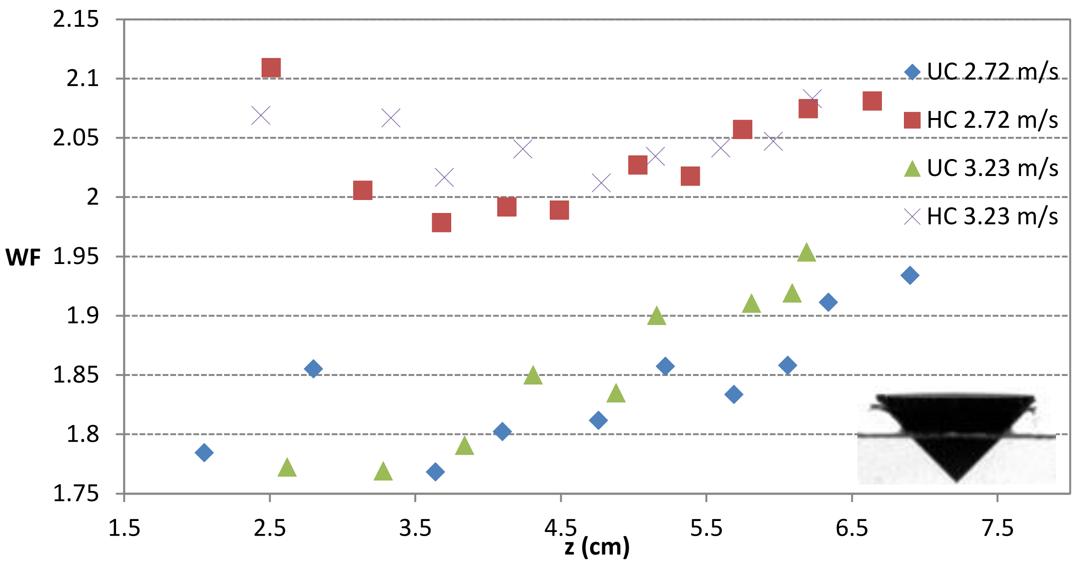

Figure 7.7 The wetting factor of cone water entry for 45° deadrise angle with hydrophobic surface

The hydrophobicity effect is illustrated in figure 7.7 by wetting factor versus cone water entry depth at the same drop height. The wetting factor shows the repelling water ratio because the majority of the raised water width and wetted side width demonstrate that the raised water reached the maximum level at the same entry depth as the hydrophobic coated test.

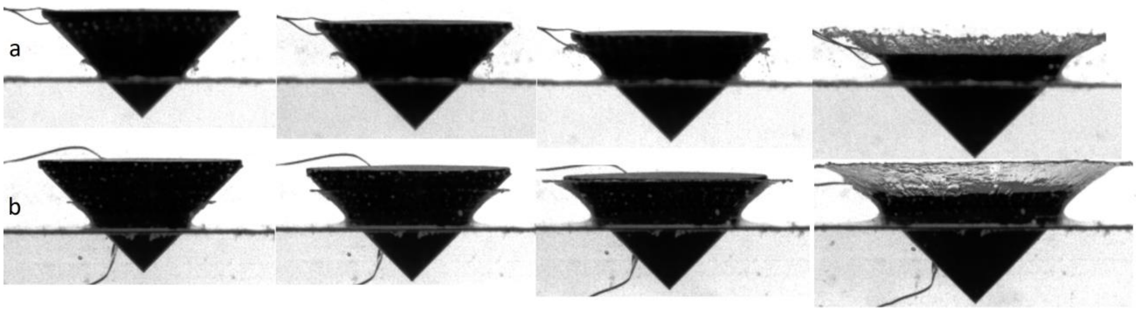

Figure 7.8 The penetration process of cone water entry from 30 cm drop height for a) untreated case and b) hydrophobic case

Figure 7.8 illustrates the penetration process of both (a) untreated and (b) hydrophobic coated drop tests from 30 cm. The snapshots clearly show that the water uprise reaches the upper position in the hydrophobic case for every process so more energy transfer to the water occurs.

7.3 Analysis of impact dynamics

The strain measurements are performed for wedges for two different deadrise angles and for cones for three different deadrise angles. It should be well-known that strain gauges are applied to the same distances from the tip of specimens for all cases. Each drop test was performed at least five times. All specimens have 2 mm thickness and were made with PLA (Polylactic Acid). Figure 7.9 and figure 7.10 show the measured maximum strain values as a function of entry velocity for both wedges and cones at various drop heights. Considering the strain values at the same deadrise angle, both the wedge and cone shapes have different values. This shows that the impact force disperses for the cone shape so low strain values are measured. The effect of the deadrise angle can be observed showing that the small deadrise angle specimens are affected more by the impact. Furthermore, the slamming induced strain is increased by rising entry velocity, as expected.

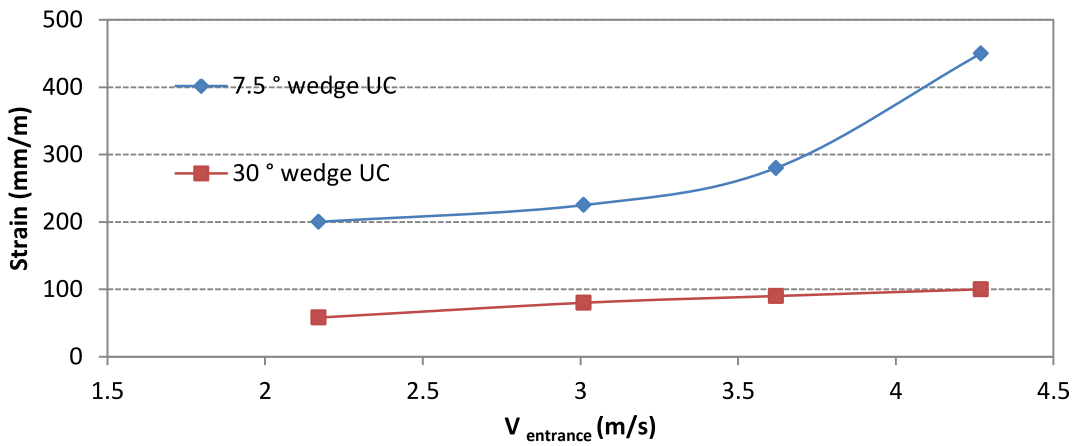

Figure 7.9 The strain values of different drop heights for wedges of 7.5° and 30° deadrise angle

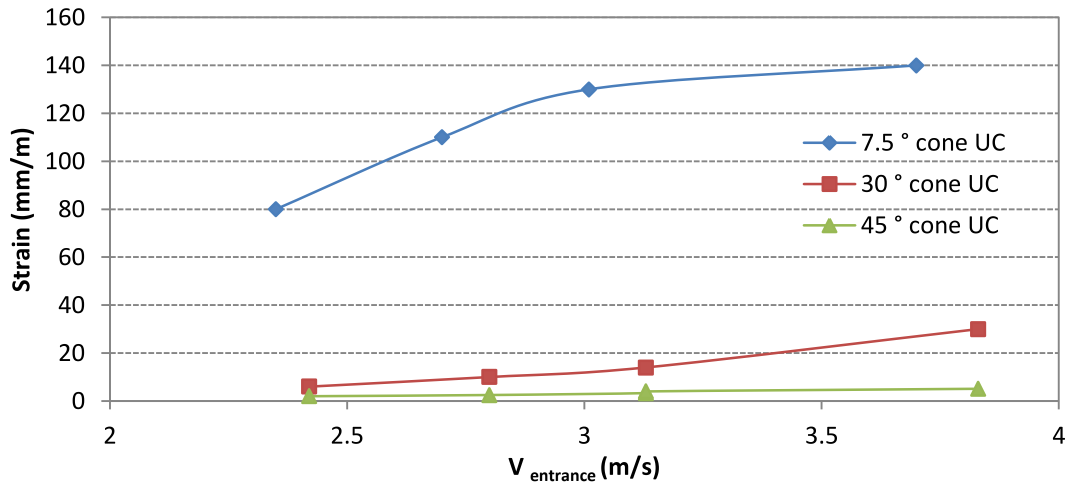

Figure 7.10 The strain values of different drop heights for cone of 7.5°, 30° and 45° deadrise angle

Van Nuffel [65] is used in both strain gauges and force transducers in order to verify the slamming force values. The compression test was performed to convert the strain value to force by attaching strain gauges to the place where the forces were applied. The force-strain relations were revealed by applying various forces and recording the responses of the strain gauges. Van Nuffel [65] also stated that the quasi static compression test was also applicable for converting slamming strain to slamming force. Strain-force conservation was also made in the current experiments by measuring the strain on the wedge by applying known forces.

The test series were performed for determining the force-strain relations. Figure 7.11 shows one of the samples of the relations from the test measuring the impact forces. It can be observed that the linear intersection for the cone with 30° deadrise angle was obtained as the strain-force value in this case. The $y = 709350 * x - 25.872$ equation was released by spline fitting. The equation was used to calculate the slamming force from the measured strain in the experiments. The force-strain was determined for all wedges and cones, separately.

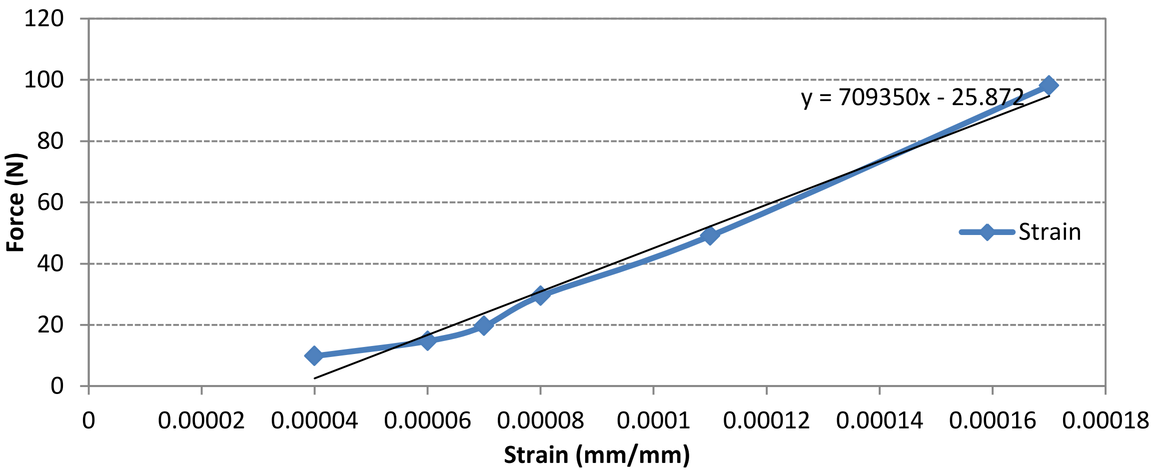

Figure 7.11 The strain values versus force by calibration of known forces

The measured strain values were converted to force by force-strain correlation and compared with the theories. One of the prediction forces which is used vertically on the specimen, is the added mass definition and conservation of momentum theory.

Comparison of the peak force coefficient value as a function of the deadrise angle is demonstrated in figure 7.12. The force coefficient for the wedge is expressed as (X. Mei [31]):

$$C_s = \frac{F\ tan\beta^2}{\rho {V_0}^3 t} \tag{7.8}$$

and the force coefficient for the cone is given by (Battistion and Iafrati [18]);

$$C_s = \frac{F\ tan\beta^3}{\rho {V_0}^4 t^2} \tag{7.9}$$

where t is time for reaching the maximum measurements values

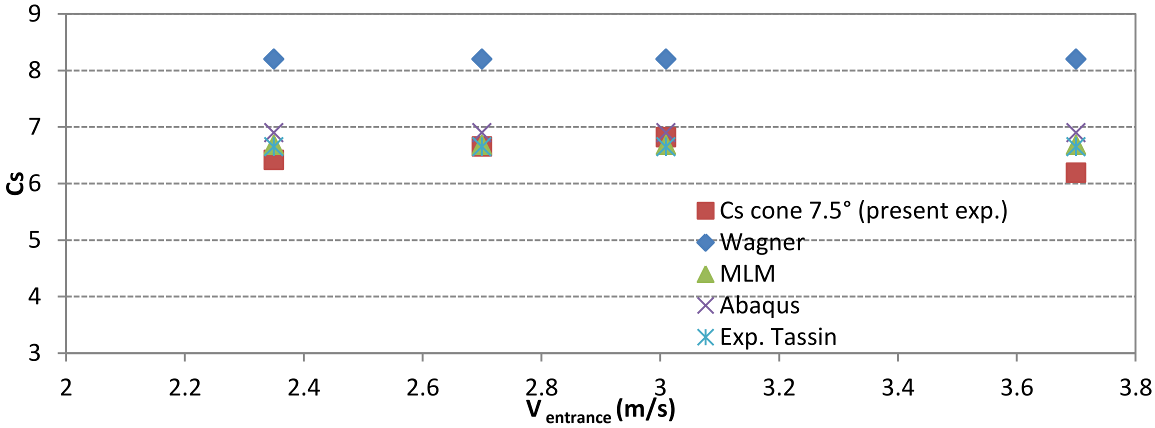

Figure 7.12 The slamming coefficient (Cs) of cone with 7.5 deadrise angle versus entry velocity

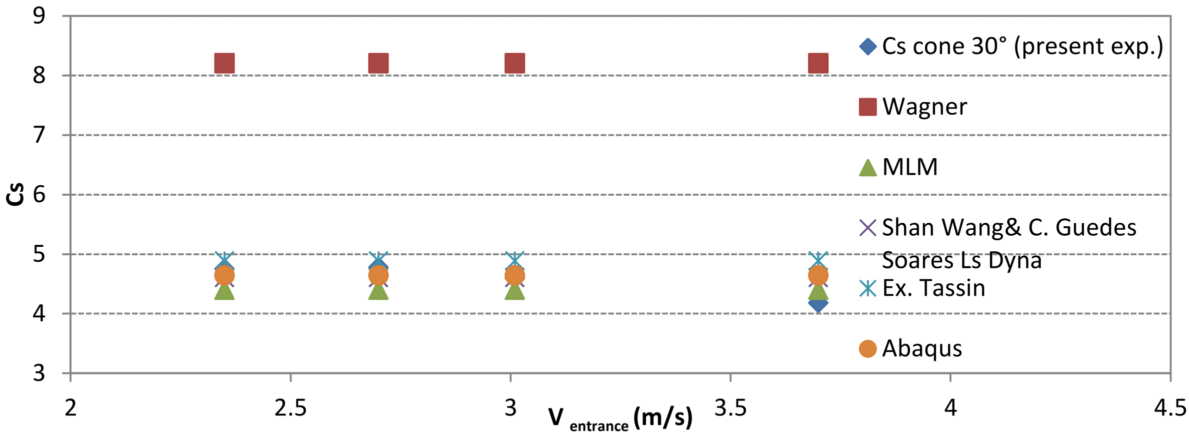

Figure 7.13 The slamming coefficient (Cs) of cone with 30° deadrise angle versus entry velocity

Figures 7.12 and 7.13 show the non-dimensional slamming force coefficient for cones with 7.5° and 30° deadrise angles versus water entry velocity. The results from the present experiments, agree well with those of abaqus (Shan Wang and C. Guedes Soares [45]), the experimental results from [92] and MLM (Modified Logvinovich mode) which was introduced by Korobkin and Malenica [93] but the Wagner solutions overestimate the coefficient when compared with other approaches. It can be observed that the most significant differences in the Wagner theory and in others occur with large deadrise angles.

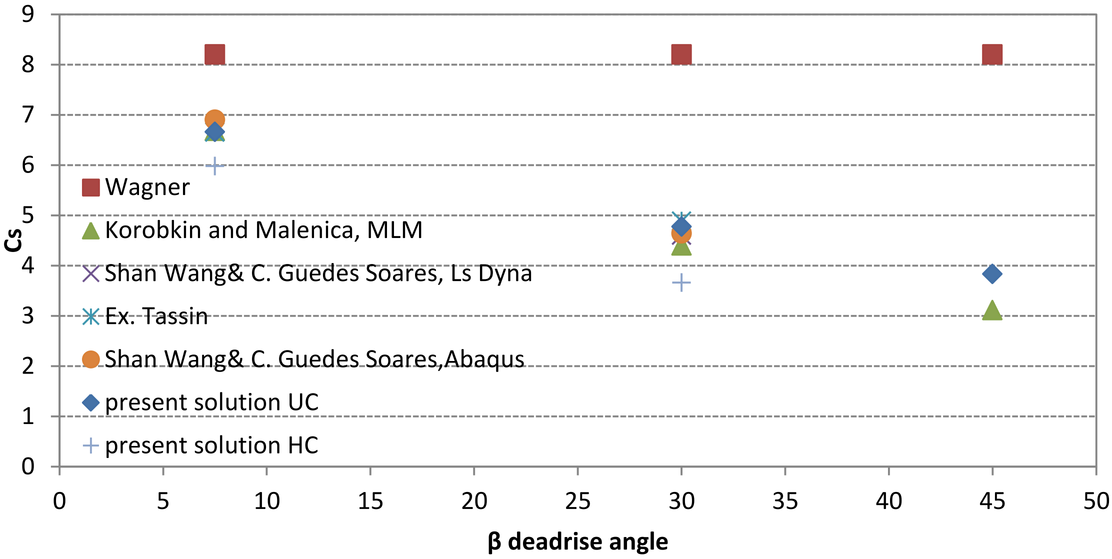

Figure 7.14 The slamming coefficient (Cs) of cone versus deadrise angle

Figure 7.14 presents the slamming force coefficient of the cone versus deadrise angle. The impact on the surface slightly decreases when the angle between cone structures and free surface of water because the area at the macro deadrise angle is affected less than the smaller ones in the same penetration positions. As expected, the slamming coefficient continues to decrease with growing deadrise angle. The numerical approaches and experimental coefficient values are close to one another except for Wagner’s theory. The Wagner theory is constant for various deadrise angles and works generally for small deadrise angles.

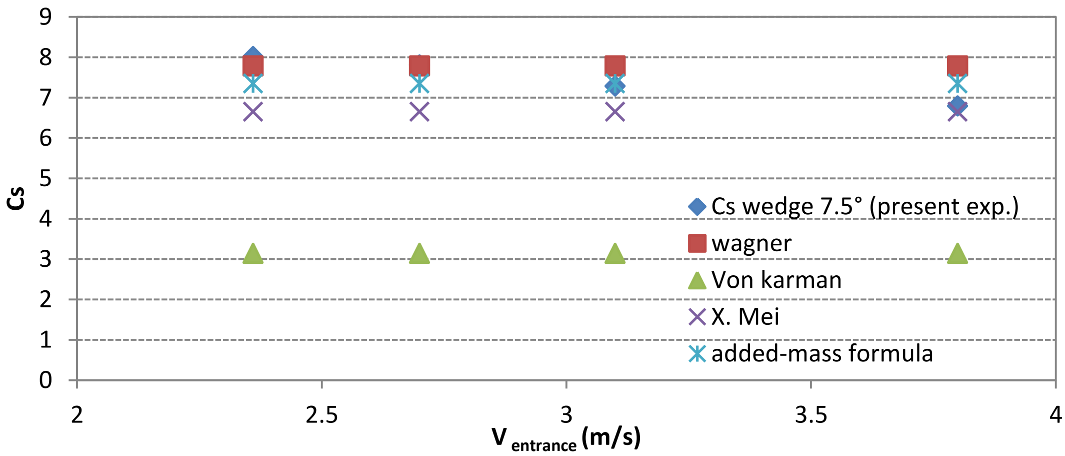

Figure 7.15 The slamming coefficient (Cs) of wedge with 7.5° deadrise angle versus entry velocity

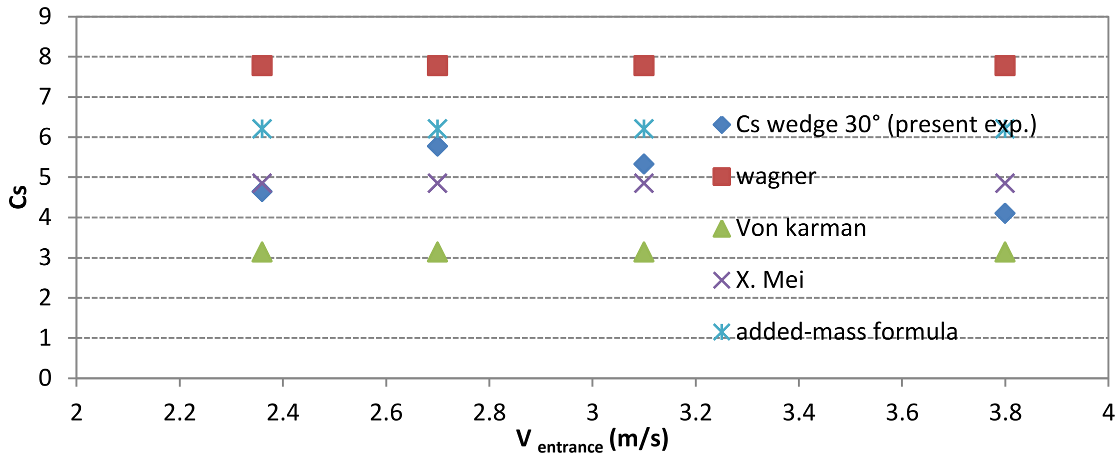

Figure 7.16 The slamming coefficient (Cs) of wedge with 30° deadrise angle versus entry velocity

The wedge drop test result for 7.5° and 30° angles is demonstrated as a non-dimensional coefficient versus water entry velocity in figures 7.15 and 7.16. The results presented have been compared to Von Karman [5], Wagner [6], and X. Mei. [31]. The Wagner and Von Karman theories remain at the upper and lower sides. Other theories are located within these two. There is little effect of velocity on the non-dimensional impact coefficient in the present calculations whilst the other approaches are constant for various water enter velocities.

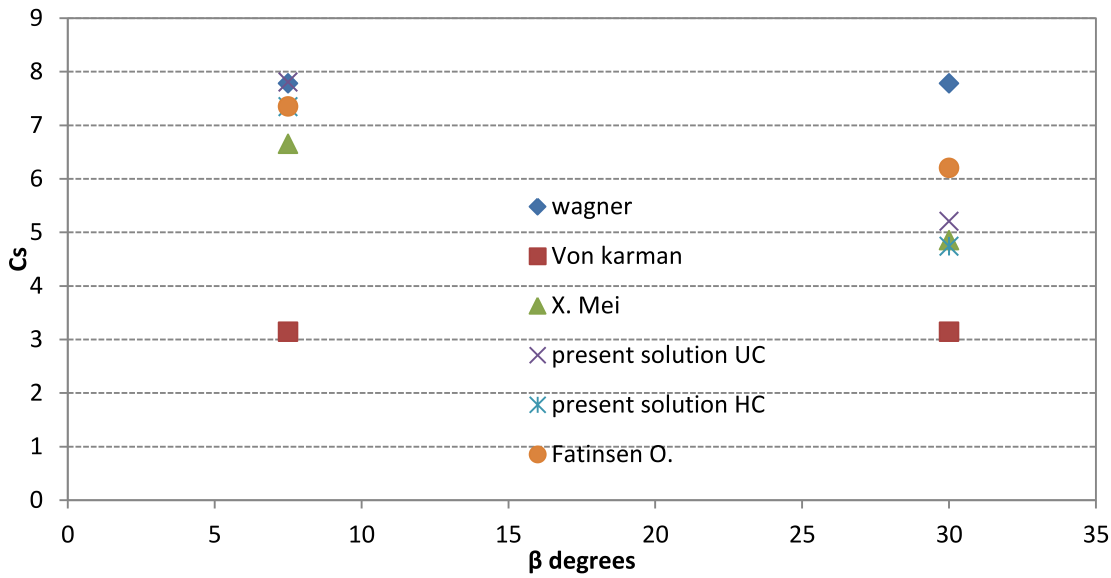

Figure 7.17 The slamming coefficient (Cs) of wedge versus deadrise angle

From figure 7.17 our experimental solution for two different deadrise angles for wedges is demonstrated by comparing theoretical results. The Von Karman [5] and Wagner [6] result is constant for various deadrise angles but X. Mei [31] results and those presented here show that the slamming coefficient has downward tendency for high deadrise angles. The Wagner theory is good for low deadrise angles but the gap is increased by the present results and X. Mei [31]. The Von Karman theory is always lower than the other approach which is because the Von Karman theory does not consider the pileup effect.

These measurements were also performed for the hydrophobic coated series. Figure 7.18 shows the strain measurement for the wedge with 7.5° deadrise angle and figure 7.19 for the cone with 30° deadrise angle displays the hydrophobic coated and untreated series comparisons. This gives the expected result for the pileup coefficient and wetting factor and the strain values also decrease.

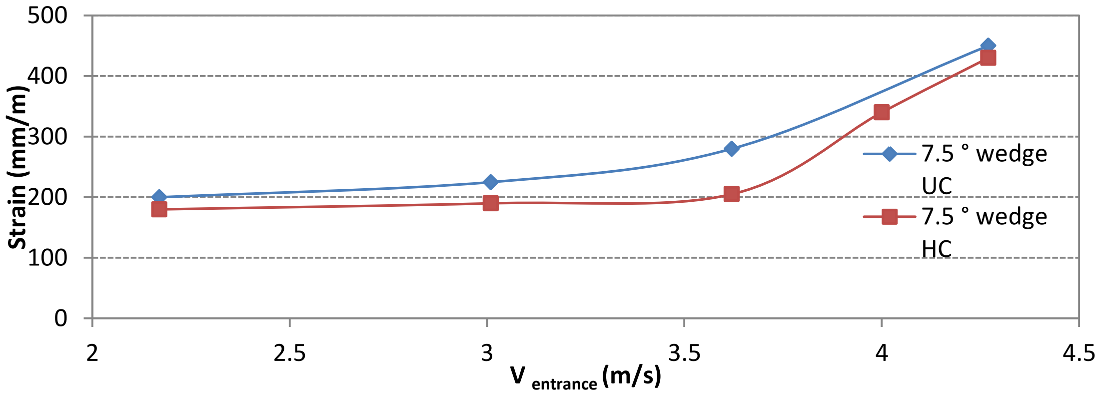

Figure 7.18 The strain measurement for wedge with 7.5° deadrise angle with hydrophobic surface

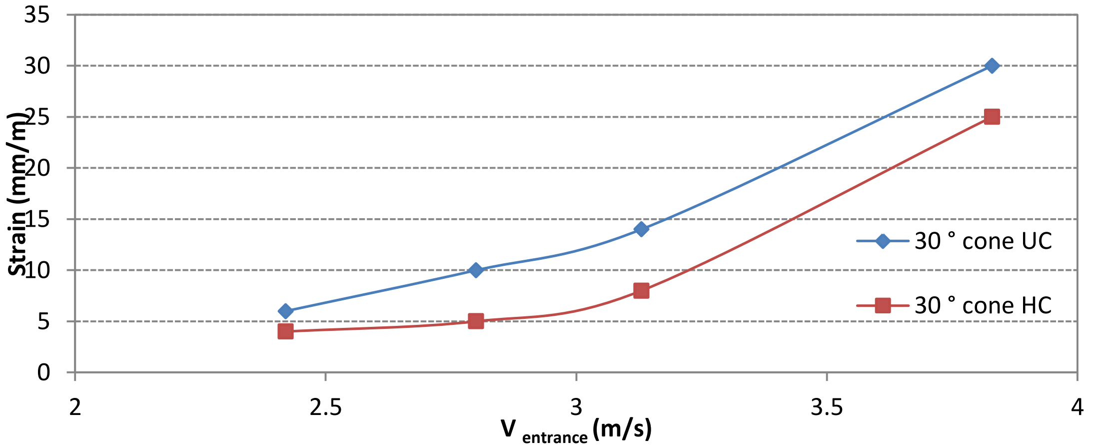

Figure 7.19 The strain measurement for cone with 30° deadrise angle with hydrophobic surface

The hydrophobic coat has been also applied to the cone with high deadrise angle but the comparison is not clear because of the very low strain value for both the untreated and the hydrophobic coated cases. The values of the strain are also converted to force by applying static force load and strain response interaction for the hydrophobic cases. The hydrophobicity changes the behavior of the surface so the pileup coefficient is more than the untreated case because more energy transfers to the fluid during the same time history. The strain measurement is also affected by this situation of repelling more fluid. The wedges or cones have to face less fluid in the hydrophobic case and this has an effect on the strain values.

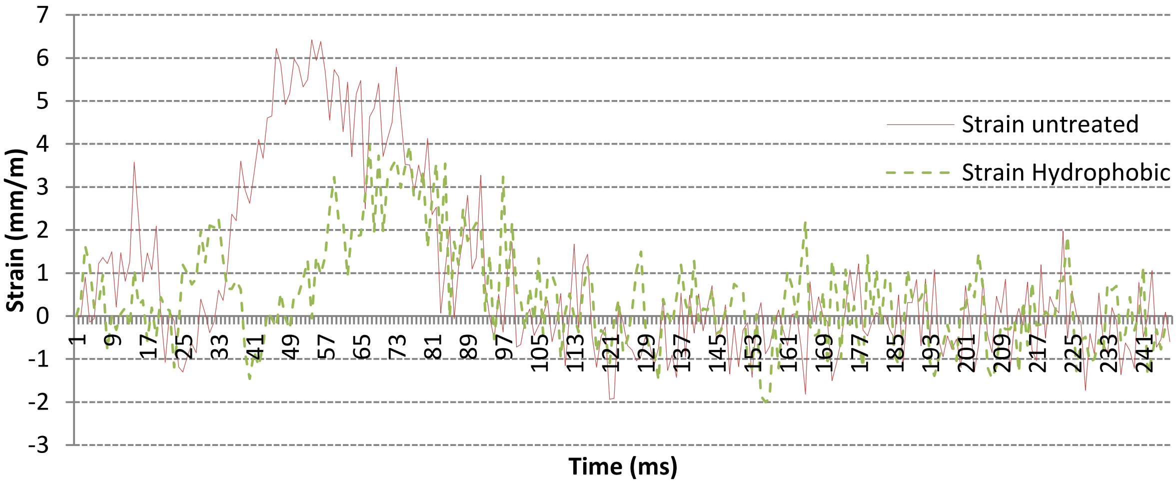

Figure 7.20 The raw strain data for wedge with 30° deadrise angle and drop from 30 cm height

Figure 7.20 presents the raw data for free fall experiments from 30 cm for the cone shaped body at 30° deadrise angle with hydrophobic coated case. In the figure, the hydrophobic results slide slightly to the right side for clarity. Although the characteristics of the slamming impact tests are similar, the impact decreases in the hydrophobic case. Another difference is the time to reach peak value. This can be understood as a separation of the water occurring early so more time is needed to reach the peak value. This time delay also affects the slamming coefficient because of the time which has taken place in the Cs equation.

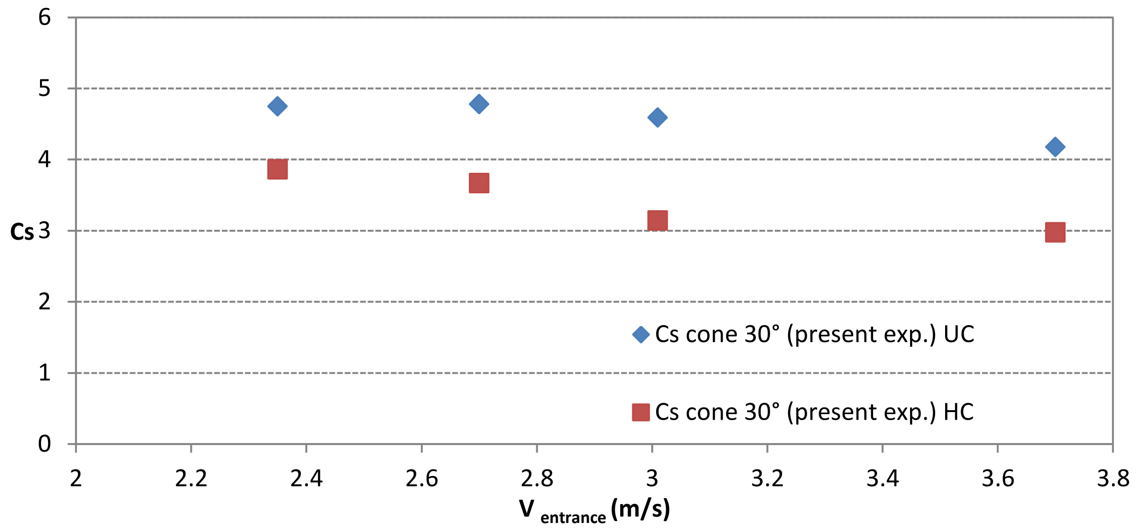

Figure 7.21 The slamming coefficient (Cs) of cone with 30° deadrise angle versus entry velocity

Comparison has also been made considering the non-dimensional coefficient for the cone. The change to the slamming coefficient at the hydrophobic surface is illustrated in figure 7.21. The present solution shows that the hydrophobicity makes a good contribution to reducing the slamming effect.

The strain values for wedge and cone shapes with different deadrise angles are given in table 7.1.[2]

Table 7.1 Strain measurement for wedge and cone with different drop height

	Strain (mm/m)					
Drop Height	Wedge 7.5°	Wedge 30°	Drop Height	Cone 7.5°	Cone 30°	Cone 45°
30 cm	200	58	30 cm	80	6	2
40 cm	225	80	40 cm	110	10	2.5
50 cm	280	90	50 cm	130	14	3.3
75 cm	450	100	60 cm	140	30	4

[2] This chapter was submitted to Applied Ocean Research

CHAPTER 8

THE EFFECT OF HYDROPHOBICITY IN BOW FLARE AND WET DECK SLAMMING

In this chapter, the effect of hydrophobicity has been studied experimentally on bow flare slamming and wet deck slamming by conducting water entry tests with a scaled ship section having bulbous bow and with a scaled catamaran section, respectively. The drop tests were performed from various heights with uncoated and hydrophobic coated models. The differences in jet flows, water pileups and water splashes were demonstrated by comparing high speed camera images obtained for both cases. The pileup coefficient and splash velocity have been calculated via camera images for four different drop heights in each case. The impact loads acting on the surface of the bodies have been measured by applying strain gage measurements and then compared between uncoated and hydrophobic coated surfaces for both models. Results showed that the application of hydrophobic coating on surface reduced the impact effect on bodies as a result of transferring more kinetic energy into the water.

The results showed here were obtained from the tests carried out with the impact velocities of 2.25 m/s for the catamaran section and 3.01 m/s for the bulbous bow section. The water entry processes of the two specimens with uncoated and hydrophobic coated surfaces were demonstrated via high speed camera images. The snapshots of the free fall of the catamaran section that has wedge shape dime hulls with 30° deadrise angle can be seen in Figure 8.1. It can be observed that the jet flow climbs up on the surface and follows the same dime hull angle in the case of the uncoated surface (Figure 8.1a). However the separation of the water occurs earlier on the coated surface (Figure 8.1b). Two jet flows coming from the both sides hit the bottom of the deck at the same time around the same location. However the jet flows collide in the air before hitting the deck in the uncoated case. The horizontal velocity component of the jet flow is much larger under hydrophobicity (Guzel and Korkmaz [79]). In both cases, the air cushioning effect is observed at larger penetration depths.

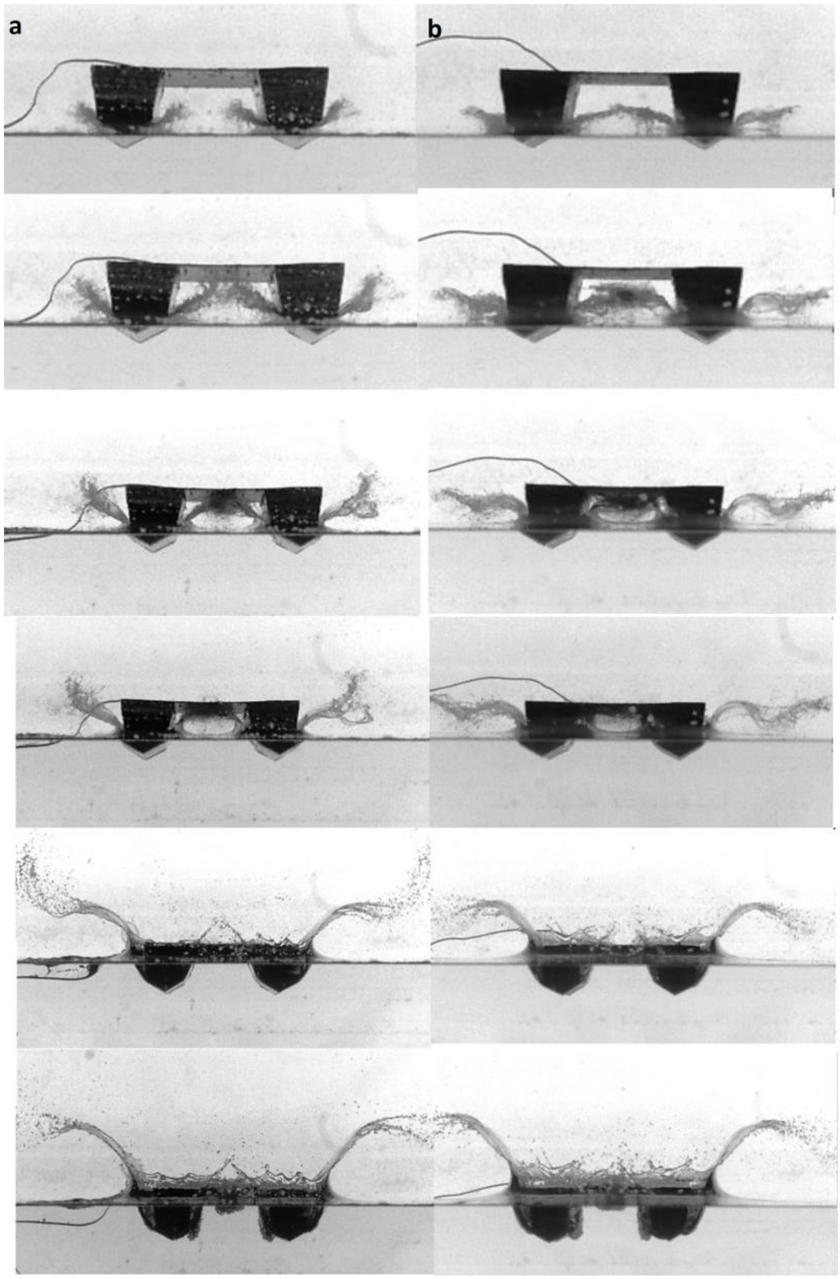

Figure 8.1 Snapshots taken at different time steps of the water entry of a catamaran dropped from 0.3 m. a) Untreated case b) Hydrophobic case

Similarly, the drop tests for the bulbous bow section were performed (Figure 8.2). The separation of jet flow occurs earlier and more volume of water in the splashes and in the pileups are observed with the hydrophobic coated surface (Figure 8.2b). Another interesting point to notice is that the jet flow separates from the surface and hits higher locations of the body under the hydrophobic effects (Figure 8.2b), while it climbs up at the cylindrical bow flare section without separation and follows the varying surface angle on the body in the untreated case (Figure 8.2a). The splashes reach higher and longer distances in the hydrophobic case.

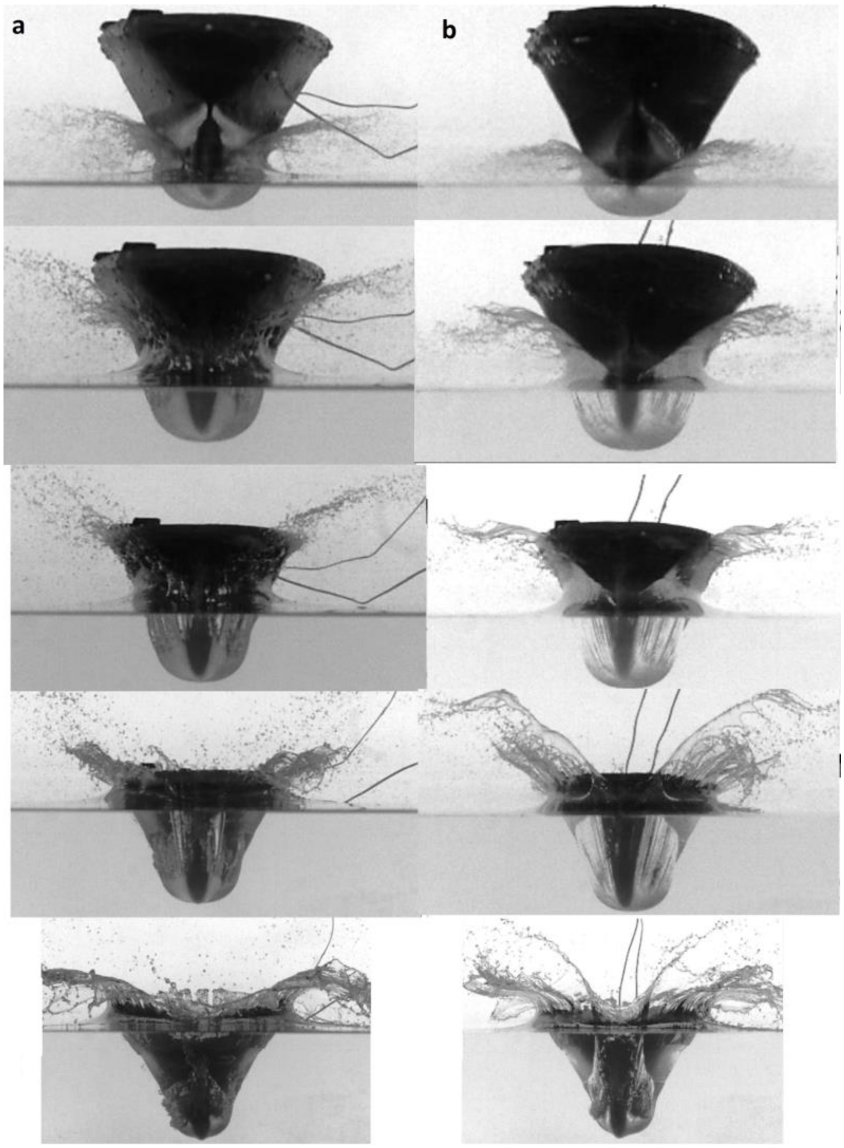

Figure 8.2 Snapshots taken at different time steps of the water entry of a scaled bow flare section dropped from 0.5 m. a) Untreated case b) Hydrophobic case

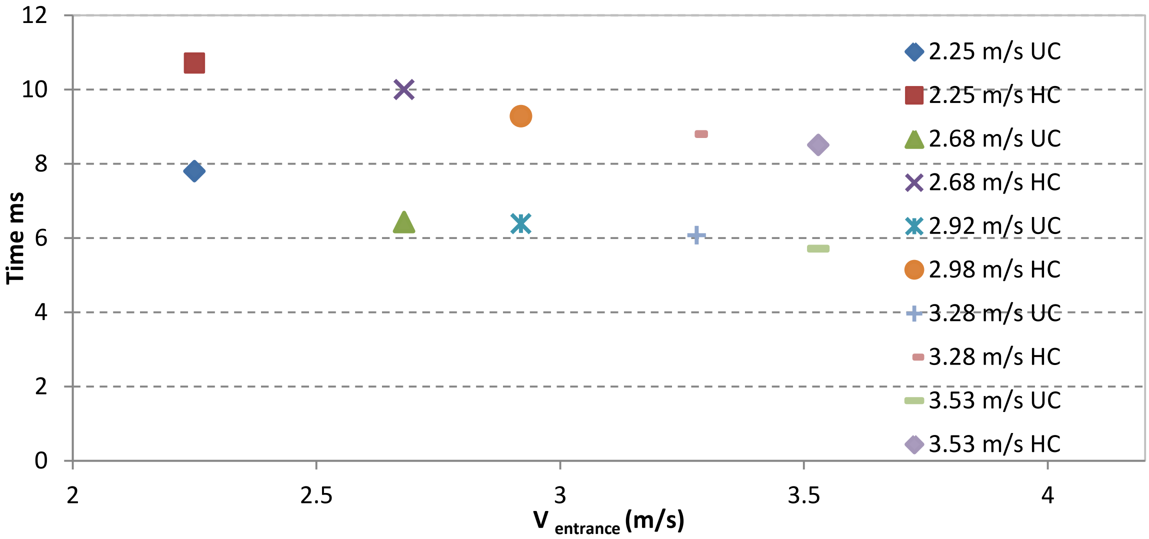

Figure 8.3 The elapsed time when the jet flow hits the wet deck. UC; uncoated surface, HC, hydrophobic coated surface

Figure 8.3 shows the elapsed time between the first touch of the catamaran section to the water and the time when the jet flow hits on the wet deck. From the Figure 8.4 that is plotted against the entrance velocity it can be observed that the jet flow reaches the wet deck at later times with the hydrophobic coated surface.

The impact loads acting on catamaran and bulbous bow sections have been measured by strain gauges. The strain gauges were installed on the deck of the catamaran section, and on the curvature of bulb and above of the bulb on the inner side of bulbous bow section. The drop tests were carried out with five different entrance velocities for each test objects, namely catamaran and bulbous bow sections. Each velocity value was tested three times in order to see the reproducibility.

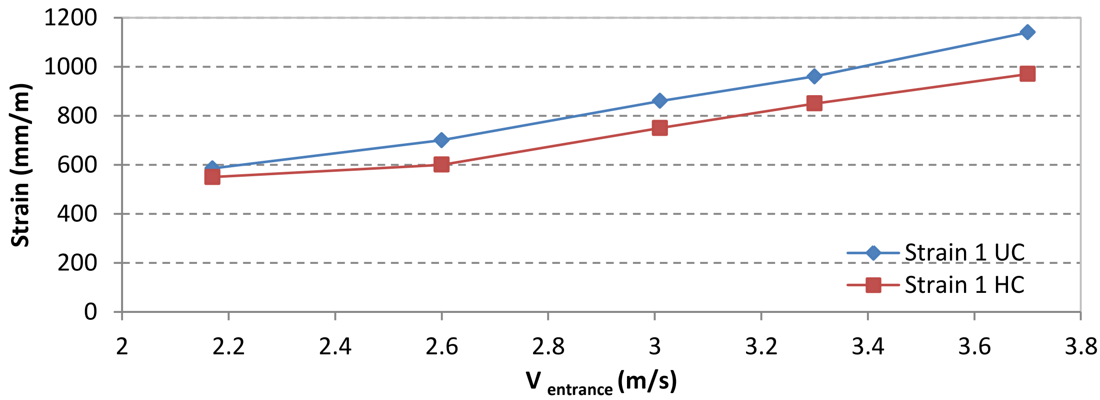

Figure 8.4 Peak strain values from the strain gauge installed on the deck of the catamaran section as a function of the entrance velocity

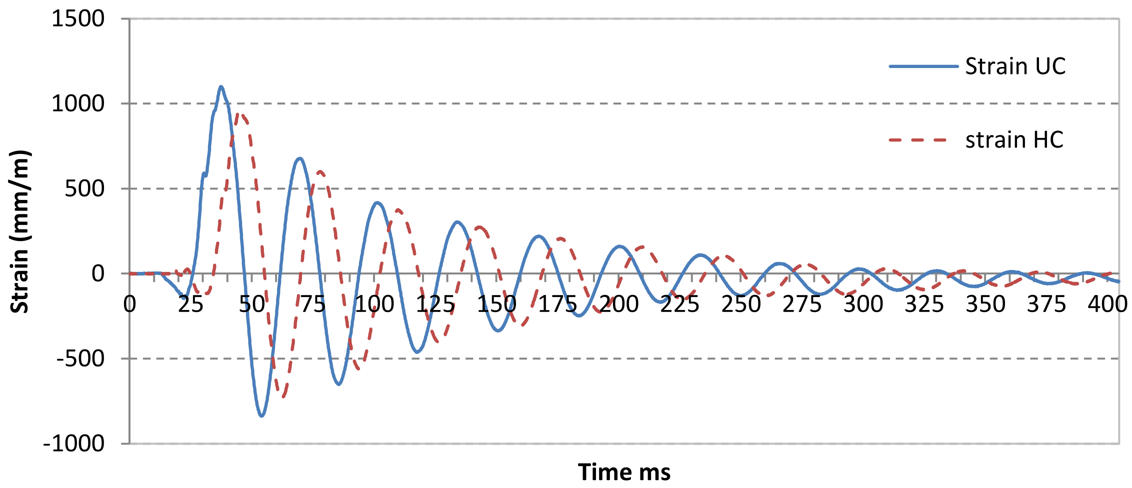

Figure 8.5 Time plots for the strain gauge installed on the scaled catamaran section for a drop height of 75 cm and an entrance velocity of 3.7 m/s.

Wet deck slamming occurs when the top of the wet deck touches the free water surface. At this moment, the strain gauge installed on the deck reads its maxima. This strain value represents the impact load during wet deck slamming. Figure 8.4 shows the maximum strain values as a function of the entrance velocity. The peak value is smaller under the hydrophobic effects for the same hydrodynamic conditions. In all experiments conducted with this catamaran section model, with the hydrophobic coated surface, the strain gauge read lower level of strain values at a rate of 10-15% for various entrance velocities. These low strain values are due to more kinetic energy transfer to the water. Larger amount of water is pushed away when the hydrophobicity is present. Figure 8.5 shows a sample of the strain time histories for the test object for the drop experiment done with the entrance velocity of 3.7 m/s for both uncoated and hydrophobic coated surfaces. In Figure 8.5, the data for the hydrophobic case is shifted to the right for clarity. It can be observed from the Figure 8.5 that the hydrophobic effect is present at the beginning of the impact. The magnitude of the peak value with the hydrophobic surface is at the same level as the uncoated surface at the later stages of the impact.

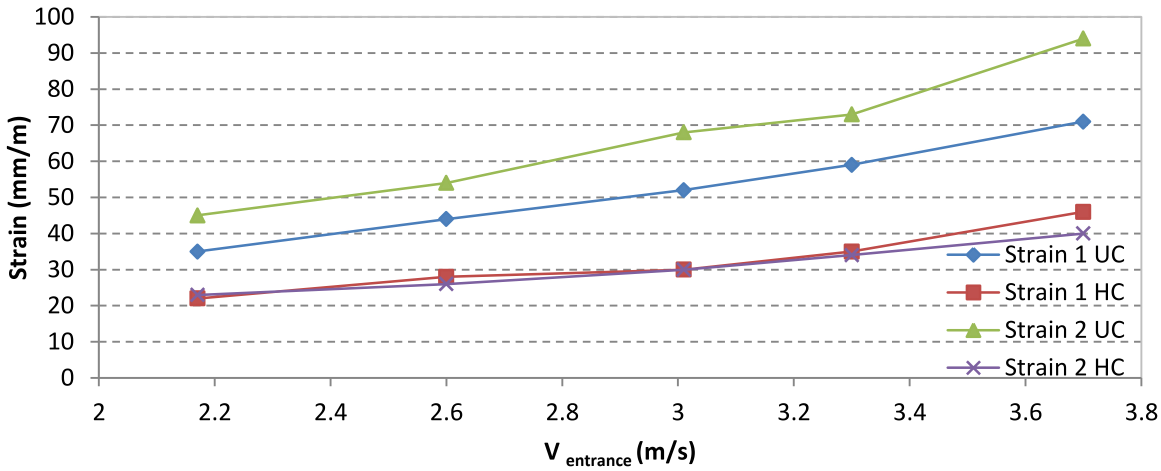

Figure 8.6 Peak strain values for the strain gauge 1 and strain gauge 2 installed on the inner surface of the bow flare section as a function of the entrance velocity

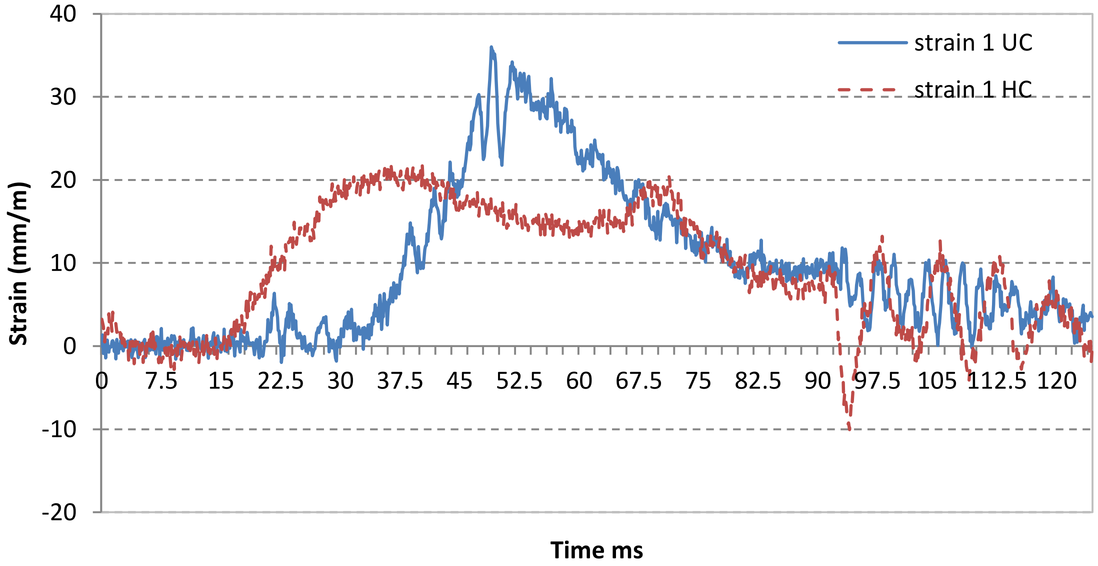

Figure 8.7 Time plots for the strain gauge installed on the bow flare section for a drop height of 30 cm and an entry velocity of 2.17 m/s

The result of the free fall test of the bulbous bow section is indicated in Figure 8.6. The peak value is smaller under the hydrophobic effects for the same hydrodynamic conditions. The differences between the both cases are much higher in the second strain because of its location where the separation of the flow occurs. The hydrophobic coating creates more dominant effect at the blow flare slamming. It is because the propagation of the impact pressure is more efficient due to the shape of the bulbous bow. Figure 8.7 shows a sample of the strain time histories for the test object for the drop experiment done with the entrance velocity of 2.17 m/s for both uncoated and hydrophobic coated surfaces. It can be observed form the Figure 8.7 that the response characteristics of the slamming are also changed under the hydrophobic effects.[3]

[3] This chapter was published in Twenty-sixth (2016) International Ocean and Polar Engineering Conference

CHAPTER 9

EXPERIMENTAL INVESTIGATION OF WATER EXIT UNDER HYDROPHOBIC EFFECTS

Prediction of hydrodynamic loads during water exit of a body is of a great importance in designing the marine vehicles that take off from the free water surface such as sea planes and wing-in-ground effect vehicles (WIG), and that pierce through the free surface like missiles and submarines. The results of an experimental investigation on water exit of three different geometries, sphere, cylinder and flat plate, with hydrophobic surfaces are presented in this chapter. With and without the hydrophobic effects present, different fluid dynamics phenomena like free surface evolution, deformation and break up of free surface, wave generation, splash, air entrapment and water detachment from the solid surfaces during a water exit event have been examined. The non-dimensional exit coefficient, C_e is a function of the total vertical hydrodynamic force which depends on the geometry of the object and the hydrodynamic conditions along with the water parameters. Our study is aimed at understanding and modeling the nonlinear free surface effects and the dynamics of water exit under an extended range of parameters including hydrophobic effects.

In this chapter, due to lack of the experimental data on water exit problem in literature, water exit tests have been set up, first for initially partially immersed spheres and flat plates, with their center above the free surface, to be towed vertically from the water surface at various speeds. Secondly, buoyancy driven water exit of a fully immersed sphere is investigated. It is observed that when the sphere rises up, it first starts deforming the free surface, and then pierces into it. The thin water layer attached to the surface of the sphere is drawn back to the test tank as the sphere moves further upward. This causes breaking of the free surface, air entrapment and wave generation in the water. Thirdly, the cylinder is used at fully immerse water exit test. The water also attached on the cylinder and cross the free surface line by helping buoyancy force.

From digital images captured using a high speed camera, free surface breakup and water detachment at different velocities are observed and the time evolution of the water detachment and the exit characteristics are measured during the water exit event. The position of the sphere, cylinder and its velocity are plotted against time. A detailed measurement of the global loads on the test objects during exit is carried out by employing strain gages.

We also showed the effects of water detachment on the test bodies during and after exit via strain gages. All this data is also collected under the hydrophobic effects, to show how the change in surface characteristics could have significant impacts on the water exit phenomenon. Understanding the difference in occurrence of the water flow separation, the change in the kinetic energy of the fluid and the free surface deformation under the hydrophobic effects could help give a better explanation of the phenomena observed during water exit and improve the design characteristics of marine structures in a water exit event.

Firstly, the results presented here are for the initial exit velocities of 0.74 m/s and 1.23 m/s for partially and fully immersed bodies, respectively. A preliminary series of tests were performed with only qualitative image analysis via high speed camera images.

In case of positive buoyancy, the buoyancy force causes continuous upward motion of solid objects. When a sphere exits water vertically in buoyancy driven water exit event, its vertical velocity makes a maxima and remains unchanged for a short period of time at the beginning of the exit, right at the moment of piercing through the free surface. As the sphere approaches the free surface, the fluid above the sphere rises up and the free surface deforms continuously and progressively shapes a curvature to the radius of the sphere. During such an event, a thin layer of water around the sphere moves along with the sphere and lifted out of the water. After the sphere exits completely, the water layer around the sphere flows down onto the free surface due to gravity. But water isn’t left the surface of the sphere completely, the thin layer stay on the surface for all releasing height.

In this chapter, the water exit phenomenon was investigated in three parts. At first, a sphere rising due to its buoyancy is observed in the test tank. The snapshots taken during water exit of a fully submerged sphere are shown in Figure 9.1. The sphere center is located at a depth of 7 cm below the calm free surface. The surface elevation is observed and then compared with the results obtained from the hydrophobic case. It can be seen from the images that the free surface deformation in water-exit of a circular sphere is non-linear. The initial submergence depth is one of the dominant parameters that affect the exit characteristics. The free surface far from the vertical location of the sphere is not influenced by the movement of the sphere.

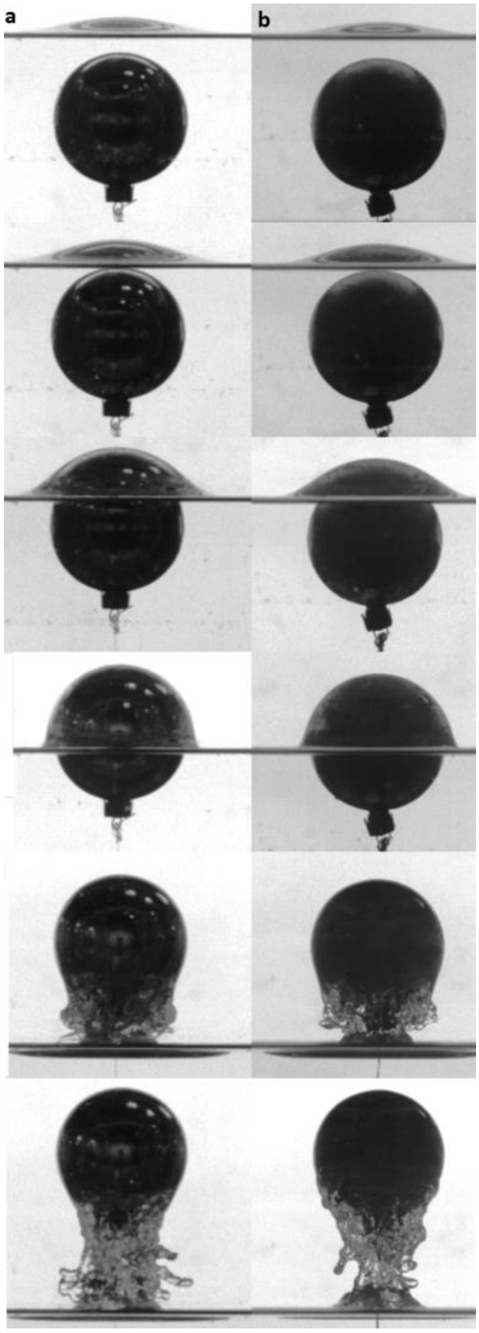

Figure 9.1 Snapshots taken during the water exit of a fully immersed sphere at Re=7x104. a) Uncoated surface b) Hydrophobic coated surface

The change in surface profile due to the water exit of a sphere can be seen in Figure 9.1. Although the water layer above the sphere is expected to be thinner under the hydrophobic effects, no significant difference has been observed from the images between the cases with hydrophobic surface and uncoated surface. The position of the sphere and its local velocity calculated from the high speed images are plotted in Figure 9.2. For each release depth, at least three exit tests were performed to see the reproducibility of the calculated velocity values. Considering the image resolution (640x480 pixels) and the recording speed (1400fps) of the camera, the scatter of the test results for each point is not large and lies within ±4% of the mean value.

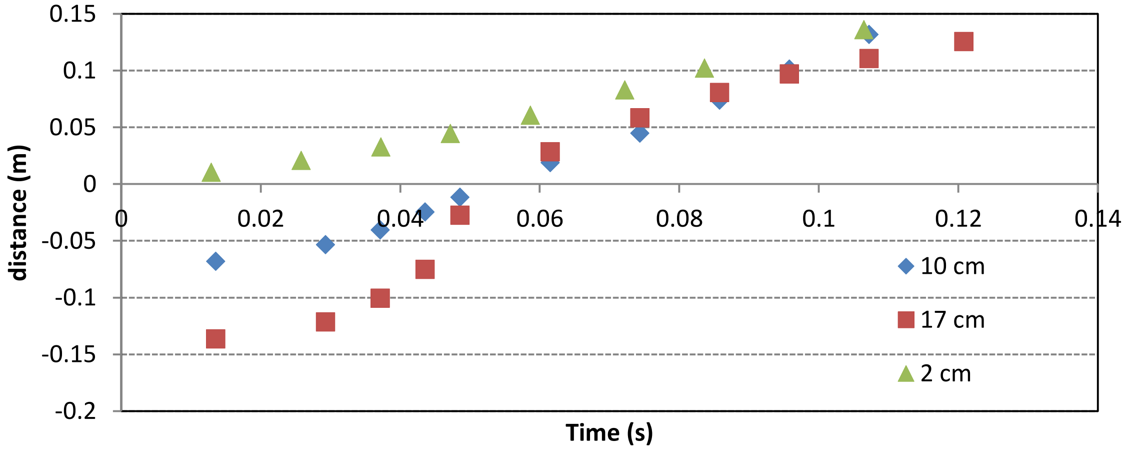

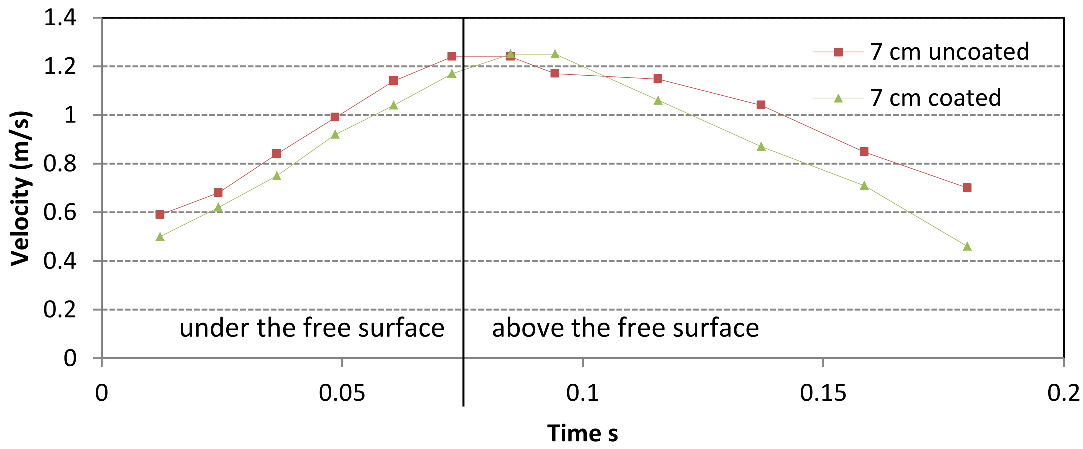

Figure 9.2 Water-exit of a fully immersed sphere; Position and velocity of the center of the sphere.

For the strain measurements, a plastic ball with a larger diameter of 16 cm and a mass of 120 gr was used. The main reason is the need for having a larger surface area to investigate the surface effects better. Also increasing flexibility would give much better response, in terms of strain values, to the change in global loads, if any, during an exit event under hydrophobic effects. Figure 8.3 shows samples of strain time histories for the plastic ball (uncoated) for the water-exit experiments done from the release depths of 2, 4, 8, 14 and 20cm below the undisturbed free surface. The strain recordings are not of sudden peak values but build up more gradually in time as the object moves up with increasing velocity under the continuous buoyancy force. The images shown in Figure 9.3 show the corresponding positions of the ball stated on the time plot of the strain values as a, b and c. Point a represents the first moment that the surface elevation is observed. Point b represents the moment that the strain value starts decreasing after it has reached its maximum. Point c represent the moment that the strain value reaches its initial value at zero velocity when fully submerged. It can be seen that as the release depth below the free surface is increased, the amount of the added mass moving with the object is increased.

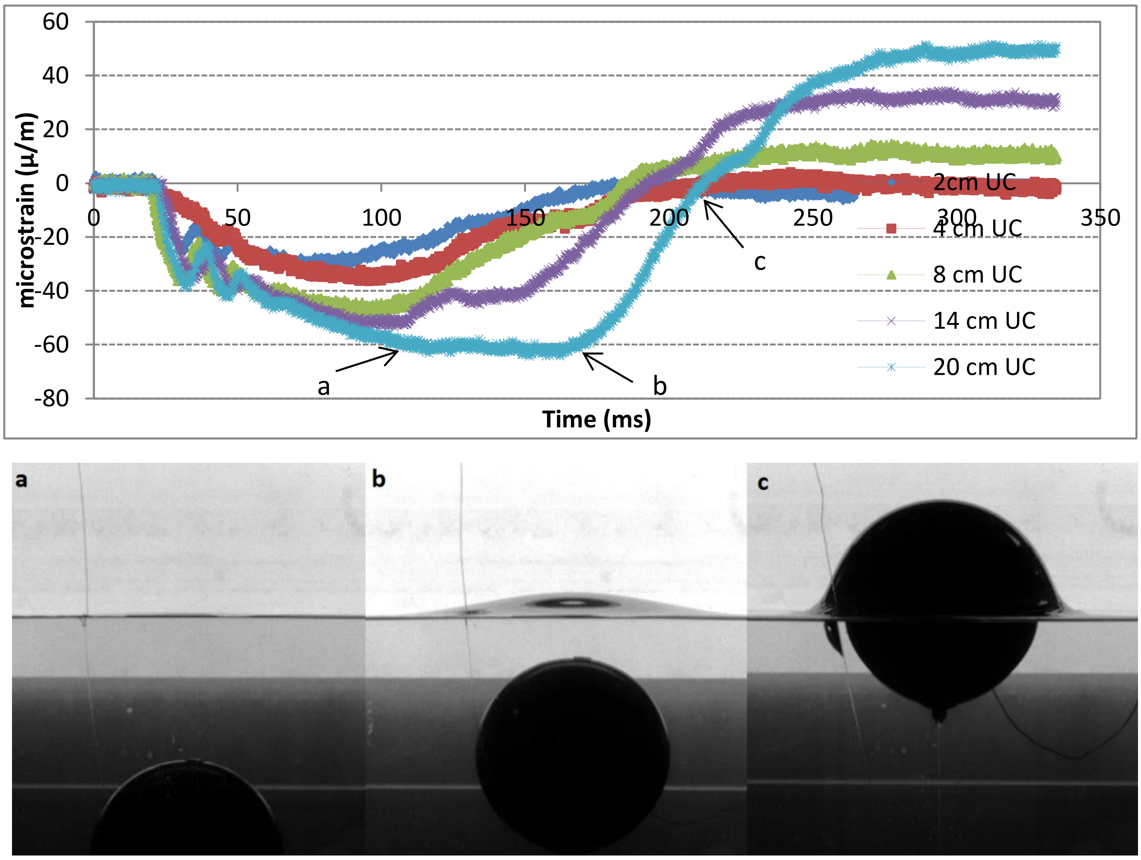

Figure 9.3 Time plots for the strain gauge installed on top of plastic sphere (uncoated) during water-exit events at different release depths. a) 12 cm below b) 3.5 cm below and c) 10 cm above the undisturbed free surface for the release depth of 20 cm.

Figure 9.4 shows samples of strain time histories for the plastic ball exit experiments under the hydrophobic effects, done from the same release depths as in Figure 9.4. The images shown in Figure 9.4 also show the corresponding positions of the ball stated on the time plot of the strain values as a and b. The characteristics of the strain time histories under the hydrophobic effects differ from the ones with the uncoated surface. While the repeatability of the strain measurements is observed under the same test conditions when no hydrophobicity is present, the strain characteristics vary under the hydrophobic effects for the same test conditions. But the peak strain values are same as uncoated tests.

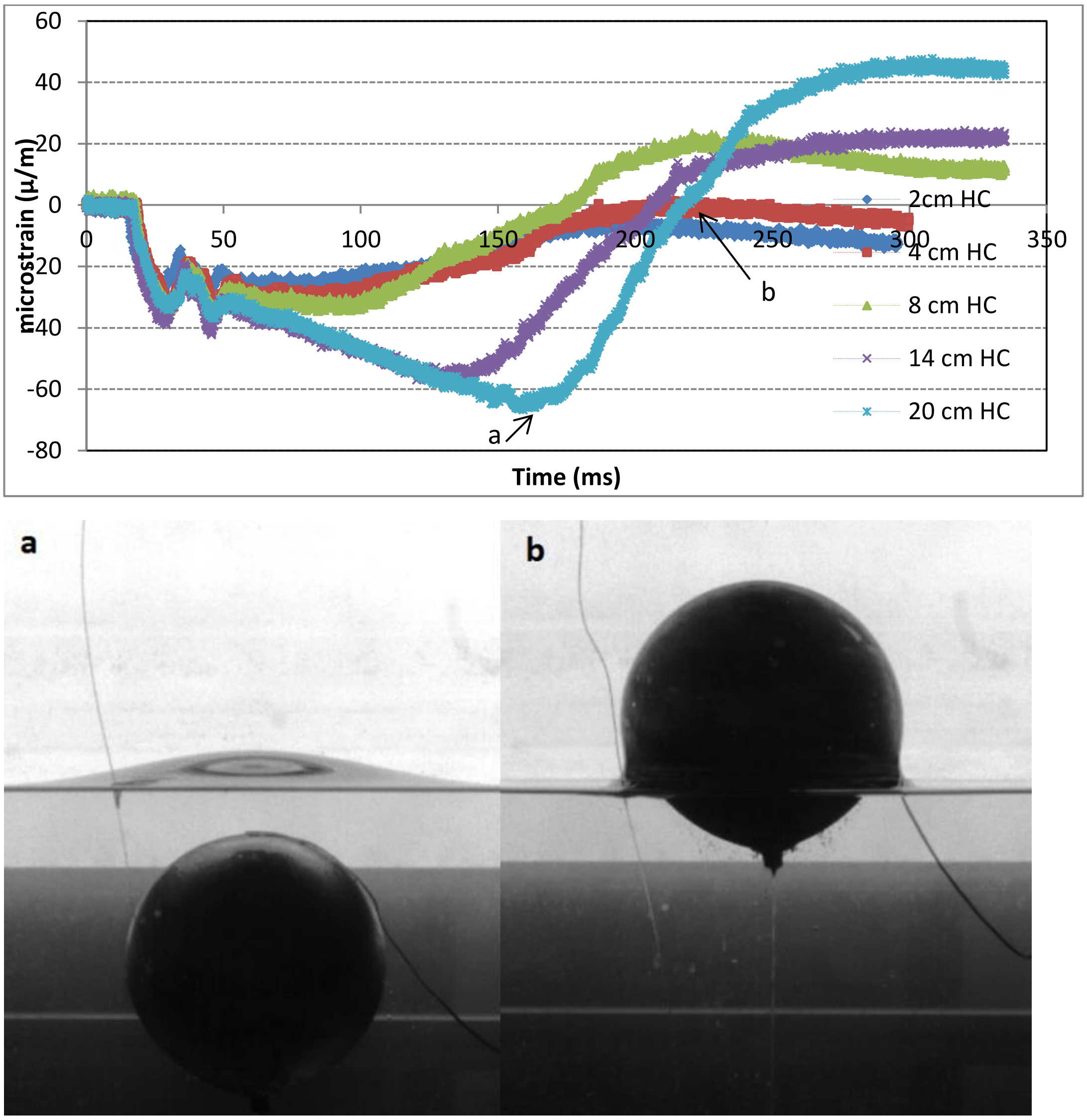

Figure 9.4 Time plots for the strain gauge installed on top of plastic sphere (hydrophobic coated) during water-exit events at different release depths. a) 2.8 cm below and b) 13.4 cm above the undisturbed free surface for the release depth of 20 cm.

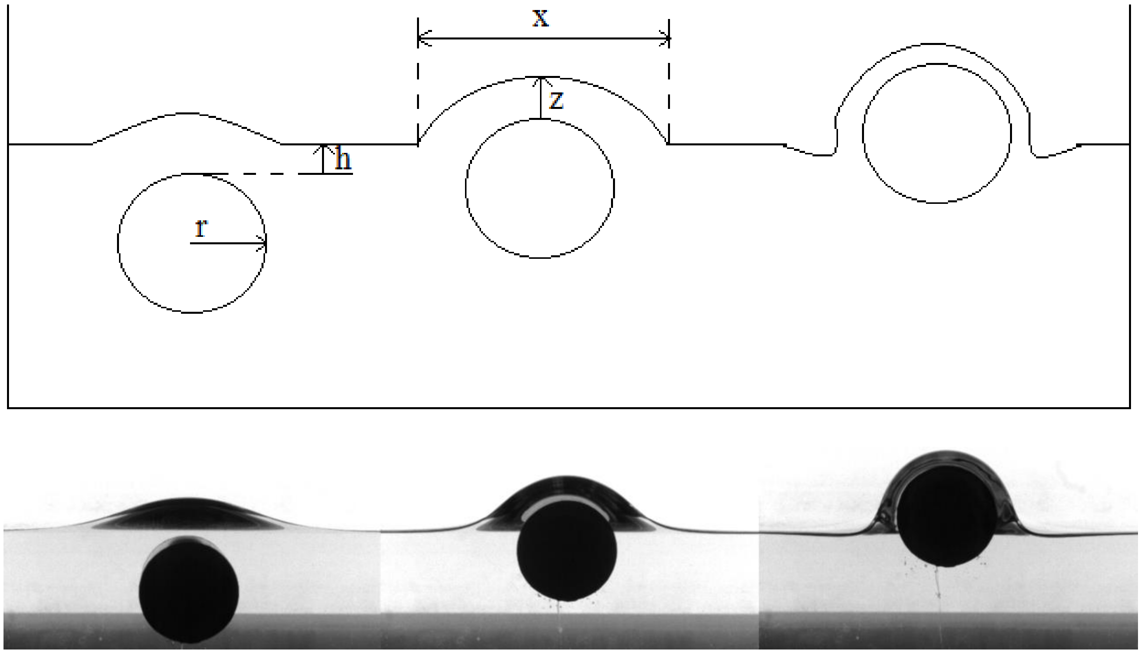

Figure 9.5 The water exit of cylinder

The second part of study is performed by cylinder. The cylinder is made of acrylic and the radius is 10.8 cm and the length is 20 cm. The water exit of cylinder rises with added mass like entry event. The cylinder is used to visualize clearly the waft of water around of it. The provoked water comparison is made for nine different depths by front thickness of cylinder and horizontal range of rising water. The figure 9.5 demonstrated the sketches and instant pictures of water exit of cylinder by showing measured lengths. The hydrophobic coated tests are also experienced by same condition with uncoated tests.

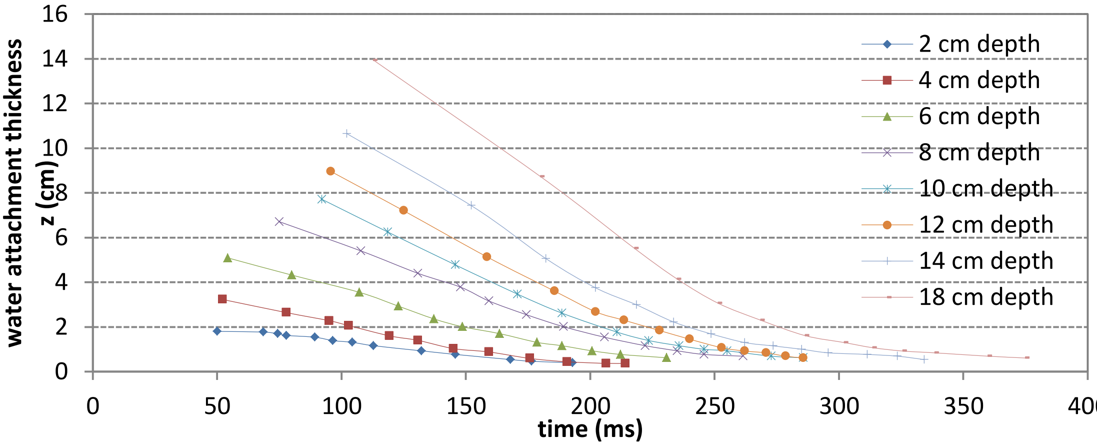

Figure 9.6 Vertical and horizontal thickness of water above cylinder versus time and their ratio versus time

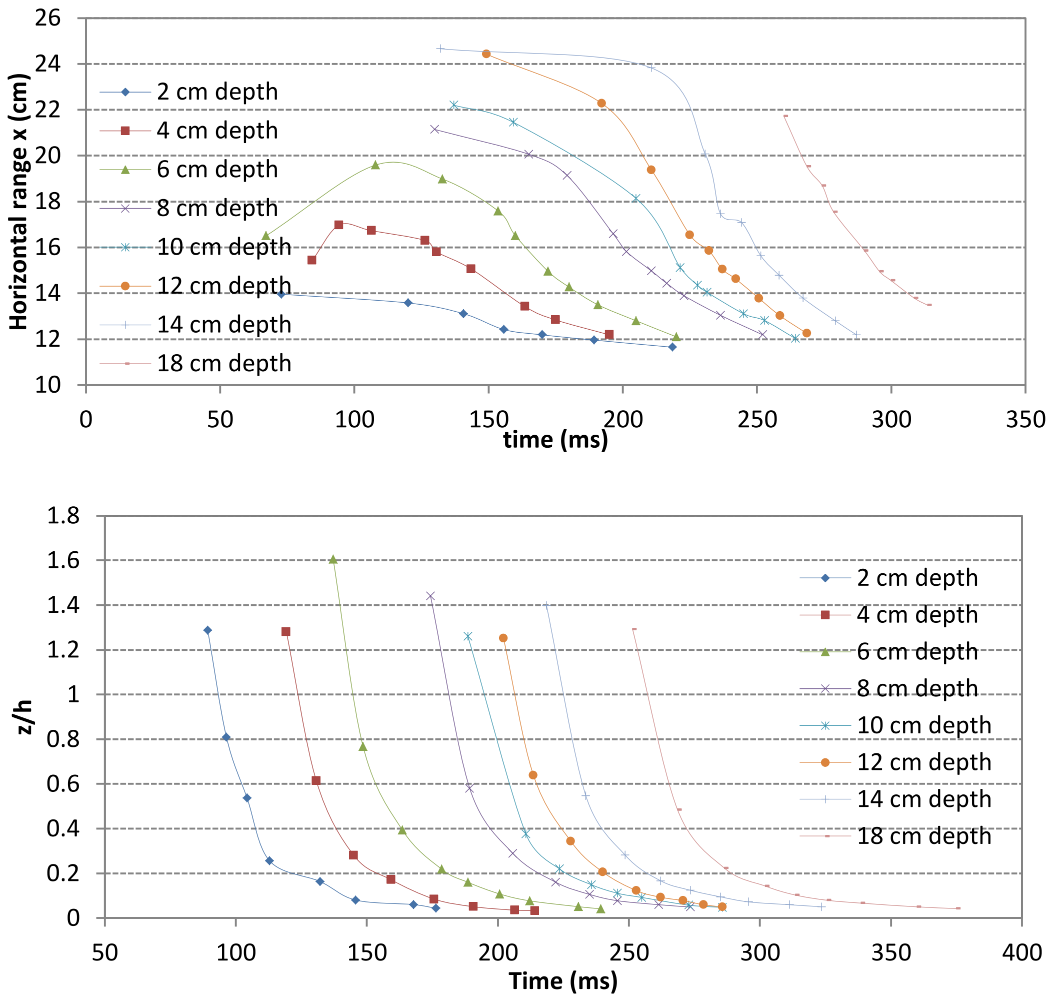

Figure 9.7 Vertical and horizontal thickness of water above cylinder versus time and their ratio versus time (cont.)

The front and horizontal thickness of the water which is occurring at water exit on cylinder around are demonstrated at the figure 9.6. The added mass calculation can be made for per unit length by $m = \frac{\pi}{2}\rho r^2$ at cylinder shape. The same variable is for different depth values at added mass formulation but the volume of pushing water is change. These results are expected that the measured thickness are increased by releasing depth increase because the added mass of the cylinder cannot be collect the effected water surface for its diameter especially at small depth values. The figure 9.6 is also show ratio of cylinder front and horizontal thickness versus time. It is clearly show that the similar ratio values are captured for all depth values. But the process of the water exit is occurred different time period. The measurements of thickness are started generally at closing the free surface and stopped when the cylinder is located on the free surface.

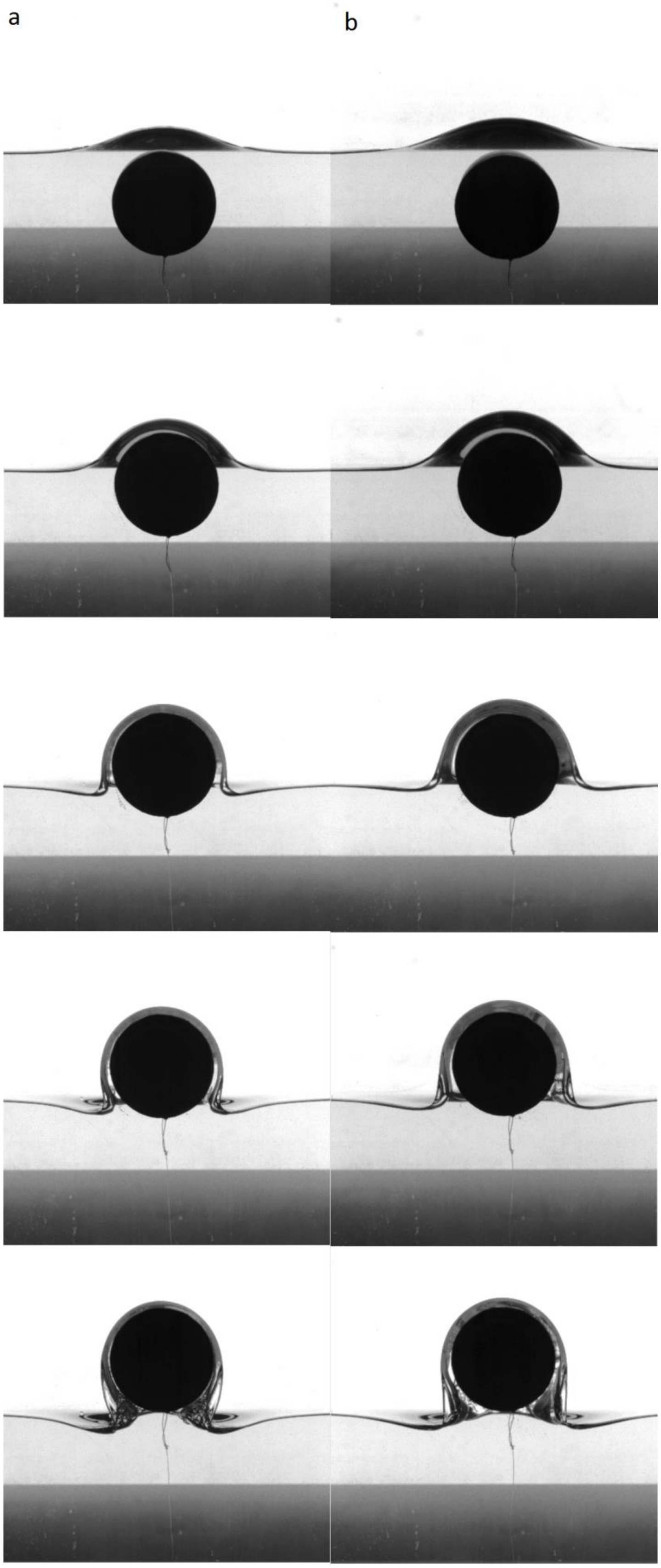

Figure 9.8 The process of water exit a) release depth from 6cm, time sequence; 102ms, 138 ms, 168ms, 179ms, 197ms, b) release depth from 14 cm, time sequence; 182ms,212ms,237ms,249ms,265ms

The sequences of water exit which are released from 6 cm and 14 cm are demonstrated at figure 9.7. The same position is capturing both situations that are arranged from tip of cylinder to free surface. The cylinder fully rising process is need to 95 ms at 6 cm depth but it takes 83 ms for 14 cm depth case. It is also easily observe from sequences pictures that the volume of the water is more at the water exit test from 14 cm depth.

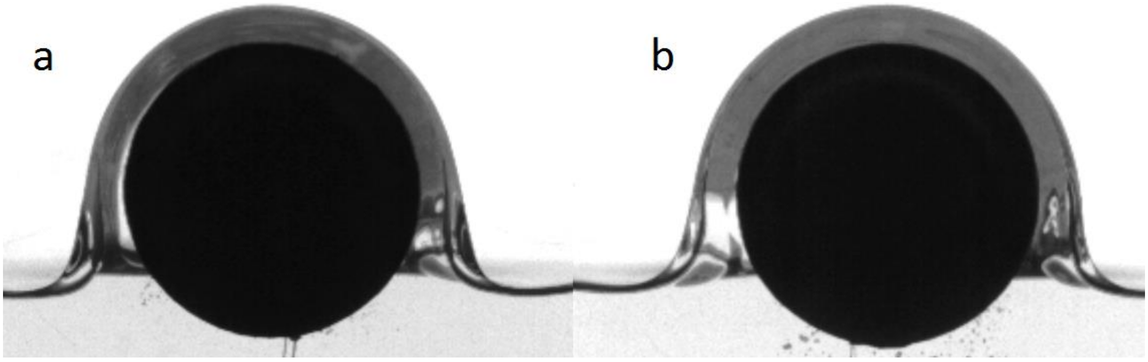

Figure 9.9 The water exit of cylinder a) hydrophobic case b) untreated case

The cylinder is also coated by hydrophobic material and the all test is performed also by this case. The figure 9.8 shows the instant picture of hydrophobic and uncoated cylinder water exit from same release depth and time. There is no significant differences are observed like other cases. The strain measurement also made for hydrophobic case and the comparison depict at figure 9.9. This is the other indicator that hydrophobicity isn't show the expected effects at the water exit of the fully penetrate test. Because there isn't any connection by third phase, in other words the samples are surrounded by water so the all air gaps are full fill at the fully penetrate stage. Therefore it can't increase the contact angle contrast to water entry.

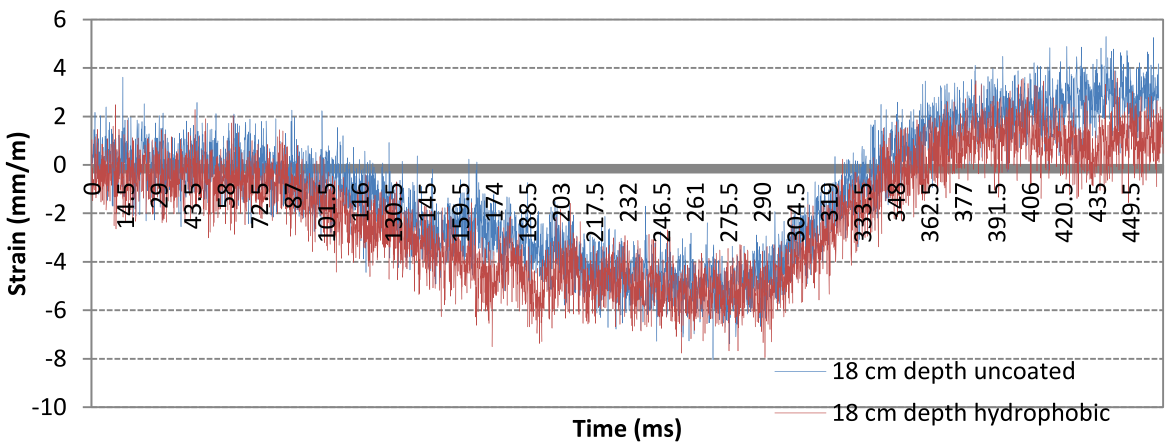

Figure 9.10 The strain measurement of water exit cylinder

The strain measurement is also performed for cylinder water exit experiment. The tip of the cylinder is selected for the placed of strain gages. The figure 9.10 is demonstrated the comparison with three different releasing depth. The strain characteristics are similar as sphere water exit measurement. The amplitude of the strain values is wide because the water exit isn't the instant event like water entry. The strain gages are reached the peak values at 2- 4 ms approximately for water entry but the values is increased to 150-250 ms approximately for water exit. The case of the strain gages tension takes more time and value at the deeper release depth test. This is the other indicator for carrying more fluid in front of the cylinder when it released at the deeper distance from the free surface.

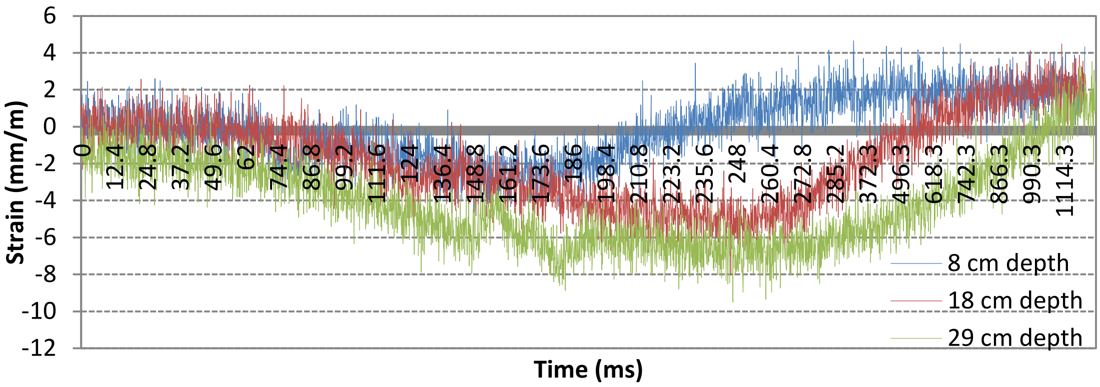

Figure 9.11 The strain measurement of cylinder at different release depth

As the third part of this study, forced exits of a partially sphere and a flat plate are investigated. A mass of water moves out along with the moving object and the amount of this water mass depends on the exit velocity and the surface property. As the object moves up, the added water on the object starts flowing down creating a water column, and at a certain moment this water column breaks up from the object's surface. This moment of break-up is referred as pinch-off of fluid, similar to pinch-off of cavity in water entry of solid objects. Figure 9.11 shows the water detachment during the water exit of a partially submerged sphere. As can be seen from the images taken at several time instants, water detachment occurs faster and the fluid pinch-off occurs much earlier at a smaller height under the hydrophobic effects. The pinch-off times and pinch-off distances are plotted against the exit velocity in Figure 9.12. And Figure 9.11 shows the water detachment during the water exit of a partially flat plate sphere. Again the flow separation occurs at much earlier time span.

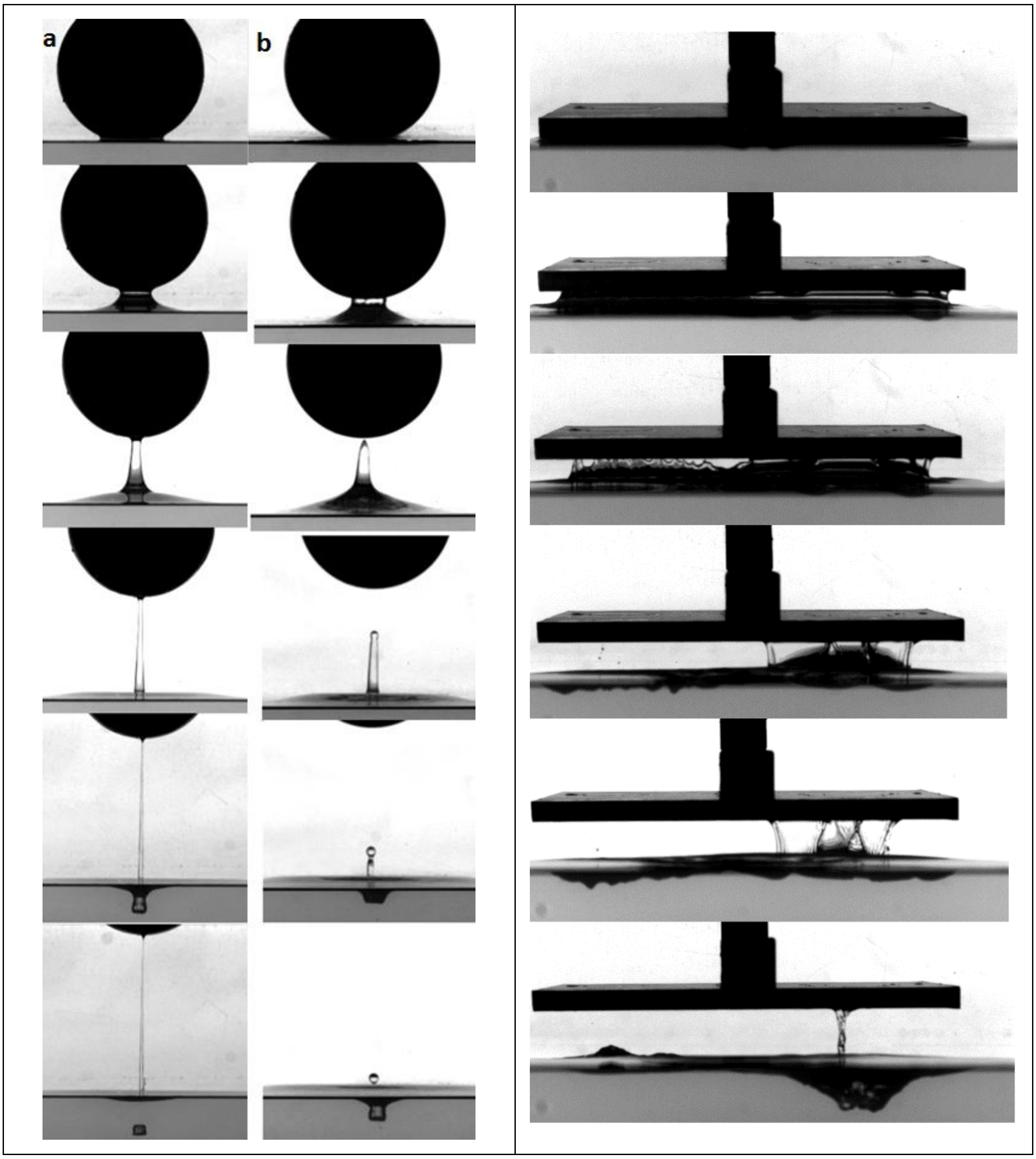

Figure 9.12 Snapshots taken during the water exit of a partially immersed sphere (0, 68, 92, 110 and 116 ms). a) Uncoated surface b) Hydrophobic coated surface c) Snapshots taken during the water exit of a partially immersed flat plate. Left side is hydrophobic coated.

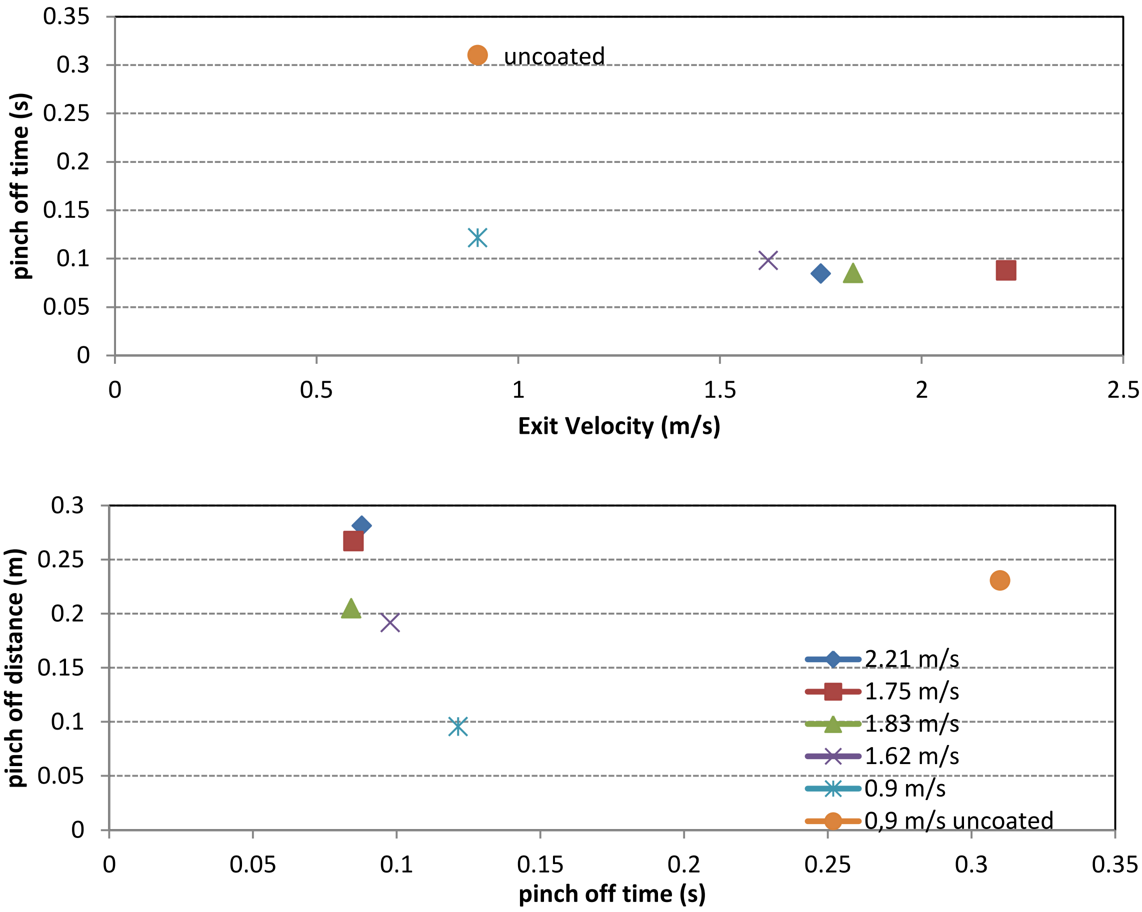

Figure 9.13 Water-exit of a partially immersed sphere; Pinch off time vs. exit velocity[4]

[4] This chapter was published in ASME 2016 35th International Conference on Ocean, Offshore and Arctic Engineering

CHAPTER 10

NUMERICAL INVESTIGATION OF THE WATER ENTRY OF A CYLINDER AT VARIOUS ENTRANCE VELOCITIES

Slamming is an impact force that occurs on ship structures during sailing in rough sea conditions. Slamming produces large impact forces in a short time period. This impact can cause local fatigue damage and also generate vibrations to the entire body of the ship. The present chapter presents numerical simulation of the impact problem of cylindrical shapes dropping to the free surface of the water. The ANSYS Fluent program is used to examine the slamming phenomenon, when considering the impact of the rigid 2D cylinder. Five different drop heights were simulated to investigate the different dynamic conditions. The properties were set as the same as those used in the cylinder experiments. The intersection of two phases was performed by applying the volume of fluid method.

Validation of the numerical studies is made through the presented experimental results. The experimental setup consisted of a water basin and one sliding mechanism supporting four aluminum abutments to perform the free fall experiments. A flexible circular cylinder was used in the experiments and entry velocities were adjusted by changing the drop heights. These were compared with the numerical results and provide snapshots of the penetration process and non-dimensional impact force coefficient under the same hydrodynamic conditions.

10.1 Numerical Method

The conservation of mass and momentum governing equations were solved by the finite volume method. The ANSYS Fluent commercial code ver. 16.1 was run on a computer which has 2.30GHz Intel core i7 processor with 8GB RAM features. The computational grid is established by ANSYS Workbench 16.1 version. The fluid domain is divided into 166550 cells on the computational grid. The segregated flow method is employed to solve the equations of flow in the connecting momentum and continuity equations. The solver is essentially a Semi-implicit method for pressure linked equation (SIMPLE) type of algorithm. The Volume of Fluid Method (VOF) is used for modelling deformation of the free surface. The VOF is identified in each cell and is a way of tracking the variables of the fluids (M. Rahaman et al. [94]). The variables are only for the stated volume cell. All the fluid variables can be reached by the total of the variables of each cell, separately. The 6-Dof UDF file is utilized to track the motion of the cylinder. The gravity and buoyancy forces are the reasons that the cylinder experienced the force.

The geometry and meshing part are generated in the ANSYS Workbench program. The mapped face meshing window is applied on the model and a high number of divisions is selected to increase the mesh quality because insufficient mesh quality can be the reason for the crash of simulation and wrong solutions. Generally, a poor quality of mesh is the reason of negative or zero cell volume errors. A triangular mesh type is used for the domain. The number of divisions is also applied near the cylinder, and the close cylinder line is chosen as 0.0003 to be more symmetrical and for better analysis. An overview of the mesh is demonstrated in figure 10.1. Approaching the true velocity and force values can occur by selecting small mesh elements. The cylinder water entry simulation is experienced by running the cylinder through the water surface. The cylinder mesh zone proceeds through water line therefore dynamic mesh is selected. The dynamic mesh zone should be introduced to define where the computational grid changes dynamically.

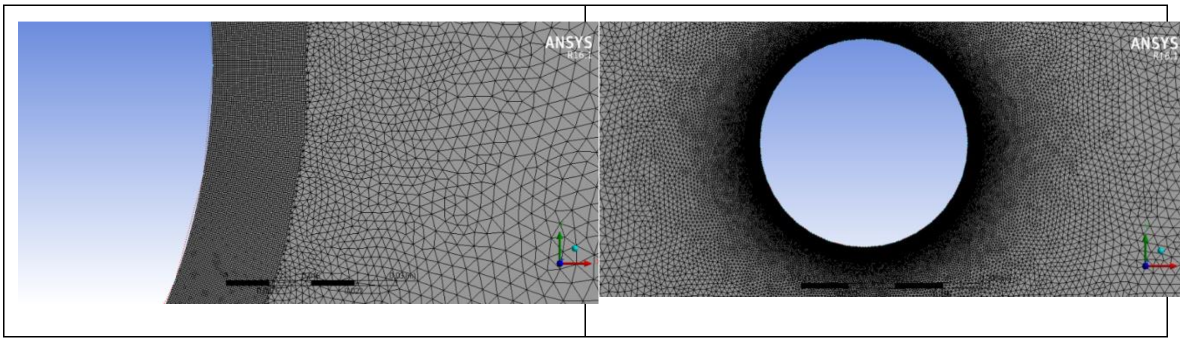

Figure 10.1 The demonstration of mesh around cylinder

The selected time step is also an important issue for accurate calculations. The different time steps are applied and evaluated for reductions in the computational time.

Especially, small time steps are required on first contact with the water because of the instant impact, pileup and spray occurring at this stage. The 0.00001 s time step is selected for all simulations at current CFD analysis and 0.000005 s time steps are also chosen for the some case.

The domain of the studied problem is illustrated in figure 10.2. The size of cylinder and water basin is taken from experimental study of the vertical and horizontal coordinates.

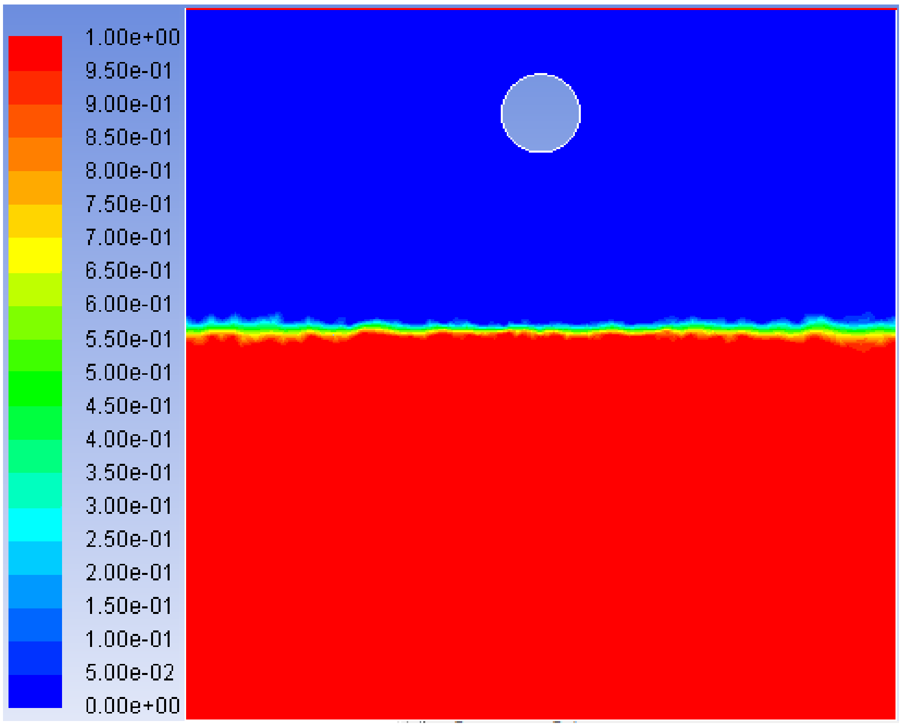

Figure 10.2 Overview of cylinder water entry with ANSYS Fluent program.

The volume domains are framed by three walls and one inlet, as the boundary conditions. Two phases are defined: water-liquid and air.

The other selection feature for analysis is the discretization parameter before starting simulations. Discretization is a way of describing the transformation of the integral form of the governing equations to linear algebraic equations. ANSYS Fluent represents two discretization solvers, first order and second order schemes. The second order causes more accurate solutions by consuming more time than the first order scheme. Second order schemes are preferred.

10.2 Analytical approaches of the cylinder water entry

The water entry of cylinders is studied by asymptotic expansion to calculate the dynamics of impact. (S. Abrate [7])

The calculation of cylinder slamming by Von Karman is as follows:

The implementation of Newton's second law for water entry of the cylinder can be formulated:

$$M\ddot{\zeta} = Mg - F - F_b - F_c - F_D \tag{10.1}$$

where ζ is the penetration depth, F_b is the buoyancy force, F_c is the capillary force and F_D is the drag force.

The Von Karman approach is neglected for all other forces. The hydrodynamic forces per unit length can be approached by the following equation:

$$\mathrm{F} \approx \pi\rho {V_0}^2(R - V_0 t) \tag{10.2}$$

The cylinder is affected by the maximum hydrodynamic force in the early stage of water entry.

The non-dimensional force is defined for cylinders compared with different properties and water entry velocities:

$$C_s = \frac{F}{\rho {V_0}^2 R} \tag{10.3}$$

C_s is the non-dimensional slamming force coefficient. The slamming coefficient is the ratio of force by squared entry velocity, cylinder diameter and density of liquid.

Some other approaches are made to calculate the slamming force coefficient (C_s) numerically. The slamming coefficient is found as $C_s = \pi$ by using plat plate theory by Von Karman [2]. Other analytical results were calculated by Wagner [6] and doubled the Von Karman theory result as $C_s = 2\pi$. Both studies give constant values for different penetration depths. Greenhow and Yanbao [71] have the slamming force coefficient $C_s = \pi(1 - \frac{Ut}{R})$ by based on Von Karman theory for the first contact but decreases after penetration progresses. Wellicome [72] also benefits from Wagner's theory for the slamming coefficient and is obtained as $C_s = \frac{2\pi}{1+\frac{3}{2}\frac{Ut}{R}}$. Campell and Weynberg [73] obtained $C_s = \frac{5.15}{1+\frac{8.5\,Vt}{R}} + \frac{0.275\,Ut}{R}$. Miao [40] achieved the coefficient from experiments and presented $C_s = 6.1e^{-6.2\frac{Ut}{R}} + 0.4$. Another approach was made by Cointe and Armand [69] and is given by; $C_s = 2\pi - \sqrt{\frac{Ut}{R}}\left[\frac{10}{3} + 2\log(2) - 2\log\left(\frac{Ut}{R}\right)\right]$.

10.3 Results and discussion

The drop test for the circular cylinder is performed both numerically and experimentally. The heights of drop are 15 cm, 30 cm, 50 cm, 75 cm and 1 meter. Comparison is made analytically, numerically and experimentally. The strain gauges are used for measuring peak slamming forces so the distribution cannot be obtained from the experimental results. This is because the strain values are not shown at an exact point, but are measured in a local area. The strain gauge is applied at the tip point of the cylinder to obtain peak values. The transitions of the strain to force values are achieved by measuring the strain with the known forces values. So the experimental comparison is chosen just for the peak values.

The force distribution on the cylinder is demonstrated in figure 10.3 for water entry from 15 cm height. Analysis is made by using the k-ϵ RANS turbulence model of second order. The numerical results are between the Cointe and Armand [69] and Wellicome [72] analytical results and the high values at first contact decreases gradually.

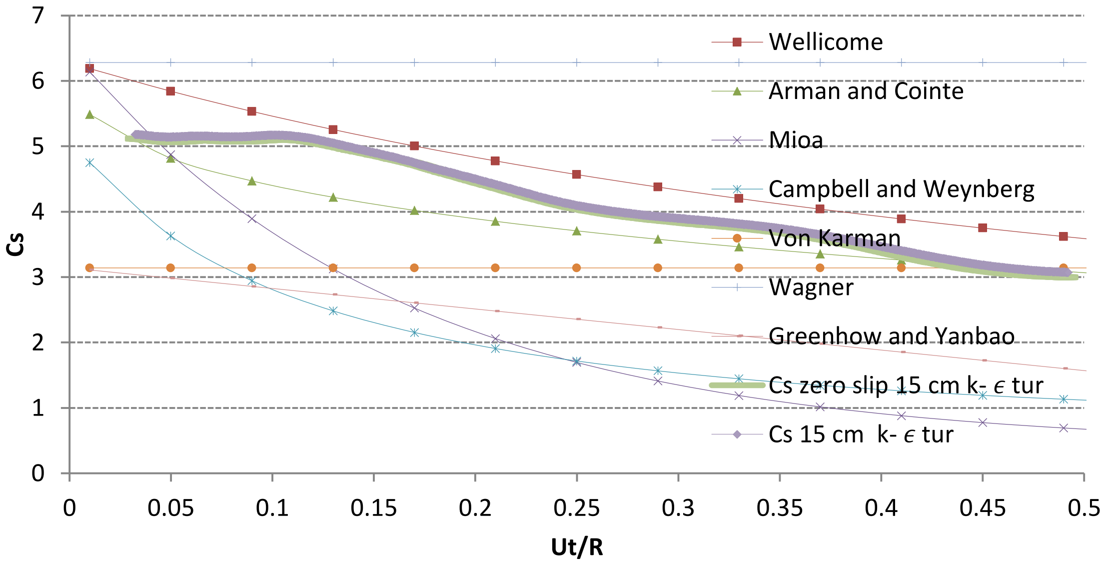

Figure 10.3 The slamming coefficient for drop height 15 cm

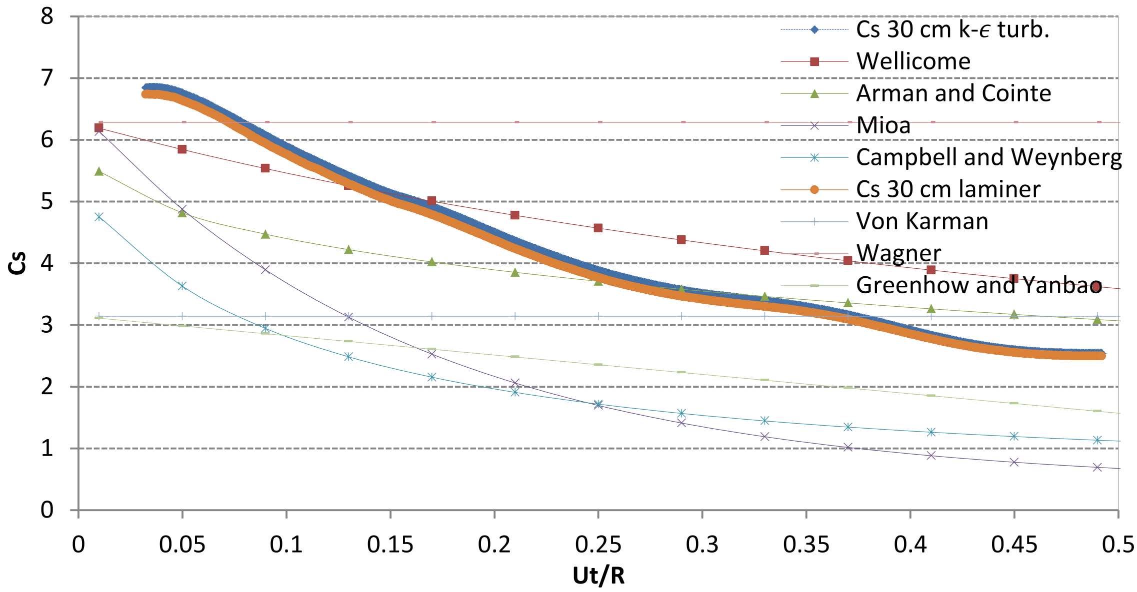

Figure 10.4 The slamming coefficient for drop height 30 cm

Figure 10.4 shows the numerical and analytical results for the slamming force coefficient. The numerical calculation is estimated for the 30 cm drop height. Two different models are used to perform the simulations. One of them is the laminar flow model and the other is k-ϵ Rans turbulence model. The general trend of the numerical force coefficient distribution is close to the analytical results. Estimation of the numerical results for both the laminar flow model and turbulence model are close to each other.

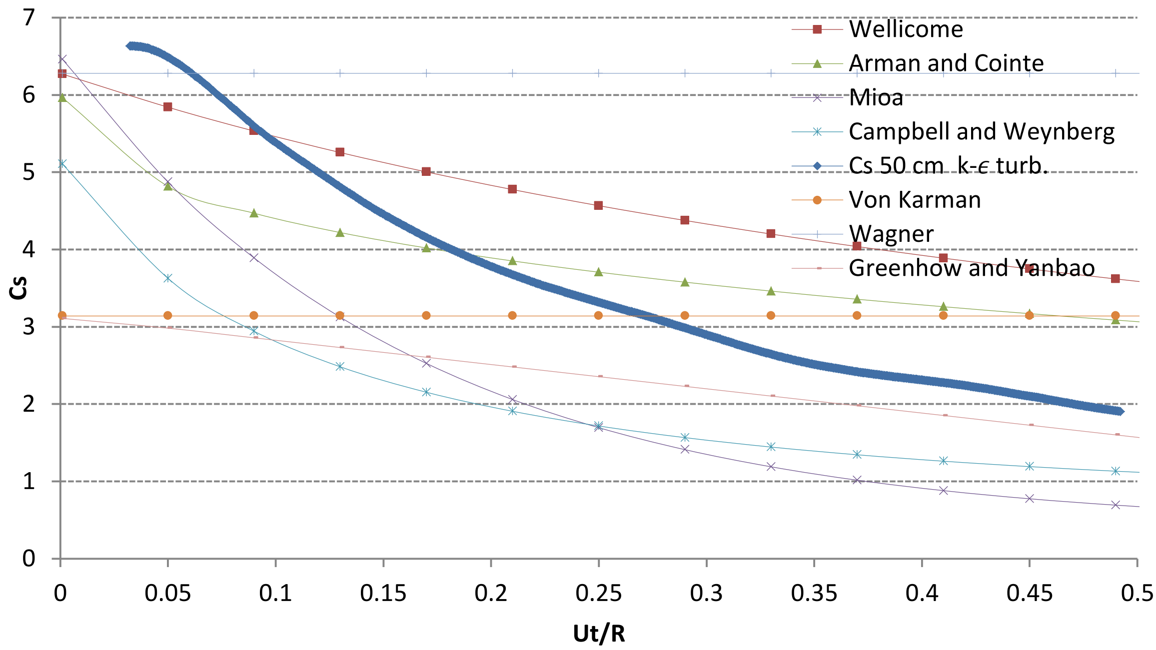

Figure 10.5 The slamming coefficient for drop height 50 cm

Figure 10.5 shows the Cs values for the drop test with 50 cm drop height. It indicates that the numerical approach is higher than the analytical results for the initial stages. The difference of Cs values is going to be close and can be placed between those in the theories. Figure 10.6 illustrates the Cs values for the drop test with 75 cm height. The k-ϵ turbulence model is performed in the simulation. The inviscid flow model is also selected for simulation of the 75 cm drop height. The viscous effect is neglected in the inviscid flow model and therefore the problem is reduced to the Euler equation and less computational cost is needed for simulation. The inviscid flow model is fairly to close the turbulence model in the Cs figure. In addition to the k-ϵ turbulence model and inviscid model, k-ω turbulence and laminar models are performed for the 100 cm drop test simulations (figure 10.6) so it is possible to clarify the different models effect on cylinder slamming. A minor discrepancy can be observed in the first interaction with the free surface between k-ϵ, k-ω turbulence and laminar model. Then all three Cs values are combined and follow almost the same route.

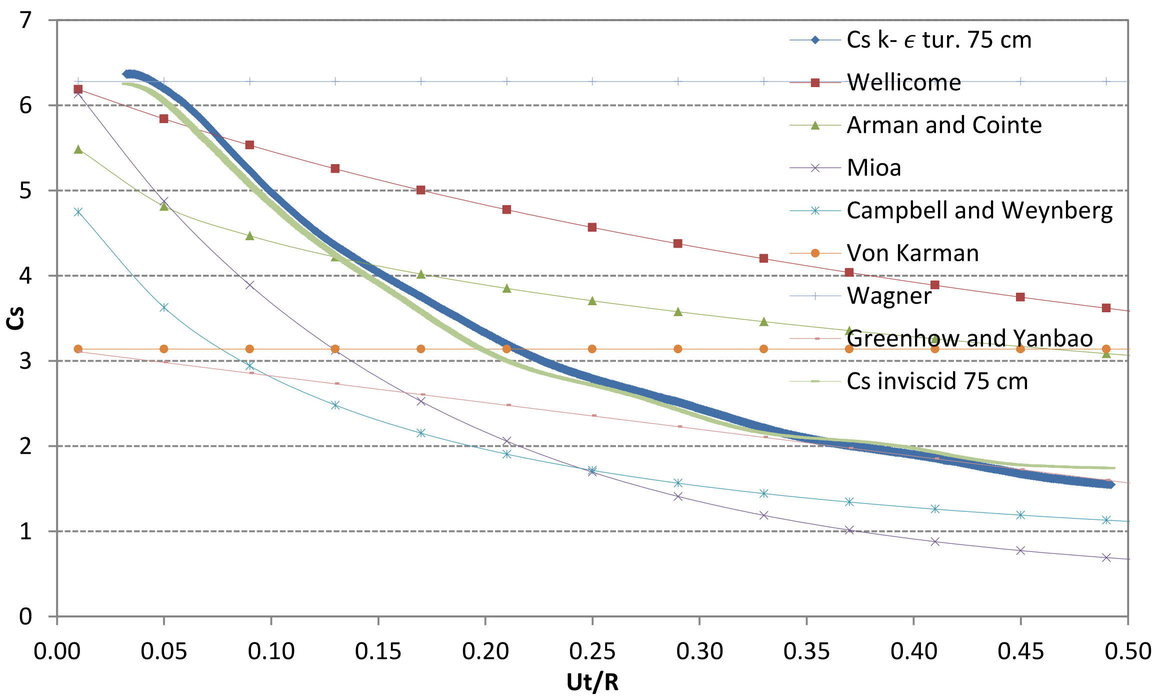

Figure 10.6 The slamming coefficient for drop height 75 cm and 100 cm

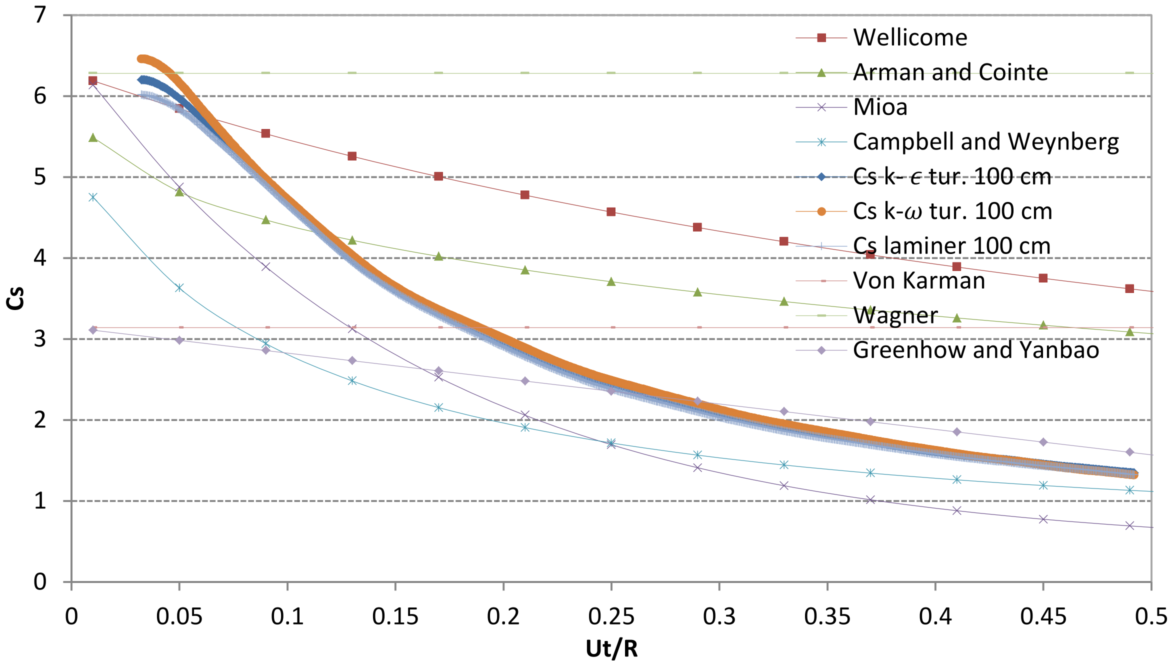

Figure 10.6 The slamming coefficient for drop height 75 cm and 100 cm (cont.)

The numerical results are also compared with the experimental results. Only the peak impact values are considered because of using the strain gauges in the experimental studies. Figure 10.7 illustrates the slamming coefficient values numerically, analytically and experimentally. Different types of cylinder materials are used for water entry. The initial cylinder material is UPVC and the others are aluminum of different thickness. Flexibility is an important issue for a slamming event. The strain data of the water entry of the relatively flexible UPVC cylinder test is measured with the least value and so the lowest non dimensional slamming force is obtained because some of the effect of the impact force is reduced by the flexible material. Therefore higher slamming coefficient values are reached for the relatively rigid cylinder. More details are given in chapter 6. The water entry simulations are performed by the rigid cylinder so flexibility is not take into account. Hence, the higher slamming coefficient value is observed in the numerical approaches for all drop heights.

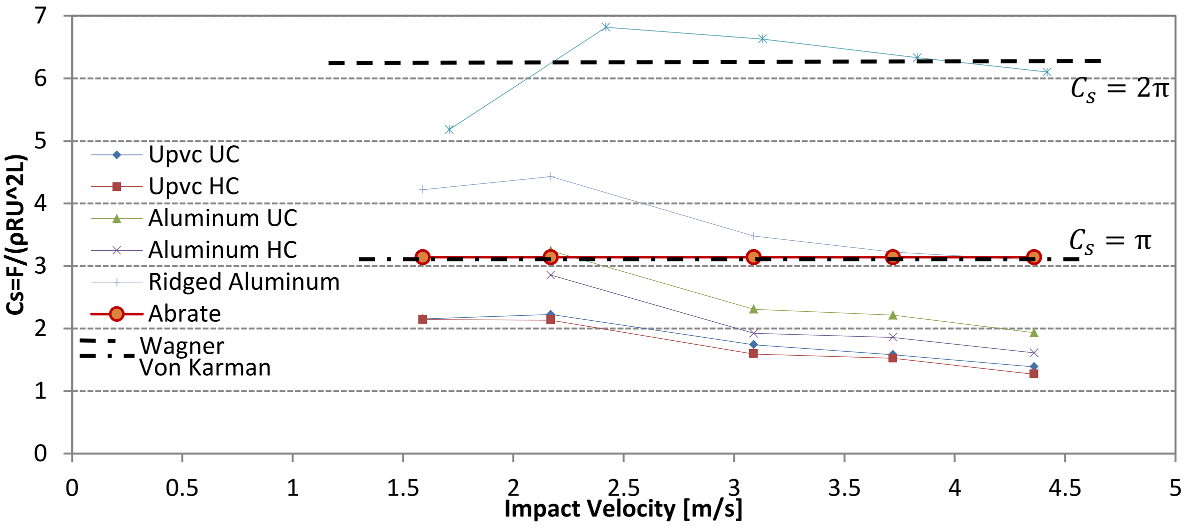

Figure 10.7 The peak slamming coefficient of cylinder

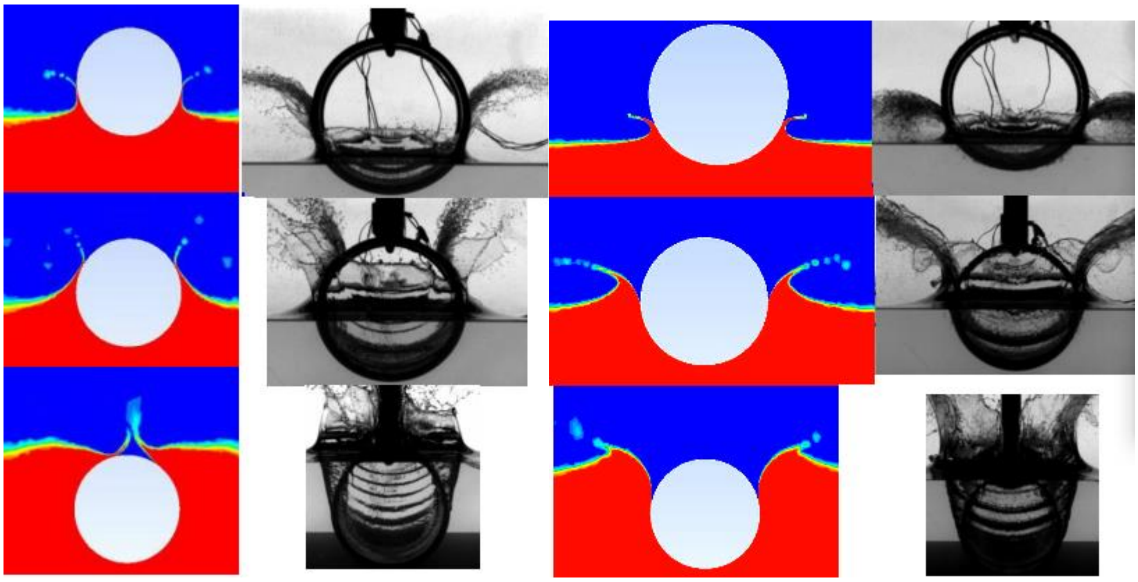

Figure 10.8 The comparison of water entry process of cylinder both numerical and experimental a) drop height 15 cm b)drop height 50 cm

Figure 10.8 shows the water entry sequences for numerical and experimental comparison. A general trend can be predicted but the whole process is not captured in the numerical simulation especially the splash zones because the approximations are used in the numerical approach.

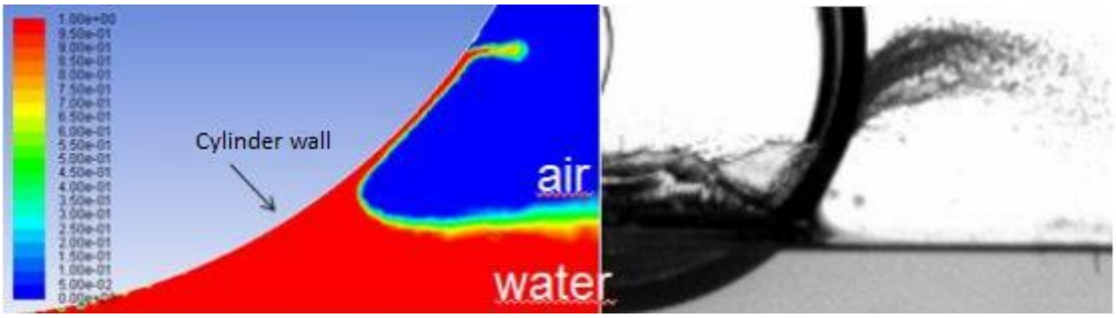

Figure 10.9 A close looks at the evaluation of pileup and splash both numerically and experimentally

The initial stage of cylinder water entry is depicted in figure 10.9. The penetration height and the entry velocity are the same for both the numerical and experimental drop tests. Evaluation of the pileup and initial separation in the numerical approach conform to the experimental picture, except for the splash zone.

Hydrophobicity is a surface characteristic that is increased with the contact angle of the water with the surface, so the wettability of the surface is decreased. A hydrophobic surface is created by selecting the boundary condition as a zero slip condition in the numerical approach (A. Kiara et al. [95]). When running run the cylinder water entry simulation with a hydrophobic surface, the cylinder boundary condition is selected with the slip condition as zero. The velocity contour is demonstrated in figure 10.10 both for the hydrophobic and hydrophilic cases for the same instant and same drop heights.

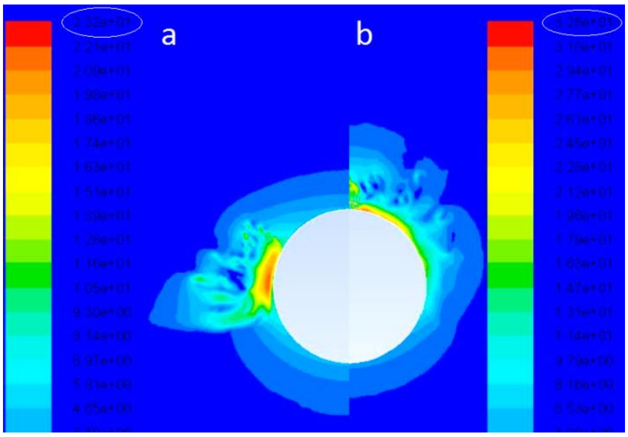

Figure 10.7 The velocity contour a) no slip condition b)free slip condition

Close up pictures of the free slip and no slip condition water entry tests show that a high velocity rate can be reached in the hydrophobic case in other words under free slip conditions. These results are expected because greater energy transfer occurs in the hydrophobic case. Comparison of the splash velocity from the experimental results are demonstrated in chapter 6 and the hydrophobic case always has a higher splash velocity.

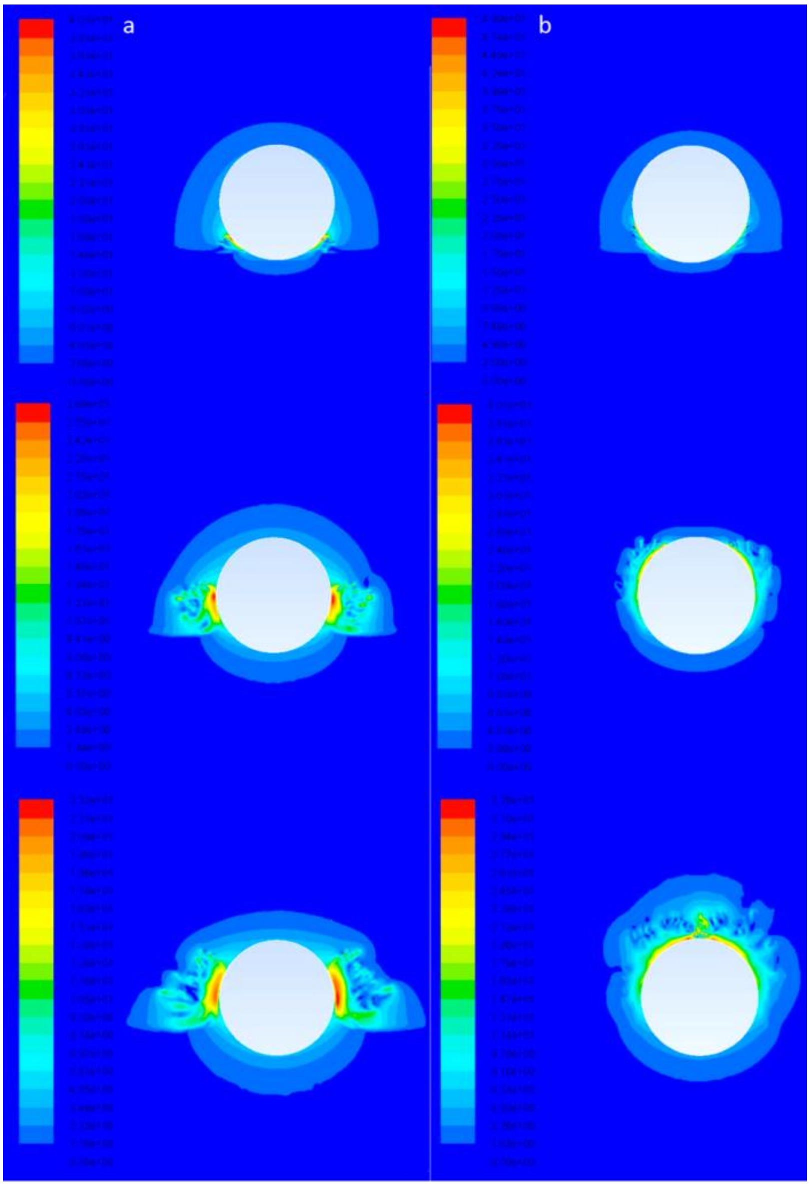

Figure 10.8 The velocity contour at cylinder water entry a) no slip condition b) free slip condition

The sequences of the cylinder water entry for both no slip and zero slip condition velocity contours are demonstrated in figure 10.11. The fluid velocity field is quite different in free slip conditions due to the high velocity value on the surface. The reason for these differences is that the attachment character is changed and the contact angle is increased by selecting a free slip surface for the cylinder.

CHAPTER 11

COMPARISON OF RIDGED SURFACES WITH HYDROPHOBIC SURFACES IN WATER ENTRY

In this chapter, the effects of hydrophobic surfaces in macro and micro scales have been demonstrated in a water entry problem by dropping wedge and cylinder shaped objects in a test rig. For the demonstrations, four different types of test objects were used in comparison, a pair of wedge and cylinder with ridged surface, and another pair of wedge and cylinder with smooth surface. To create the water repellent characteristics in micro scale, the test objects were coated with a hydrophobic coating material, which basically forms micro ridges on the surface. The jet flow, water pile up and water splashes were captured by a high speed camera and compared between the cases of macro and micro scale ridges and smooth surfaces. The early separation of the jet flow and splash and larger volumes of pileup were observed in cylinder drop tests on both micro and macro scale ridges comparing to smooth surfaces, meaning that similar hydrophobic effects are observed in both scale ridges. On smooth surfaces, at lower entry velocities, splash does not occur and the jet flow climbs up along the test object and at higher entry velocities, splashes and the jet flow occur at much higher penetration depths comparing to the ridged surfaces, causing late jet flow separation.

Hydrophobicity enables solid surfaces to have the characteristic of water repellency by creating micro scaled ridges. Water particles cannot penetrate into between the ridges and thus, resulting in less contact area between the solid surface and the water. Figure 11.1 illustrates this phenomenon called Cassie-Baxter state of wetting. In much larger sizes of ridges as seen in Figure 11.1b, similar phenomenon can be observed due to the air pockets trapped between the ridges during a water entry event of a solid body. In this study, the characteristics of water entry under hydrophobic effects are compared between the cases for macro and micro scaled ridges by carrying out drop tests in a water tank. The results are compared with the ones obtained from the tests of the smooth surfaced bodies of similar geometries.

11.1 The mechanism of the hydrophobic effects during water entry

In the water entry of cylinders and spheres, the location of the flow separation varies with the entrance velocity and the surface characteristics of the body. While there is no cavity created after the impact at lower entrance velocities with hydrophilic surfaces, a cavity is always formed with hydrophobic surfaces at any entrance velocity. And the cavity when hydrophobicity is present is always larger than the one with hydrophilic surfaces at higher entrance velocities. The complexity in its kinematics also creates differences in impact loads.

In early attempts to overcome this complexity in numeric simulations, the contact angle is inserted as a boundary condition and related to the maximum spread of the droplet and the contact time on the surface in VOF methods. This approximation is first proposed by Brackbill et al. [96] and the most widely-used model for implementing the contact angle. Weymouth [97] showed that modelling of hydrophobic and hydrophilic body surfaces with respectively free-slip and no-slip body boundary conditions can capture the cavity kinematics of bluff water entry. Kiara et al. [95] simulated the water entry of a cylinder by utilizing a modified weakly compressible SPH scheme (mSPH) by modelling the effects of the hydrophobic and hydrophilic surface via imposing free-slip and no-slip kinematic boundary conditions on the body surface. Although the effects of viscosity and surface tension can be neglected because of the higher values of Re and We, thus has no effects on the cavity shape, the change in viscosity and surface tension affects the shape of the jet (Kiara et. al., [95]). With the usage of mSPH, Kiara et al., [95] showed that the size of the cavity behind a cylinder changes with free-slip and no-slip kinematic boundary conditions, representing hydrophobic and hydrophilic surfaces respectively. But still, their simulations are not comparable with the experiments. The effects of the surface properties on the cavity dynamics in their simulations are limited between Ut/D=1-3 only. Although the slip length creates an interface of liquid flowing on air and solid mixture and decreases the effect of viscosity as the liquid flows partly on air, in the case of a water entry of a solid body, the effect of slip length is very limited (only in jet flow). Decrease in viscosity is not very important because of the higher Reynold numbers which imposes to neglect the effects of viscosity.

Duez et al. [66] proposed an interpretation in terms of contact line stability. As the jet flows upward and climbs up on the surface, the triple line (Figure 11.1b) of the jet moves in a way that it creates a dynamic contact angle, Θ_d much larger than the static contact angle, Θ (Figure 11.1a). As this dynamic contact angle reaches to 180°, the triple line is no longer stable. This is where the separation occurs. Duez [66] showed on small spheres that the threshold velocity at which the separation occurs is a function of the static contact angle.

Considering a water droplet hitting on a super hydrophobic surface, we observe that water droplet bounces like a ball making the interaction much more elastic. Therefore, the water entry of solid bodies under hydrophobic effects should be analyzed from the perspective of hydroelasticity as well.

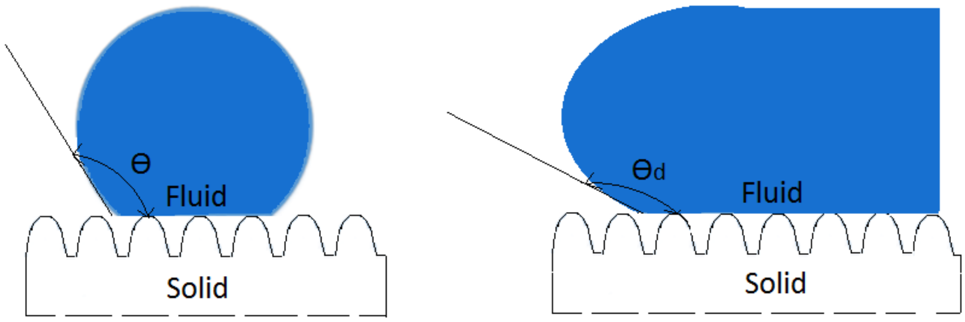

Figure 11.9 a) Illustration of Cassie-Baxter state b) Sketch of the triple line region in jet flow

The water surface has a specific energy that influences solid-fluid intersection lines and is well known as a surface tension. When a droplet releases to the surface, surface energy will occur, so too will a force. The energy balance for ideal wetting and partial wetting cases can be written as:

$$\gamma_{SA} = \gamma_{SL} + \gamma^* \cos\theta \qquad (11.1)$$

where s, a and l represent the solid, air and liquid. The γ^* denotes simply liquid and air energy and Θ is the contact angle between liquid and solid.

The full and partial wetting sketches are demonstrated in figure 11.2.

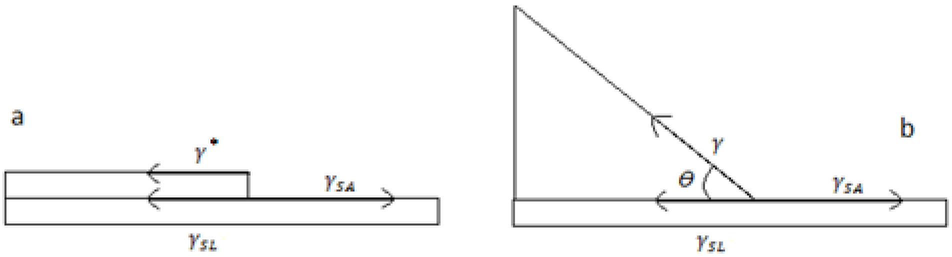

Figure 11.2 The sketches of a) fully wetted b) partial wetted

This equilibrium of energy does not occur for the quite wetting case. The droplet spreads on the surface and cannot make an angle between the surface and droplet, and the energy of solid - air γ_{SA} is larger than $\gamma_{SL} + \gamma^*$, which is the solid-liquid and liquid-air energy in the complete wetting case. Partial wetting is achieved by making the surface rough.

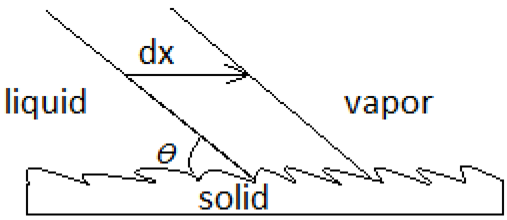

Figure 11.3 The Wenzel models [98]

The Wenzel model is generated for the surface energy on rough surfaces for the liquid which moves to the solid-vapor area as sketched in figure 11.3. It can be written as (David Quere [99]):

$$dE = r(\gamma_{SL} - \gamma_{SA}) + \gamma\ dx\ cos\theta^* \tag{11.2}$$

where dE is the variation of energy.

Every solid surface has roughness; either macro or micro scale roughness. This difference generates the surface wettability properties. The rate of surface roughness can be increased by a coating which produces micrometric scale roughness. Wenzel [98] introduced the roughness factor, r, which is the ratio of original surface area and apparent surface area of a rough surface.

$$cos\theta^* = r\ cos\theta \tag{11.3}$$

This equation estimates the wettability and thus, the hydrophobic ratio. When the value of ϴ is under 90°, the surface of an object becomes more hydrophilic at the $\theta^* < \theta$

stage. The exact opposite situation creates a more hydrophobic surface and so drying increases (David Quere [99]).

As a result of increasing the contact angle, both the wettability and the water retention are decreased. When coating is applied to the surface, the physical parameters can be enhanced. This is a chemical application but it has physical results. It has two layers, a base coat and a top coat. The first coat is prepared on the surface to hold the second part and the second layer makes the surface hydrophobic. The physical result of the coat is a scaling up of the surface roughness and no chemical interaction is made with the water. Spray application is performed by a compressor so the transfer of the coat is spread equally on the surface.

11.2 Results and Discussion

Smooth, hydrophobic coated smooth, ridged and hydrophobic coated ridged surfaces are compared in terms of splash characteristics, volume of pileups, air cavity and as well as the entire process of the water entry. The geometrical characteristics of the test objects are given in Table 11.1. At first, the visualized phenomenon obtained from the drop tests of the hydrophobic coated cylinder and sphere are compared with the ones from the literature to make sure that the same observations can be made. For comparison, an UPVC cylinder (OD 22 cm) is coated half in hydrophobic. The snapshots obtained from its drop test can be seen in Figure 11.4. In this figure, the left half is under hydrophobic effects. Although the hydrodynamic force acting on the object is the same, the phenomenon observed on both side is different. The jet flow and the water splash on the hydrophobic side is faster and moves more horizontally, and the volume of the pile up water is larger than the other half. It is due to more kinetic energy transferred to water. But on the uncoated side, the water jet climbs up along the surface, resulting in propagating the impact pressure (and local loads) onto the upper side of the cylinder. To investigate these effects when positive buoyancy is present, same drop tests were carried out with a low density plastic sphere (OD 18 cm). Figure 11.5 shows the snapshots taken during the water entry of this low density sphere. Similar phenomenon is observed on this case as well. So far, the case with micro scale ridges, the hydrophobic surface, has been discussed. The Figure 11.6 shows the water entry process of all four surfaces on cylindrical test objects. The snapshots from the water entry of the ridged aluminum cylinder is displayed in Figure 11.6a and the hydrophobic coated version of the same cylinder is in Figure 11.6b. The ridged surface without the hydrophobic coating shows somehow similar behavior as the hydrophobic coated smooth surface entering water. The ridged surface with the coating shows also similar behavior. The volume of pile ups and the size of air cavity are larger and the jet flow is faster for the cases with coating (micro) and with ridges (macro). It is also observed that the way of water splash forms and travels is similar in all three cases. The similarity of the water jet flow, air cavity and the pileups in smooth cylinder with coating and in ridged cylinder with and without the coating, is due to the existence of less solid contact area with water, caused by the trapped air between ridges (Figure 11.6a-6b). Having micro scale or macro scale ridges on the surface causes very similar effects. The ridged cylinder without the coating also shows the similar behavior of repelling water and preventing water from climbing on the solid surface.

Table 11.1 Geometrical characteristic of the test objects

	Smooth Cylinder	Ridged Cylinder	Smooth Wedge	Ridged Wedge
Mass	0.9 kg	1.1 kg	0.9 kg	1 kg
ID/side length	12.8 cm	14.4 cm	10 cm	12.7 cm
Wall thickness	0.2 cm	0.5 cm-0.7 cm	0.2 cm	0.2 cm-0.45 cm
Ridge Sizes (h/w)		0.2 cm/0.9 cm		0.25 cm/0.3 cm

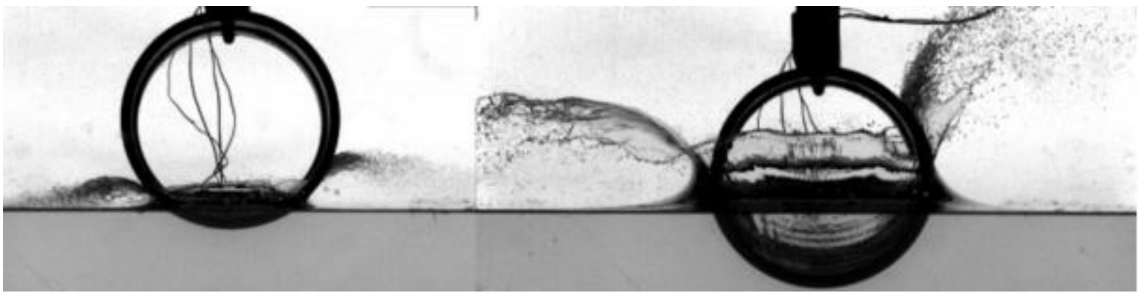

Figure 11.4 Snapshots taken at early and late stages of water entry of a cylinder dropped from 30 cm. Left half is treated with hydrophobic coating.

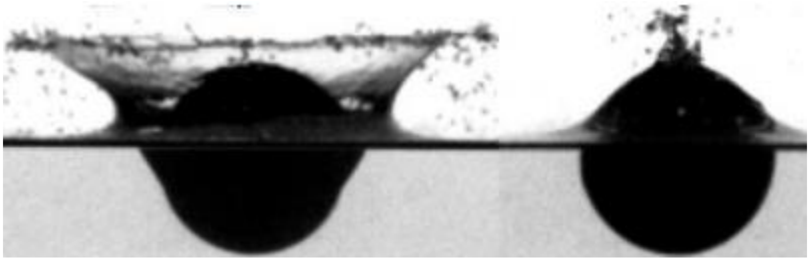

Figure 11.5 Snapshots taken at late stage of water entry of a sphere dropped from 30 cm. Hydrophobic coated (left) and untreated (right).

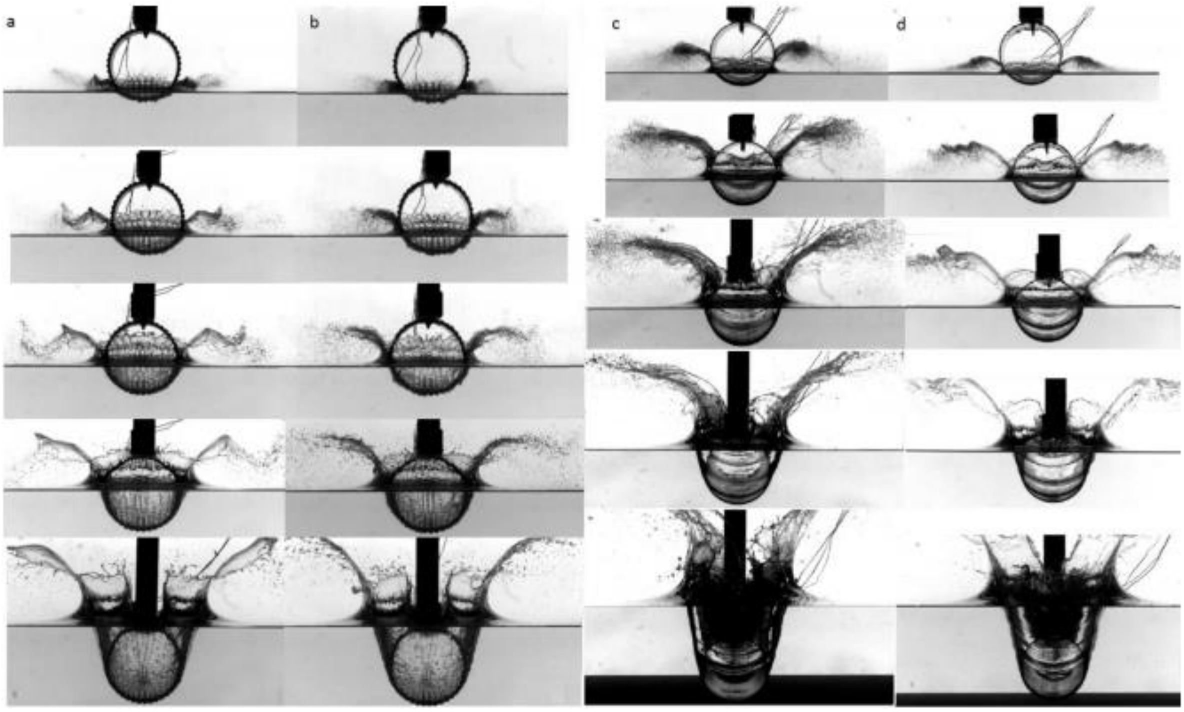

Figure 11.6 Snapshots taken at different time frames (t =11, 21, 31, 44, 78 ms) during water entry of a cylinder; a) untreated ridged surface b) coated ridged surface c) untreated smooth surface d) coated smooth surface

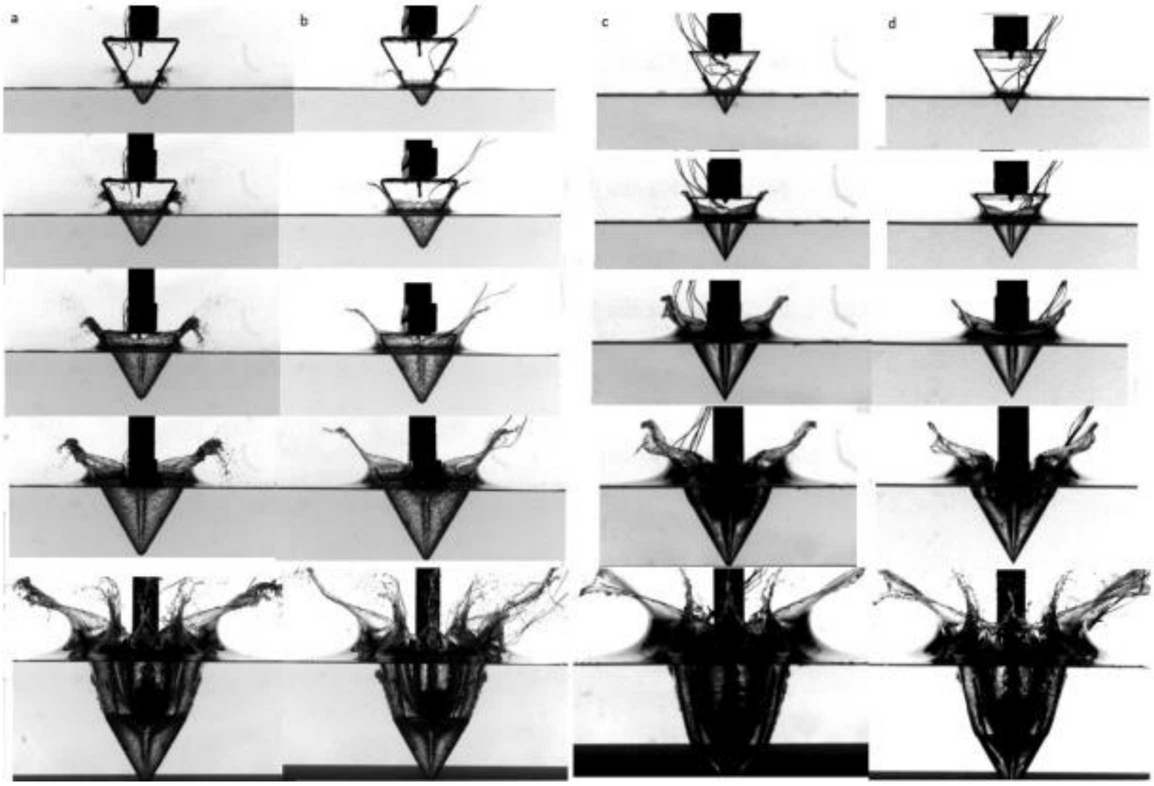

Figure 11.7 Snapshots taken at different time frames (t =11, 21, 31, 44, 78 ms) during water entry of a wedge; a) untreated ridged surface b) coated ridged surface c) untreated smooth surface d) coated smooth surface

After observing the effects of ridges, in micro or macro size, on water entry with an object with varying deadrise angle, namely cylinder, the same comparison was made with an object with a constant deadrise angle (60°), namely wedge. The same hydrophobic coating material was applied onto the surface of a ridged aluminum wedge and a smooth aluminum wedge. Figure 11.7a and 11.7b shows the snapshots from the water entry of the uncoated and coated ridged wedge, respectively, and Figure 11.7c and 11.7d from the water entry of the uncoated and coated smooth surface wedge, respectively. For the cases with coated surfaces, the volume of pile ups is larger and the jet flow is faster comparing to the uncoated cases. It is also observed that the jet flow and splash is thinner in the coated cases. However, the ridged wedge without coating did not show similarity with the coated smooth wedge as opposed to the cases with cylinder. This is due to having higher chances of air escape from the gaps between the ridges under the effects of a higher deadrise angle. Thus, having micro scale and macro scale ridges on surface did not show similarity at higher deadrise angles. Moreover, hydrophobic coated ridged wedge creates the thinnest jet due to the minimized water-solid contact area.

CHAPTER 12

CONCLUSION

In this study, both the early and later stages of the slamming of simple geometries are experimentally investigated to obtain the necessary knowledge to understand the mechanisms involved in the water entry of solid objects, and to predict the pressure distribution over the solid surface and the splash characteristics.

It was decided to begin the experiments on three main types of test objects; UPVC cylinder, aluminum cylinder and acrylic sphere. First, the effects of the drop height and the body flexibility on the problem are studied for these objects. Another parameter that is considered to have an influence on the impact loads during a slamming event is the surface properties of the solid objects. To extend understanding of the hydrodynamic effect of slamming onto the surface properties of objects, a series of experiments was carried out. To investigate the effects of the hydrophobicity and to provide some fundamental experimental results for slamming events under the hydrophobic effects, the splash and pileup characteristics, impact loads and penetration characteristics are compared for the cases both with and without hydrophobicity via high speed camera images and strain measurements.

The main conclusions for these advanced deadrise angle shapes, which may be drawn from the findings of this experimental study, are as follows.

The flow separation on solid surfaces and the splash formation are modified under the hydrophobic effects. The jet flow separates from the surface much earlier and splash velocities are higher for this case. This indicates that more kinetic energy is transferred to the jets.

Although the volume of water displaced by the test object is the same as in the first stages of impact, no matter what the drop height is, the water pileups under the hydrophobic effects are bigger in mass and move further away from the object. This means that more kinetic energy is carried away with the pileups.

For the hydrophobic coated test objects the peak strain values during slamming are smaller than for the case of the untreated test objects. Thus, introducing hydrophobicity onto a solid object experiencing water slamming causes a reduction of the impact forces.

The water jet separates from the surface of the cylinder and the sphere at higher entry velocities in both cases. This separation occurs much earlier in the hydrophobic case. whereas at lower entry velocities, this separation never occurs in the untreated case and the jet climbs up along the surface, while the separation is observed again at the beginning of the impact when hydrophobicity is present. This indicates that under the effect of hydrophobicity, no pressure pulse would occur at the surface of the cylinder or the sphere at larger deadrise angles even for larger penetration depths.

Under the hydrophobic effect, the peak value of the strain (force) occurs at a larger penetration depth compared to the untreated case under the same test conditions. This means that the force is distributed over a larger wetted area which corresponds to 62°-66° of the cylindrical circumference, while it is 67°-70° for the untreated case for the 100 cm drop height.

In the tests carried out by a sphere subject to positive buoyancy, it was observed that the sphere with hydrophobic surface slows down quicker and stops at smaller penetration depths. The difference in penetration depths is around 3% between the cases for the drop heights of 50 cm. This is due to more kinetic energy loss to the water under hydrophobic effects.

It is concluded from this study advanced deadrise angle shapes that not only the hydrodynamic, water and material parameters affects the slamming loads, but also the solid surface parameters have important effects as well. As such, it was observed that hydrophobic surfaces cause a reduction in slamming loads, distribute the impact pressure on a wider area and eliminate the pressure pulses from the solid surface at larger penetration depths.

The other experimental study undertaken presents the slamming phenomena for constant deadrise angle shapes by using wedges and cones with hydrophobic coating. The pileup coefficient and wetting factor were computed for all specimens and the hydrophobic effect is discussed. The penetration processes were recorded by high speed camera and measurements were made by applying strain gauges at the inner sides of the specimens. The experiments on the wedges and cones which have three different deadrise angles were performed with free drop tests. Each test was also conducted for the hydrophobic cases. A visualization study was made only for the relatively large deadrise angles for the wedge and conical shapes. This is because visibility is better those angles.

The results show that the pile up and wetting factor value is constant for untreated surfaces however that value decreases at the early penetration stages in the hydrophobic cases, then becomes constant, but with higher values than the untreated ones. This means that the surface roughness with the help of the hydrophobic coat is the reason for the quick energy transfer. The more the water repellence happens, the more the pileup coefficient and wetting factor can be calculated. The pileup coefficients are about 0.27 for the untreated ridged wedges, 0.35 for the hydrophobic ridged wedge, 0.55-0.6 for the untreated flat wedge and 0.75-0.8 for the hydrophobic flat wedge. The wetting factors, without adding jet flow to the computations, change in the range 1.5-1.6 for the hydrophobic cases and 1.4-1.5 for the untreated cases. The Wagner solution is approximately 1.58, so it is higher than the untreated cases and closer to the hydrophobic cases. The prediction of the wetting factor is lower with the W. S. Vorus [91] approach by 1.2. After taking jet flow into account, the wetting factor solution shows the similarities as characteristic but the values are increased. The potential energy of the specimens is transferred to the risen water at the rate of 60-80% (Panciroli et al. [29]). Another outcome of these results is that more energy transfer to the water is occurring for the hydrophobic cases.

Later, the experiments were made for measurement of the slamming impact by mounting strain gauges on the inner side of wedges and cones. The effect of the deadrise angle is demonstrated and, as expected, the strain values decreased with increasing the deadrise angle. Conservation was made by calibrating the strain value by applying the known force and measuring the reply of the strain gauges. Therefore, the relations are disclosed and it is understood that there is linear correlation in the force-strain graph. After the drop test, the measured strain values were converted to force and then the slamming coefficient was calculated. The slamming coefficients are compared to the Von Karman [5] and Wagner [6] theories by converted force values. The present values are positioned between the stated theorems. The same procedure was done for the hydrophobic cases and the reduction of the force is demonstrated by also using the strain measurement.

With the aid of a snapshot of the water entry process and strain measurement of the wedges and cones with hydrophobic surface, the surface parameter can be seen to change the slamming effects. Less interaction and quicker energy transfer to the water can be obtained for the hydrophobic cases so fewer impact forces are exposed.

The water entry of the cylinder is also investigated numerically. Simulation is performed ANSYS Fluent program and compared by experimental and analytical results. The non-dimensional results were analyzed for all three methods to obtain comparable values. Even the numerical results remain above the experimental results; they are closer to some analytical approaches because both flexible and relatively rigid cylinders were used in experiment and these values increase.

In order to investigate the water impact problem using ship models, the drop tests were carried out for the cases of bow flare and wet deck slamming with varying entry velocities and different surface properties. The scaled catamaran and bulbous bow sections were used for the experiments. Strain gauge measurements were applied on the test objects to quantify and compare the impact loads under the hydrophobic effects. A high speed camera was used to record the penetration process and the water uprising characteristics were compared via the high speed camera images during water entry.

An early separation of jet flow from the surface was observed on the ship model test when hydrophobicity was present. Thus the propagation of the impact pressure was expected to be different. Less impact loads were measured with the hydrophobic coated surfaces. This indicates that the kinetic energy transfer to the fluid is greater.

This study shows that the slamming loads, which are the reason for serious damages to structures, can be decreased with hydrophobic surface characteristics.

The water exit of partially and fully submerged bodies is also investigated to obtain the necessary knowledge for understanding the mechanism involved and to develop a mathematical model and a numerical approach predicting the pressure distribution and the takeoff loads.

The test results are presented from the exit tests using a sphere, a cylinder and a flat plate. Then, consideration is made of how flow separation on solid surfaces and free surface break-ups is modified on bodies with hydrophobic coating. The free water surface elevation is visualized with a high speed camera. In the case of partially submerged body exits, the amount of water attached to the body is lesser and separates from the solid surface quicker under hydrophobic effects. In the case of fully submerged bodies, the strain readings that represent the global loads acting on the body show different characteristics, indicating an easier exit in lesser amount of time but the peak strain values are the same for all geometric shapes. Investigation of the surface break-up via high speed images from different angles is done also for the hydrophobic cases but it is understood that the hydrophobicity does not show contribution early separation for fully submerges bodies.

Lastly, the characteristics of the water entry of the cylinder and wedge shaped objects with ridged surface are compared with the ones obtained with smooth surface under hydrophobic effects. For cylinders, having ridges on the surface creates similar effects during water entry to those of an object with a hydrophobic surface.

REFERENCES

[1] Jian, L.V., (2014). “Analytical Study of the Responses of Bottom Panels under Slamming Loads and Steel/Composite Hybrid Slamming Test Boat”, Dissertations, Lehigh University, Graduate School of Natural and Applied Sciences, Bethlehem.

[2] Sekhar, G. R. and Nallayarasu, S. (2013). “Experimental investigation of the wave slams and slap coefficients for array of non-circular section of offshore platforms’’, Ships and Offshore Structures, 8(1):15-28.

[3] Chuang, S., (1967). “Experiments on Slamming of Wedge- Shaped Bodies’’, J. of Ship Research, 11: 190-198.

[4] Kleefsman, K.M.T., (2005). Water impact loading on offshore structures – a numerical study, PhD thesis. University of Groningen. Graduate School of Natural and Applied Sciences, Groningen.

[5] Karman, V., (1929). The impact on sea plane floats during landing, the Technical Report 321, NACA.

[6] Wagner, H., (1932). “Uber stoss und Gleitvorgänge an der Oberfläche von Flüssigkeiten”, Zeitschrift fur Angewandte Mathematik Und Mechanik. 12(1): 193-215.

[7] Abrate, S., (2013). “Hull slamming”. Appl. Mech. Rev. 64(6):1-35.

[8] Chuang, S., (1969). “Theoretical investigations on slamming of cone-shaped bodies”, Journal of Ship Research 13(1):276-283.

[9] Chuang, S. and Milne, D., (1971). Drop tests of cones to investigate the three-dimensional effects of slamming, technical report 3543. NSDRDC.

[10] Lin, M.C. and Shieh, L.D., (1997). “Flow visualization and pressure characteristics of a cylinder for water impact”, Applied Ocean Research 19(2): 101-12.

[11] Peseux, B., Gornet, L. and Donguy, B., (2005). “Hydrodynamic impact: Numerical and experimental investigations”, Journal of Fluids and Structures 21(1): 277–303.

[12] Huera-Huarte, F. J., Jeon, D. and Gharib, M., (2011). “Experimental investigation of water slamming loads on panels”. Ocean Engineering 38(1): 1347–1355.

[13] Faltinsen, O.M., (2000). “Hydroelastic Slamming”, J. Marine Science Technology 5(1):49-65.

[14] Cooper, M. and McCue, L., (2011). “Experimental study on deformation of flexible wedge upon water entry”. 9th Symposium on High Speed Marine Vehicles, May, Naples, Italy.

[15] Panciroli, R., Abrate, S., Minak, G. and Zucchelli, A., (2012). “Hydroelasticity in water-entry problems: Comparison between experimental and SPH results”, Composite Structures 94: 532–539.

[16] Basaran, I., (2012). Hydroelastic analysis of ship structures under the slamming impact, PhD Thesis, Istanbul Technical University, Graduate School of Natural and Applied Sciences, Istanbul.

[17] Zhao, R. and Faltinsen, O., (1993). “Water Entry of Two-Dimensional Bodies”. J. Fluid Mech. 246(1):593–612.

[18] Battistin, D. and Iafrati, A., (2003). “Hydrodynamic loads during water entry of two-dimensional and axisymmetric bodies”. J. Fluids Struct. 17(5):643–664.

[19] Hanbing, L., Wang, H. and Soares, C. G. (2012). “Numerical and experimental study of hydrodynamic impact and elastic response of one free-drop wedge with stiffened panels”, Ocean Engineering 40(1):1-14.

[20] Yettou, E.M., Desrochers, A. and Champoux, Y., (2006). “Experimental study on the water impact of a symmetrical wedge”. Fluid Dynamics Research, 38(1):47-66.

[21] Judge, C., Troesch, A. and Perlin, M., (2004). “Initial water impact of a wedge at vertical and oblique angles”, J. Eng. Math. 48(1):279-303.

[22] De Backer, G., Vantorre, M., Beels, C., De Pre, J., Victor, S., De Rouck, J., Blommaert, C. and Van Paepegem, W., (2009). “Experimental investigation of water impact on axisymmetric bodies”, Applied Ocean Research 31(3):143–156.

[23] Smith, N. J., Stansby, P. K. and Wright, J. R., (1998). “The slam force on a flat plate in free flight due to impact on a wave crest”, J. Fluid Structure 12(1):183-96.

[24] Kim, Y. and Hong, S.W., (2008). “Theoretical and numerical studies on three dimensional water entry”, Proceedings of the Symposium on Naval Hydrodynamics, Seoul, Korea.

[25] Lewis, S.G., Hudson, D.A., Turnock, S.R. and Taunton, D.J., (2010). “Impact of a free falling wedge with water: Synchronized visualization, pressure and acceleration measurement”. Fluid Dyn. Res. 42(1):1-30.

[26] Fairlie-Clarkea, A.C. and Tveitnes, T., (2008). “Momentum and gravity effects during the constant velocity water entry of wedge-shaped sections”, Ocean Engineering, 35(7):706–716.

[27] Aarsnes, J.V., (1996). Drop test with ship sections-effect of roll angle, Report 603834.00.01.Norwegian Marine Technology Research Institute, Trondheim.

[28] Chuang, S.L.,(1966). “Experiments on flat-bottom slamming” , J. Ship Res., 10(1):10–17.

[29] Panciroli, R., Shams, A., Porfiri, M., (2015). “Experiments on the water entry of curved wedges: High speed imaging and particle image velocimetry”, Ocean Engineering 94(1):213–222.

[30] Greenhow, M., (1987). “Wedge entry into initially calm water” ,Applied Ocean Research, 9(4):214–223.

[31] Mei, X., Liu, Y., Yue, D.K.P., (1999). “On the water impact of general two-dimensional sections”, Journal of Applied Ocean Research, 21(1):1-15.

[32] Bisplinghoff, R. L. and Doherty, C. S., (1952). “Some studies of the impact of vee wedges on a water surface”. JFI, 253(6):547-561.

[33] Tveitnes, T., Fairlie-Clarke, A.C. and Varyani, K., (2008). “An experimental investigation into the constant velocity water entry of wedge-shaped sections”, Ocean Engineering, 35(14):1463–1478.

[34] Wu, G.X., Sun, H. and He, Y.S., (2004). “Numerical simulation and experimental study of water entry of a wedge in free fall motion”, Journal of Fluids and Structures, 19(3):277–289.

[35] Okada, S. and Sumi, Y., (2000). “On the water impact and elastic response of a flat plate at small impact angles”. Journal of Marine Science and Technology, 5 (1):31-39.

[36] Wu, G.X., Xu, G.D. and Duan, W.Y., (2010). “A summary of water entry problem of a wedge based on the fully nonlinear velocity potential theory”, 9th International Conference on Hydrodynamics, Shanghai, China.

[37] Korobkin, A.A. and Pukhnachov, V.V., (1988). “Initial stage of water impact. Annual review report of fluid mechanic”, 20(1):159-185.

[38] Oh, S.H., Kwon, S.H. and Chung, J.Y., (2009). “A close look at air pocket evolution in flat plate impact”, 24 th International workshop on water waves and floating bodies, Zelenogorsk, Russia.

[39] Campbell, J.M.C. and Weynberg, P.A., (1980). Measurements of parameters affecting slamming, Report No. 440, Wolfson Unit for Marine Technology, Southampton, United Kingdom.

[40] Miao, G., (1988). Hydrodynamic forces and dynamic responses of circular cylinders in wave zones, PhD Thesis, Norwegian University of Science and Technology, Graduate School of Natural and Applied Sciences. Trondheim.

[41] Molin, B., Cointe, R. and Fontaine, E., (1996). “On energy arguments applied to the slamming force”, Proceedings of the 11th Int. Workshop of Water Waves and Floating Bodies, Hamburg, Germany.

[42] Panciroli, R. and Porfirib, R., (2014). “A particle image velocimetry study of hydroelastic slamming”, Procedia Engineering 88(1):180–185.

[43] Faltinsen, O.M. and Zhao, R., (1997). “Water entry of ship sections and axisymmetric bodies”, AGARD FDP and Ukraine Institute of Hydromechanics Workshop on High-Speed Body Motion in Water, Kiev, Ukraine.

[44] Cointe, R., (1989). “Two dimensional water solid impact”, Journal of Offshore Mechanics and Arctic Engineering, 111(1):109-114.

[45] Wang, S. and Soares C.G., (2013). “Slam induced loads on bow-flared sections with various roll angles”, Ocean Engineering 67(1):45–57.

[46] Sun, H. and Faltinsen, O.M., (2009). “Water entry of a bow-flare ship section with roll angle”, J Mar Sci Techno, 14(1):69–79.

[47] Laverty, S.M., (2004). Experimental Hydrodynamics of Spherical Projectiles impacting on a Free Surface Using High Speed Imaging Techniques, Msc Thesis, Massachusetts Institute of Technology, Graduate School of Natural and Applied Sciences, Massachusetts.

[48] Brizzolara, S., Couty, N., Hermundstad, O., Ioan, A., Kukkanen, T., Viviani, M.and Temarel, P., (2008). “Comparison of experimental and numerical loads on an impacting bow section”, Ships and Offshore Structures, 3(4):305-324.

[49] Davisa, M.R. and Whelanb, J.R., (2007). “Computation of wet deck bow slam loads for catamaran arched cross sections”, Ocean Engineering 34(1):2265–2276.

[50] Greenhow, M. and Lin, W.M., (1983). Non-linear free surface effects experiments and theory, Report No. 83-19. Massachusetts: Massachusetts institute of technology.

[51] Colicchio, G., Greco, M., Miozzi, M. and Lugni, C., (2009). Experimental and numerical investigation of the water-entry and water-exit of a circular cylinder, 24th International Workshop on Water Waves and Floating Bodies, Russia.

[52] Tyvand, P.A. and Miloh, T., (1995). “Free-surface flow due to impulsive motion of a submerged circular cylinder”, Journal of Fluid Mechanics 286(1):67–101.

[53] Moyo, S. and Greenhow, M., (2000). “Free motion of a cylinder moving below and through a free surface”, Applied Ocean Research 22(1):31–44.

[54] Greenhow, M., (1988). “Water entry and exit of a horizontal circular cylinder”, Applied Ocean Research 10(4):191–198.

[55] Johannessen, S.R., (2012). “Used of CFD to study hydrodynamic Loads on Free-Fall Lifeboats in the impact phase”, MSc. Thesis, NTNU, Trondheim.

[56] Larsen, E., (2013). Impact Loads on Circular Cylinders, Master Thesis Norwegian University of Science and Technology, Graduate School of Natural and Applied Sciences, Trondheim.

[57] Alexandru, I., Brizzolara, S., Viviani, M., Couty, N., Donner, R., Hermundstad, O., Kukkanen, T., Malenica, S. and Termarel, P., (2007). “Comparison of experimental and numerical impact loads on ship-like sections. Advancements in Marine Structures”, In, Advancements in Marine Structures: Proceedings of Marstruct, UK.

[58] Ghandimi, P., Dashtimanesh, A. and Djeddi, S.R., (2012). “Study of water entry of Circular Cylinder by using analytical and numerical solutions”, J. Braz. Soc. Mech. Sci. & Eng. 34(3): 225-232.

[59] Faltinsen, O.M., (2007). “Challenges in hydrodynamics of ships and ocean structures”, Brodogradnja 58(3):268–277.

[60] Marcer, R., Berhault, C., Jouëtte, C. de, Moirod, N. and Shen, L., (2010). “Valıdatıon of CFD Codes For Slammıng”. V European Conference on Computational Fluid Dynamics ECCOMAS CFD.

[61] Ahsaee, H.G. and Nikserestht, A.H., (2013). “Numerical Simulation of two dimensional dynamic motion of the symmetric water impact of a wedge”. International journal of maritime Technology, 1(1):11-22.

[62] Engle, A. and Lewis, R., (2003). “A comparison of hydrodynamic impacts prediction methods with two dimensional drop test data”, Marine Structures 16(2):175–182.

[63] Wang, S., (2011). Assessments of slam induced loads on two dimensional wedges and ship sections, MSc Thesis, Instituto Superior Technico, Graduate School of Natural and Applied Sciences, Lisboa.

[64] Zhu, X., Faltinsen, O.M and Hu C., (2006). “Water Entry and Exit of a Horizontal Circular Cylinder”, ASME. J. Offshore Mech. Arct. Eng., 129(4):253-264.

[65] Nuffel, V.D., (2014). Experimental Study of the Slamming Induced Pressures, Forces and Deformations of Quasi-Rigid and Deformable Bodies during Vertical Water Entry, PhD Thesis, Ghent University, Graduate School of Natural and Applied Sciences, Belgium.

[66] Duez, C., Ybert, C., Clanet, C.and Bocquet, L., (2007). “Making a splash with water repellency”, Nature Physics, 3:180–183.

[67] Korkmaz, F.C. and Guzel, B., (2016). “Effect of hydrophobicity in slamming; case for advancing deadrise angle”, submitted to Ocean Engineering.

[68] Korkmaz, F. C., Guzel, B. and Safa, A., (2016). “The Effect of Hydrophobicity in Bow Flare and Wet Deck Slamming”, The Twenty-sixth International Ocean and Polar Engineering Conference, 469-471.

[69] Cointe, R. and Armand, J.L., (1987). “Hydrodynamic impact analysis of a cylinder”, J. Offshore Mech. Arct. Eng. 109(3): 237-243.

[70] Cointe, R., Fontaine, E., Molin, B. and Scolan, Y.M., (2004). “On energy arguments applied to the hydrodynamic impact force”, J. Eng. Math. 48(4): 305–319.

[71] Greenhow, M. and Yanbao, L. (1987).” Added masses for circular cylinders near or penetrating fluid boundaries: review, extension and application to water-entry, -exit and slamming”, Ocean Engineering 14(4):325–348.

[72] Wellicome, J.F., Temarel, P., Molland A.F., Cic, J. and Taunton, D. J., (1999). “Experimental measurements of the seakeeping characteristics of fast 4.5 m displacement catamarans in open irregular seas”, Ship Science Reports, 118(1): 67-80.

[73] Campbell, I.M.C. and Weınberg, P. A., (1980). “Measurement of parameters affecting slamming”, Wolfson Unit, University of Southampton, Report No. 440.

[74] Tveitnes, T., (2001). Application of added mass theory in planning, PhD Thesis University of Glasgow, Graduate School of Natural and Applied Sciences, Glasgow.

[75] Panciroli, R., Ubertini, S., Minak, G. and Jannelli, E., (2015). "Experiments on the dynamics of flexible cylindrical shells Impacting on a water surface", Experimental Mechanics 55(8):1537–1550.

[76] Blommaert, C., Van Paepegem, W., Dhondt, P., De Backer, G., Degrieck, J., De Rouck, J., Vantorre, M., Van Slycken, J., De Baere, I., De Backer, H., Degroote, J., Vierendeels, J., De Pauw, P., Matthys, S. and Taerwe, L., (2009). "Large scale slamming tests on composite buoys for wave energy applications", 17th Int. Conf. Comp. Material.

[77] Daniello, R.J., Waterhouse, N.E. and Rothstein, J.P., (2009). "Drag reduction in turbulent flows over superhydrophobic surfaces", Phys. Fluids 21(1):1-9.

[78] Sun, H., (2007). A boundary element method applied to strongly nonlinear wave–body interaction problems, PhD Thesis, NTNU, Graduate School of Natural and Applied Sciences, Trondheim.

[79] Guzel, B. and Korkmaz, F. C., (2015). "Experimental Investigation of Water Entry Impact on Hydrophobic Surfaces" , Proceedings of the 34th International Conference on Ocean, Offshore and Arctic Engineering.

[80] Chung, J.Y., Nahm, J.O., Kang, H.D. and Kwon, S.H., (2007). "A Novel Experimental Technique in Slamming", 22nd WWWFB, Plitvice, Croatia.

[81] Payne, P.R., (1993). "The spray sheets produced during vertical wedge impact and steady planning". Ocean Eng. 20(3): 247–261.

[82] Jalalisendi, M., Shams, A., Panciroli, R. and Porfiri, M., (2015). "Experimental reconstruction of three-dimensional hydrodynamic loading in water entry problems through particle image velocimetry", Exp. Fluids 56(2):1-17.

[83] Panciroli, R. and Porfiri, M., (2013). "Evaluation of the pressure field on a rigid body entering a quiescent fluid through particle image velocimetry" Experiments in fluids, 54(12):1-13.

[84] Nila, A., Vanlanduit, S., Vepa, K.S., Van Nuffel, D., Van Paepegem, W., Degroote, J. and Vierendeels, J., (2012). "High speed particle image velocimetry measurements during water entry of rigid and deformable bodies", 16th International Symposium on Applications of Laser Techniques to Fluid Mechanics. Lisbon, Portugal.

[85] Sun, H. and Faltinsen, O.M., (2006). "Water impact of horizontal circular cylinders and cylindrical shells", Appl. Ocean Res. 28(5):299–311.

[86] Ionina, M.F. and Korobkin, A.A., (1999). "Water impact on cylindrical shells", Proc. of 4th Intern. Workshop on Water Waves and Floating Bodies.

[87] Nila, A., (2014). Experimental Investigation of the Water Entry of Rigid and Deformable Bodies Using Time-Resolved Particle Image Velocimetry, PhD Thesis, Ghent University, Graduate School of Natural and Applied Sciences, Belgium.

[88] Payne, P. R., (1994). "Recent developments in added mass planning theory", Ocean Engineering, 21(3):257-309.

[89] Cointe, R., (1991). "Free surface flow close to a surface –piercing body, mathematical approach in hydrodynamic", T Miloh , Soc.,Ind. Appl. Math. Philadelphia, USA.

[90] Zhao, R. and Faltinsen, O.M., (1993). “Water Entry of Two-dimensional Bodies”, Journal of Fluid Mechanics, 246(1):593–612.

[91] Vorus, W.S., (1996). “Flat Cylinder Theory for Vessel Impact and Steady Planning Resistance”, Journal of Ship Research, 40(2):89-106.

[92] Tassin A., Jacques, N., Alaonui, A.E.M., Neme, A and Leble B., (2012). “Hydrodynamic loads during water impact of three-dimensional solids: modelling and experiments”, Journal of Fluids and Structures, 28(1):211-231.

[93] Korobkin, A. and Malenica, S., (2005). “Modified Logvinovich model for hydrodynamic loads on asymmetric contours entering water”, 12th IWWWFB, Longyearbyen.

[94] Rahman, M., Akimoto, H. and Ali, M.A., (2013). “Numerical Simulation of 2D hydrodynamic impact of wedge and Ship section at variable velocity”, Journal of naval architecture and marine engineering, 10(1):49-58.

[95] Kiara, A., Paredes, R. and Yue, D.K.P., (2013). “Evaluation of SPH in capturing flow separation points on hydrophobic and hydrophilic bodies during bluff water entry”, 9th International SPHERIC Workshop. Paris, France.

[96] Brackbill, J.U., Kothe, D.B. and Zemach, C., (1992). “A continuum method for modeling surface tension”, J. Comput. Phys., 100(2):335-354.

[97] Weymouth, G.D. and Yue, D.K.P., (2011). “Boundary data immersion method for Cartesian-grid simulations of fluid-body interaction problems”, J. Comput. Phys. 230(16):6233-6247.

[98] Wenzel, R.N., (1936). “Resistance of solid surface to wetting water”, Ind. Eng. Chem., 28(8):988-994.

[99] David, Q., (2008). “Wetting and roughness”, Annual Review of Materials Research, 38: 71-99.

CURRICULUM VITAE

PERSONAL INFORMATION

Name Surname	: Fatih Cuneyd KORKMAZ
Date of birth and place	: 28.03.1986, Erzurum
Foreign Languages	: English
E-mail	:fckorkmazz@gmail.com

EDUCATION

Degree	**Department**	**University**	**Date of Graduation**
Master	Naval Arc. and Marine Engineering	Yildiz Technical University	2012
Undergraduate	Mechanical Engineering	Yildiz Technical University	2009
High School		Erzincan Science High School	2004

WORK EXPERIENCE

Year	**Corporation/Institute**	**Enrollment**
2010-2011	Negmar Shipping Investment	Assistant Specialist

PUBLISHMENTS

Papers

1. Korkmaz, F.C. and Guzel, B., (2017). “Water entry of cylinders and spheres under hydrophobic effects; Case for advancing deadrise angles”, Ocean Engineering 129(1):240–252.

2. Korkmaz, F.C. and Guzel, B., (2015). “Experimental study on force distribution during slamming event with hydrophobic surface”, International Journal of Advances in Mechanical and Civil Engineering, 2(5):44-47.

3. Korkmaz, F.C., Su, M.E. and Alarçin, F., (2014). “Control of a Ship Shaft Torsional Vibration Via Modified PID Controller”, Brodogradnja, 65(1):17-27.

Conference Papers

1. Korkmaz, F.C., Guzel, B. and Safa, A., (2016). “The Effect of Hydrophobicity in Bow Flare and Wet Deck Slamming”, The Twenty-sixth (2016) International Ocean and Polar Engineering Conference.

2. Guzel, B. and Korkmaz, F.C., (2016). “Experimental Investigation of Water Exit Under Hydrophobic Effects”, ASME 35th International Conference on Ocean, Offshore and Arctic Engineering.

3. Guzel, B. and Korkmaz, F.C., (2015). “Experimental Investigation of Water Entry Impact on Hydrophobic Surfaces”. ASME 34th International Conference on Ocean, Offshore and Arctic Engineering.

Projects

1. Researcher; 2013-10-01-KAP03, “An Experimental And Numerical Investigation Of Slamming Loads On Ship Forms”.

AWARDS

1. Best paper awards, “The IRES 5th International Conference 2015”.